

REPORT DOCUMENTATION PAGE

*Form Approved
OMB No. 0704-0188*

The public reporting burden for this collection of information is estimated to average 1 hour per response, including the time for reviewing instructions, searching existing data sources, gathering and maintaining the data needed, and completing and reviewing the collection of information. Send comments regarding this burden estimate or any other aspect of this collection of information, including suggestions for reducing the burden, to Department of Defense, Washington Headquarters Services, Directorate for Information Operations and Reports (0704-0188), 1215 Jefferson Davis Highway, Suite 1204, Arlington, VA 22202-4302. Respondents should be aware that notwithstanding any other provision of law, no person shall be subject to any penalty for failing to comply with a collection of information if it does not display a currently valid OMB control number.

PLEASE DO NOT RETURN YOUR FORM TO THE ABOVE ADDRESS.

1. REPORT DATE (DD-MM-YYYY) 18-05-2012		2. REPORT TYPE		3. DATES COVERED (From - To)	
4. TITLE AND SUBTITLE Predicting Boat-Generated Wave Height: A Quantitative Analysis through Video Observations of Vessel Wakes				5a. CONTRACT NUMBER	
				5b. GRANT NUMBER	
				5c. PROGRAM ELEMENT NUMBER	
6. AUTHOR(S) Tan, Sam Wei Shen				5d. PROJECT NUMBER	
				5e. TASK NUMBER	
				5f. WORK UNIT NUMBER	
7. PERFORMING ORGANIZATION NAME(S) AND ADDRESS(ES) U. S. Naval Academy Annapolis, MD 21402				8. PERFORMING ORGANIZATION REPORT NUMBER	
9. SPONSORING/MONITORING AGENCY NAME(S) AND ADDRESS(ES) U.S. Naval Academy Annapolis, MD 21402				10. SPONSOR/MONITOR'S ACRONYM(S)	
				11. SPONSOR/MONITOR'S REPORT NUMBER(S) Trident Scholar Report no. 409 (2012)	
12. DISTRIBUTION/AVAILABILITY STATEMENT This document has been approved for public release; its distribution is UNLIMITED					
13. SUPPLEMENTARY NOTES					
14. ABSTRACT In this study, a new method of conducting vessel wake studies using video observations was evaluated. Using a remote web-based camera, vessel traffic along a section of the Severn River in Annapolis, MD, was recorded and subsequently processed using a newly developed vessel tracking tool. This tracking tool brings together computer vision techniques to track transiting vessels and obtain boat parameters usually investigated in vessel wake studies. When matched with wave records obtained using an underwater wave gage, these measurements create a new database from which relationships between vessel size, boating speeds, and their associated maximum wake heights can be examined.					
15. SUBJECT TERMS Vessel tracking, camera calibration, vessel-generated wake, wavelet analysis, video observations of vessel traffic					
16. SECURITY CLASSIFICATION OF:			17. LIMITATION OF ABSTRACT	18. NUMBER OF PAGES 112	19a. NAME OF RESPONSIBLE PERSON
a. REPORT	b. ABSTRACT	c. THIS PAGE			19b. TELEPHONE NUMBER (Include area code)

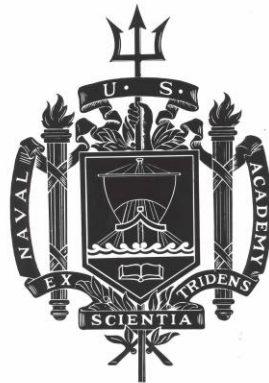
A TRIDENT SCHOLAR PROJECT REPORT

NO. 409

**Predicting Boat-Generated Wave Heights: A Quantitative Analysis through Video
Observations of Vessel Wakes**

by

Midshipman 1/C Sam W. Tan



UNITED STATES NAVAL ACADEMY
ANNAPOLIS, MARYLAND

This document has been approved for public
release and sale; its distribution is limited.

U.S.N.A. --- Trident Scholar Project Report; no. 409 (2012)

**Predicting Boat-Generated Wave Heights: A Quantitative Analysis through Video
Observations of Vessel Wakes**

By

Midshipman 1/C Sam W. Tan, Class of 2012
United States Naval Academy
Annapolis, Maryland

(signature)

Certification of Adviser Approval
Professor David L. Kriebel
Department of Naval Architecture and Ocean Engineering

(signature)

Associate Professor Jenelle A. Piepmeier
Department of Weapons and Systems Engineering

(signature)

Visiting Professor Patrick J. Hudson
Department of Naval Architecture and Ocean Engineering

(signature)

Acceptance for the Trident Scholar Committee
Professor Carl Wick
Deputy Director of Research & Scholarship

(signature)

USNA-1531-2

ABSTRACT

Vessel generated wake wash can lead to erosion of loose bank sediments and the destruction of fragile aquatic habitats. Although various studies have been done to quantify the magnitudes of boat wakes and their associated energy, there is yet to be a single model which can universally predict wave heights across different vessel sizes, boating speeds and hull forms. The goal of this study is thus to develop an updated equation model capable of predicting boat-generated wave heights given a set of basic vessel parameters.

While rigorous field testing can be conducted to increase the sample size of past studies, limitations due to cost and time usually makes it challenging to do so. In this study, a new method of conducting vessel wake studies using video observations will be proposed and evaluated. Using a remote web-based camera, vessel traffic along a section of the Severn River in Annapolis, MD, was recorded and subsequently processed using a newly developed vessel tracking tool. This tracking tool brings together computer vision techniques in MATLAB (Simulink) to track transiting vessels and obtain boat parameters usually investigated in vessel wake studies including 1) vessel length, 2) vessel speed, and 3) distance of its sailing line from the shore. When matched with wave records obtained using an underwater wave gage (Nortek AWAC), these measurements create a new database from which relationships between vessel size, boating speeds, and their associated maximum wave heights can be examined.

The results of this study were used to generate a new family of improved equations for the purpose of developing a unified description of vessel generated waves. This study also revealed the viable prospect of a quick, low cost, but effective manner of conducting vessel wake

studies that can be utilized in the future to better analyze the environment impacts of boating and vessel traffic. The use of video observations in such a manner also holds potential to aid the Navy's development of low-wake riverine vessels and its implementation of vessel tracking surveillance to augment port and harbor security.

Keywords: vessel tracking, camera calibration, vessel-generated wake, wavelet analysis, video observations of vessel traffic

TABLE OF CONTENTS

Abstract		1
Table of Contents		3
List of Figures		5
List of Tables		7
List of Symbols		8
Chapter 1	Introduction	9
Chapter 2	Background and Theory	
	2.1 Vessel Wake Characteristics	12
	2.2 Past Research on Vessel Wakes	18
Chapter 3	Method of Investigation	
	3.1 Overview	23
	3.2 Camera Installation	25
	3.3 Calibration Methods	27
	3.3 AWAC Profiler Setup	39
	3.4 Wave Logger Setup	42
Chapter 4	Video Processing	
	4.1 Overview	45
	4.2 Vessel Tracking Tool	49
Chapter 5	Wave Filtering and Processing	
	5.1 Overview	60
	5.2 Wave Processing Methods	66
Chapter 6	Results	
	6.1 Model Development	74
	6.2 Experimental Data Analysis	82
Chapter 7	Conclusions	93

	4
Acknowledgements	96
References	97
Appendix A – Specifications of vessels used for F_{∇} conversion factor	99
Appendix B – Simulink Code	100
Appendix C – AWAC Deployment Plan Setup	104
Appendix D – MATLAB Code	105

LIST OF FIGURES

Figure 1	- Wave Height vs. speed trends in planing vessels	12
Figure 2	- Typical vessel wave record	14
Figure 3	- Definition sketch of wave pattern generated by a moving vessel	14
Figure 4	- Super-critical wave pattern	17
Figure 5	- Example of H_{\max} vs. Boat Speed Curve	21
Figure 6	- Google Maps view of the data collection site	23
Figure 7	- Simplified flowchart of database generation	24
Figure 8	- Control vessels used	25
Figure 9	- Camera output image	26
Figure 10	- Transposing 2-D pixel positions into 3-D real world coordinates	27
Figure 11	- Camera tilt and pan angle	28
Figure 12	- Finding the image's vanishing point	29
Figure 13	- Determining the vanishing point using parallel field lines	30
Figure 14	- Trigonometric calibration setup	32
Figure 15	- Comparison between image plane and real world axis	32
Figure 16	- Addition of P_0	33
Figure 17	- Utilizing trigonometric relationships to find unknown, Y_0	34
Figure 18	- Conversion from row number to distance Y	35
Figure 19	- Conversion from row number to distance Y (Corrected)	36
Figure 20	- Relationship between x_{mag} and i_y	38
Figure 21	- Acoustic Surface Tracking (Yellow Beam) using the AWAC	40
Figure 22	- The Nortek AWAC	41
Figure 23	- Wave Logger deployed at the mouth of College Creek	44
Figure 24	- 6.1m Aluminum frame used to deploy the wave logger	44
Figure 25	- Simplified Flowchart for vessel detection and tracking	45
Figure 26	- Background subtraction and filters used to detect ship movements	48
Figure 27	- Flow diagram of simulation process	49
Figure 28	- Optical Flow Block	50
Figure 29	- Velocity Threshold Block	51
Figure 30	- Median Filter Block	52
Figure 31	- Morphological Opening Block	53
Figure 32	- Effect of increasing neighborhood size on binary silhouette	54
Figure 33	- Effect of modifying structural element size to remove vessel wake	55

Figure 34	- 'Blob Analysis' block	56
Figure 35	- Overview of measurement subsystem	57
Figure 36	- Raw video simulation output	58
Figure 37	- Filtered simulation output	59
Figure 38	- Video simulation output (magnified)	59
Figure 39	- Use of Wave spectral analysis to determine component frequencies	60
Figure 40	- Example of wave frequency spectrum obtained	61
Figure 41	- Application of wavelets in the identification of vessel generated wakes	63
Figure 42	- Definitive Characteristics of a Vessel-generated waveform	65
Figure 43	- Flow diagram for wave processing	66
Figure 44	- Results of filtering wave spectrum	67
Figure 45	- Sample of processed wave data	69
Figure 46	- Anomalous bursts caused by beam reflection error	70
Figure 47	- Geometry of vessel wave propagation	71
Figure 48	- Determining H_{\max} with the aid of wavelet scalogram	72
Figure 49	- Range of Vessel lengths tracked	73
Figure 50	- Normalizing wave heights at different (y/L) values	74
Figure 51	- Original H_{\max} vs. Vessel Speed for Robalo dataset	75
Figure 52	- Corrected H_1 vs. Vessel Speed for Robalo dataset	76
Figure 53	- Original H_{\max} vs. Vessel Speed for Zodiac dataset	77
Figure 54	- Corrected H_1 vs. Vessel Speed for Zodiac dataset	78
Figure 55	- Corrected H_1 vs. Vessel Speed for the entire dataset	79
Figure 56	- Comparing the relationship between $\nabla^{1/3}$ and LV	80
Figure 57	- Normalized Wave Height vs. F_{∇} plot	82
Figure 58	- Plot of Dataset with Regression Curves	83
Figure 59	- Comparison of gH/V^2 measured and gH/V^2 predicted	84
Figure 60	- Comparison of Predicted vs. Measured wave heights for Robalo	85
Figure 61	- Comparison of Predicted vs. Measured wave heights for Zodiac	86
Figure 62	- Normalized Wave Height vs. F_{∇} plot (differentiated by length)	88
Figure 63	- Normalized Wave Height vs. F_{∇} plot (log scale)	89
Figure 64	- H_1 vs. Speed Plot for $2.5\text{m} < L < 5.0\text{m}$	89
Figure 65	- H_1 vs. Speed Plot for $5.0\text{m} < L < 7.5\text{m}$	90
Figure 66	- H_1 vs. Speed Plot for $7.5\text{m} < L < 10.0\text{m}$	90
Figure 67	- H_1 vs. Speed Plot for $10.0\text{m} < L < 12.5\text{m}$	91
Figure 68	- H_1 vs. Speed Plot for $12.5 < L < 15.0\text{m}$	91

LIST OF TABLES

Table 1	-	Planing boat operation vs. various Froude numbers	17
Table 2	-	Data points used for calibrating P and Y	35
Table 3	-	Preliminary values of x_{mag}	37
Table 4	-	Vessel models studied	98

LIST OF SYMBOLS

Symbol	Meaning	Units
H_{\max}	Maximum Wave Height	m
L_V	Vessel Length	m
V_S	Vessel Speed	m/s
Y	Distance of vessel's sailing line from shore	m
∇	Vessel Displaced Volume	m^3
L	Wavelength	m
T	Wave Period	s
f	Wave Frequency	s^{-1}
g	Gravitational Constant	m/s^2
d	Water Depth	m
C	Wave Celerity	m/s
C_g	Wave Group Velocity	m/s
L_{wl}	Length at water line	m
θ_p	Angle of propagation	$^\circ$
α	Camera Pan Angle	$^\circ$
τ	Camera Tilt Angle	$^\circ$
i_y	Image Pixel Row Value	pixel
i_x	Image Pixel Column Value	pixel
X_{mag}	Magnitude per column pixel at a specified row	m/pixel
<hr/>		
Y_P	Image Horizontal Axis	-
X_P	Image Vertical Axis	-
Y_W	Real world Y-axis	-
X_W	Real world X-axis	-
Z_W	Real world Z-axis	-
F_L	Length Froude number	-
F_d	Depth Froude number	-
F_∇	Volume, or Displacement Froude number	-

CHAPTER 1 – INTRODUCTION

In recent years, the growing popularity of recreational boating has increased concerns over their impact on coastal and inland waterways. Wake wash from passing vessels have been noted to be detrimental to the shore environment, damaging shoreline property and disturbing aquatic habitats. As such, there is a rising demand for conducting vessel wake studies in order to better understand and quantify the nature of vessel-generated wake forms. For the Navy, where the focus is less of an environmental nature, understanding the relationship between vessel types and their wakes can possibly impact operational effectiveness, especially where clandestine infiltration of hostile shorelines using small, low-wake, riverine boats are concerned.

Despite the demand for vessel wake studies, quantitative investigations of vessel-generated waves have been rather challenging due to the dynamic nature of these wake forms and a lack of standardized wave measurement criteria. As a quick remedy, blanket restrictions (e.g. arbitrary speed limits) are often implemented to curb shoreline deterioration. However, these are neither truly effective nor based on adequate science, and can curtail high speed vessel operations that rely on speed for effective service (e.g. passenger ferries). In addition, a majority of past vessel wake studies were also specific to certain vessel types or geographical locations, which limit the universality of their findings. A broader, more general description of vessel-generated waves can therefore be useful in scenarios where a quick, simplified solution is required to quantify vessel wakes without the need for rigorous field testing and data collection.

In this study, a novel and efficient method of generating a broad vessel-wake database by using video observations of vessels was proposed. The findings from this study will help develop a unified description of boat-generated waves, in the form of improved equations, to calculate wave heights over a broader range of vessel sizes and boating speeds where previous models are inadequate in describing.

The sub goals of this investigation are as follows:

1. Create a robust vessel tracking tool within the MATLAB Simulink interface capable of efficiently calculating the following vessel parameters 1) vessel length, 2) vessel speed and 3) its distance of its sailing line from shore.
2. Generate a broader database of vessel types travelling at different displacement modes and their associated maximum wave heights, H_{max} , generated.
3. Formulate an updated equation model to calculate boat-generated wave heights.

To accomplish this, a remote camera was used to document vessel traffic over a section of the Severn River for approximately two weeks. The recorded vessel footage was then analyzed using computer vision techniques to isolate and track transiting vessels in order to obtain vessel parameters of interest (length, speed and distance of sailing line from shore). Wave height measurements concurrently recorded by an underwater wave gage, the NortekTM Acoustic Wave and Current profiler (AWAC), were also filtered and matched with its corresponding vessel of origin. This identification process was done with the aid of wavelet scalograms, which helped differentiate vessel generated wakes from background wind waves by highlighting regions in the wave-time signal where transient time-frequency shifts occur.

Finally, a database of boat parameters and their corresponding wave heights was compiled and analyzed for relationships present. The resultant database followed the expected trends of a wave-speed curve and proved to be a robust method of efficiently quantifying wave heights given the parameters studied. By implementing a least-squared regression method in Microsoft Excel, an updated family of equations was obtained and evaluated against equations proposed by past studies.

In summary, this study revealed the viable prospect of a quick, low cost, but effective manner of conducting vessel wake studies that can be utilized in the future to better analyze the environmental impacts of boating and vessel traffic. The use of video observations in such a manner also holds potential to aid the Navy's development of low-wake riverine vessels and its implementation of vessel tracking surveillance to augment port and harbor security.

CHAPTER 2 – BACKGROUND AND THEORY

2.1 Vessel Wake Characteristics

Relationship between vessel speed and wave height

Recreational vessels today come in all shape and sizes. While all vessels produce a certain amount of wake as they plough through the water, the height of such waves generated is not always directly proportional to speed. Upon reaching a *critical speed*, some vessels transition to planing mode and the shape and size of their wakes changes. Figure 1 illustrates the general trend of a planing vessel's maximum wave height versus its boat speed.

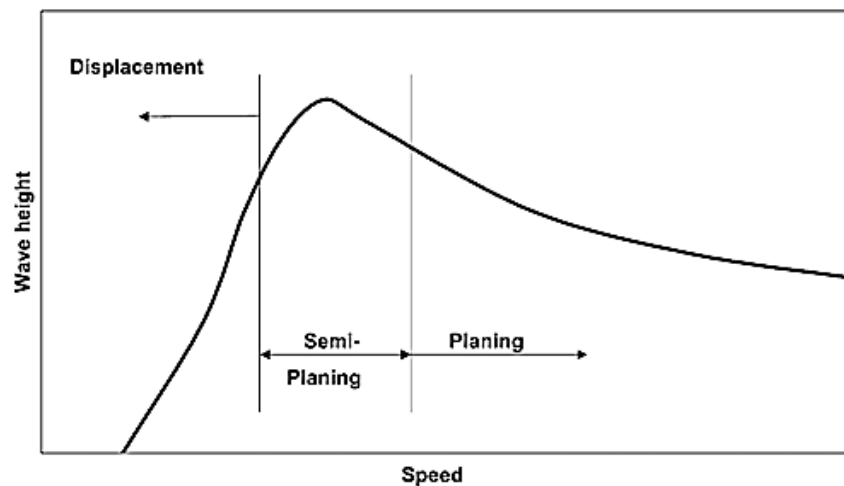


Figure 1: Wave Height vs. speed trends in planing vessels (Maynard, 2005)

Every vessel is uniquely designed to operate in different displacement modes. Some operate solely in the displacement zone (e.g. tankers, warships), while other smaller, faster vessels (e.g. speedboats, fishing vessels) have the capability to plane due to their unique hull form. In other words, a vessel's mode of operation plays a crucial factor in determining its wave-making ability. The three speed-displacement modes experienced by a typical planing vessel are described below:

1. Displacement – Boat weight is solely supported by the buoyant force of water. The vessel operates with the bow down and the relative slow speed of the vessel generates very little wake.
2. Semi-planing – As vessel speed increases, the lift force on the bottom of the vessel, generated by the differential fluid pressure on its hull, pushes the bow upwards, causing it to partially rise out of water. This mode is typically characterized by the largest wakes. However, the speed range in which semi-planing occurs is not well defined and can be narrow or wide depending on the vessel's hull form and design *critical speed*.
3. Planing – The lift force supports the hull position with little contribution from buoyant force. The bow dips and wake size decreases since less of the hull contacts the water surface.

Geometry of Vessel-generated waves

A vessel-generated wave that has travelled approximately one ship length from its point of generation will assume the shape of a sinusoidal wave. Once fully formed, the series of waves generated by a single disturbance is known as a 'wave train', and can be characterized by a single value, H_{\max} , which represents the maximum wave height generated for that event. Figure 2 illustrates a typical wave signal recorded by a wave gage.

In general, every vessel moving through the water generates at least two sets of waves: divergent waves caused by the bow and transverse waves caused by the stern and propellers.

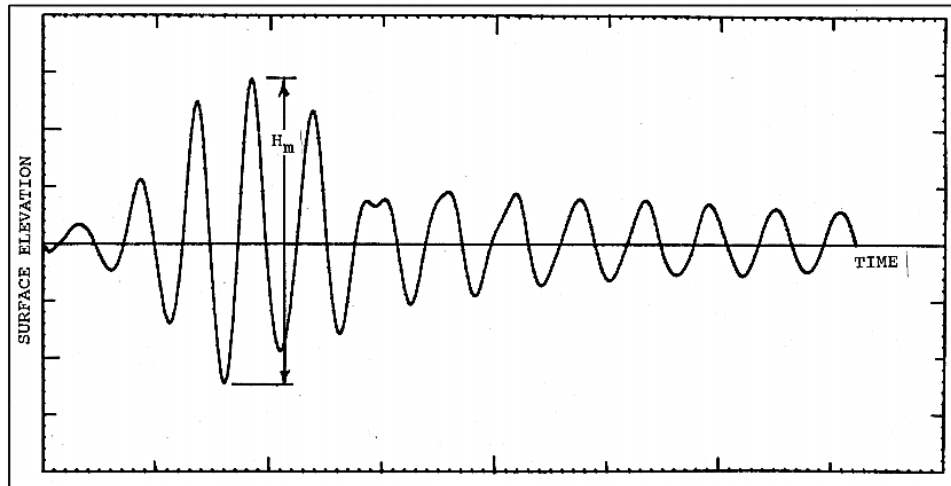


Figure 2: Typical vessel wave record, with H_{\max} denoted (Sorensen, 1973)

The intersection points of the two wave fronts form the cusp points where peak wave heights occur. This line of wave peaks is known as the *cusp locus line*, which generally occurs at an angle of 19.3° from the sailing line and propagates at an angle θ_p away from the vessel. Between the cusp points, the diverging and transverse waves are out of phase, resulting in much lower wave heights. Figure 3 illustrates a sketch of a typical vessel-generated waveform caused by a moving vessel in *deep water*.

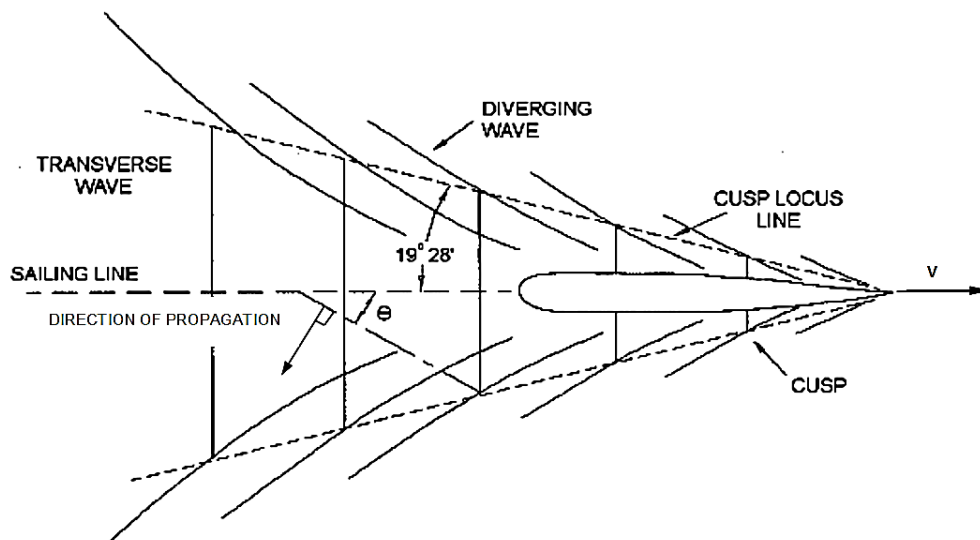


Figure 3: Definition sketch of wave pattern generated by a moving vessel

(Adapted from USACE, 2003)

Effect of Froude number on Vessel-generated waves

Water depth influences the waveform indirectly by influencing wavelength. In deep water, wavelength, L , is solely dependent on wave period, T , as given by the relationship:

$$L = \frac{gT^2}{2\pi} \quad (1)$$

where g is the force of gravity

A *deep water* classification applies whenever the relative water depth is $\geq L/2$. As the wave approaches the shore and water depth decreases to $< L/2$, the wave base begins to come into greater contact with the ocean floor. The wavelength decreases as a result of this shoaling process. A wave is considered to be in *intermediate waters* when this happens, and the wavelength is defined by the relationship:

$$L = \frac{gT^2}{2\pi} \tanh(kd) \quad (2)$$

where $k = 2\pi/L$ and $d =$ water depth

This equation applies to waves travelling in depths of $L/2$ to $L/20$. Subsequently, as the wave reaches shallower depths of $< L/20$, it transitions to shallow water and its wavelength is given by:

$$L = T\sqrt{gd} \quad (3)$$

The depth classification of the wave affects the type the Froude calculation that will be used to quantify the vessel-wake relationship. Divergent waves form at the bow and stern at an angle that is influenced by a vessel *Length Froude number* F_L that is defined as:

$$F_L = \frac{V_s}{\sqrt{gL_{wl}}} \quad (4)$$

where $L_{wl} =$ boat length at waterline, $V_s =$ boat speed

This length based Froude number is often used in deep water to determine the critical speeds for wave generation based on the vessel's length. Generally, when the length Froude number is approximately 0.4 in deep water (or $F_L = \frac{1}{\sqrt{2\pi}}$), the wavelength of the transverse waves is equal to the vessel's length, causing both the bow and stern wakes to interfere constructively. At such speeds, which are also known as the 'hull speed' or 'critical speed' for many conventional vessels, the resultant vessel wakes are the largest (PIANC, 2003). However, in shallower waters, the *Depth Froude number* F_d , which uses depth as a characteristic length instead of vessel length, is applied as a better characterization for the waves generated. The depth Froude number is given by:

$$F_d = \frac{V_s}{\sqrt{gd}} \quad (5)$$

Sorensen (1973) suggest that vessel-generated waves are influenced by shoaling when $F_d > 0.56$ (for transverse waves) and $F_d > 0.7$ (for divergent waves). Wave heights are expected to increase as F_d approaches unity ($F_d = 1$), with transverse waves gaining prominence over divergent waves. At this point, the wave speed is at its maximum value at a given depth, which gives a condition similar to the critical condition in deeper water. In other words, vessel-generated wakes are expected to be highest at $F_L = 0.4$ and $F_d = 1$.

Blount (1993) also suggests an additional volume or displacement Froude number that is characterized by the vessel's displacement. This volume Froude number, F_∇ , is defined as:

$$F_\nabla = \frac{V_s}{\sqrt{g \nabla^{2/3}}} \quad (6)$$

Where ∇ = volume of water displaced by boat

This Froude number is typically used for vessels travelling in semi-planing or planing modes. Table 1 (Maynard, 2005) provides a brief summary of the operating ranges of F_L and F_∇ for planing vessels in deep water. F_d was not included here since it only applies to shallow water scenarios.

Table I. Planing boat operation versus various Froude numbers

Operating range	F_L	F_∇
Displacement	<0.4	<1.3
Semi-planing	0.4 to 0.9	1.0 to 3.0
Planing	>0.9	>2.3

As the vessel speed increases beyond its critical value, the geometry of the wave pattern changes as well. The wave begins to depart from the typical Kelvin wave shape (as in Fig. 3) and begins adopting a more slender shape. As illustrated in Figure 4, at higher vessel speeds, the transverse wave disappears, leaving only divergent waves that trail behind as continuous curved lines (Whittaker *et al*, 2001). The angle of propagation θ_p increases and is dependent on the depth Froude number:

$$\theta_p = \cos^{-1} \left(\frac{1}{F_d} \right) = \cos^{-1} \left(\frac{\sqrt{gd}}{V_s} \right) \quad (7)$$

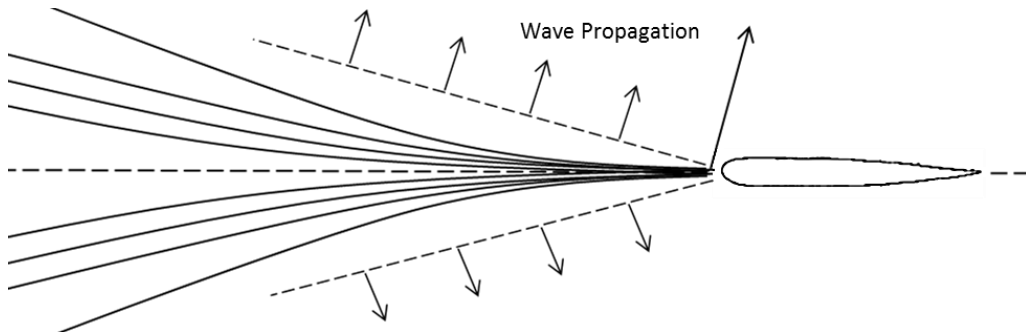


Figure 4: Super-critical wave pattern (Adapted from Whittaker *et al*, 2001)

Therefore, when vessels travel beyond their critical speed, the resultant wave locus lines bend further backward. The angle of propagation becomes more perpendicular to the vessel's sailing line, causing the vessels wakes to adopt a more slender pattern than when travelling at sub-critical speeds.

2.2 Past Research on Vessel Wakes

The Froude number calculations provide a general guideline on the critical speeds at which vessels transition from displacement to planing mode. Knowledge of these values can provide effective wake management strategies based on reducing time spent at or near critical velocities (Glamore, 2008). However, determining the Froude number alone is insufficient in predicting H_{max} . Vessel-generated wave height is also dependent on several other factors: bow geometry, operating draft of vessel, the distance from sailing line, and in relatively confined channels, the clearance between the vessel hull and the channel bottom and sides, (US Army Corps of Coastal Engineers, 2003) parameters which are not accounted by a vessel's Froude numbers.

Over the years, equations have been developed to predict wave heights as a function of these dependent parameters, such as vessel speed, distance from sailing line, water depth, and simplified hull geometry parameters. However, such equations are often obtained through regression analysis of field data collected by a specific author, and are hence limited to the specific vessel types and operational conditions represented by that particular investigation (US Army Corps of Engineers Coastal, 2003). There is yet to be a unified description of vessel wakes that can be applied across a broad range of vessel types.

In the Sorensen and Weggel model (S&W), developed after Sorensen and Weggel (1984) and Weggel and Sorensen (1986), none of the empirical parameters used are functions of the ship hull form, and are only dependent on the cube root of the vessel's displaced volume. They described the functional relationship of wave height as:

$$H_m = f[V, g, d, \nabla^{1/3}, x] \quad (8)$$

where H_m = maximum wave height, ∇ = volume of water displaced by boat, x = lateral distance from the sailing line of the boat.

Kriebel and Seelig (2001) improved on the S & W model by creating a more unified description of ship generated waves using a modified Froude number, F^* . Their effort was based upon a consolidation of published data on ship generated waves obtained from 60 individual vessels obtained from 16 papers, augmented by sea trials data collected along the Chesapeake Bay using the USNA Yard Patrol (YP) Craft. This modified Froude number (F^*) could be used to determine wave height while factoring the influence of hull geometry, and is done by incorporating coefficients that depend upon the ship block coefficient and bow entry length. Their new empirical model is given as:

$$\frac{gH}{v^2} = \beta (F^* - 0.1)^2 \left(\frac{y}{L}\right)^{-1/3} \quad (9)$$

where β is the empirical coefficient that varied with bow entry length (defined as the distance from the bow to the widest part of the hull) and y is the distance relative to the sailing line from the point of measurement.

In Kriebel and Seelig (2001), dimension values of wave heights and vessel speed were normalized in the form of gH/V^2 . An advantage of normalizing wave heights in this form is that

the resultant normalized wave heights should never exceed unity, which places a rational upper bound on the wave height data. Distance of the vessel from the point of wave measurement was normalized by the vessel length as $(y/L)^{-1/3}$. Their study compared different exponents and found the $(-1/3)$ model to be superior.

The above equation proposed by Kriebel and Seelig was shown to be effective but is limited in usage for displacement vessels operating at sub critical ($F_d < 1$) Froude numbers. On the other end of the speed-displacement curve (Fig. 1), Maynard (2005) created a general equation that is effective in describing wave heights for semi-planing and planing small boats using the following relationship.

$$\frac{H_m}{\nabla^{1/3}} = C(F_\nabla)^{-0.58} \left(\frac{x}{\nabla^{1/3}}\right)^{-0.42} \quad (10)$$

where C is the coefficient used to account for the deadrise angle, θ_{deadrise} , of the vessel

The predictive equation was developed using a database of field measurements obtained from a study of four vessel types and their wakes along the Kenai River in Alaska. In Maynard's study, the general equation was developed based on boat speed, volume displaced by the boat and distance from the boat at which the waves were observed. The results obtained using Maynard's proposed equation was found to be reliable when compared to independent data obtained by Zabawa and Ostrom (1980) not used in the development of the equation.

As demonstrated, the quantification of a vessel's H_{max} value requires knowledge of a vessel's hull form and its design characteristics – factors which may be difficult to obtain in order to quickly evaluate a vessel's wave making properties. Therefore, there lies a demand for a

simplified, generalized equation that provides a fast and economical evaluation criterion which sufficiently neglects the effects of individual hull differences. This requires the establishment of brand new datasets that will encompass a broad range of vessel types and hull forms. However, the cost and logistics involved in conducting numerous vessel runs in order to achieve such as goal remains as one of the biggest limiting factors.

Figure 5 illustrates a wave height vs. boat speed plot obtained from field measurements of a series of controlled boat passes conducted by Zabawa and Ostrom (1980). In their study, a 26ft Uniflite Cruiser was driven along Broad Creek (in Anne Arundel County, MD) at various distances from the shoreline for a range of speeds. Their results show a non-linear increase of maximum wave height with boat speed as expected. Nevertheless, the small number of data points included in these plots severely limits its usefulness.

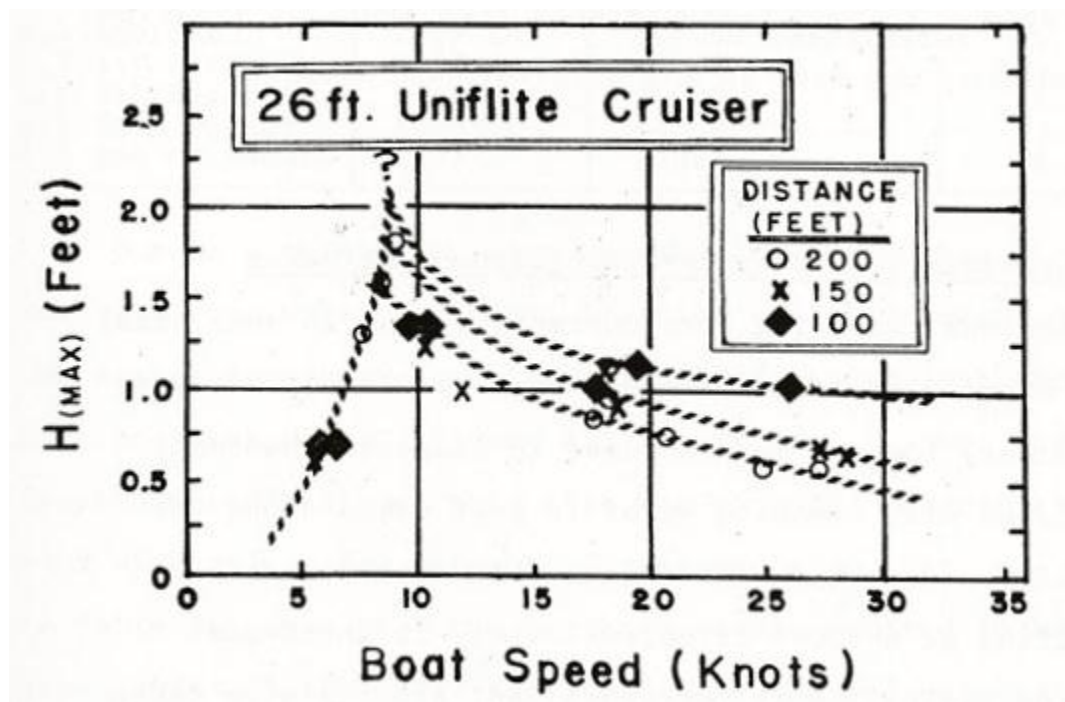


Figure 5: Example of H_{\max} vs. Boat Speed Curve (Zabawa and Ostrom, 1980)

In order to improve on current equation models, our study seeks to establish a new and efficient method of conducting future vessel wake studies by means of a novel vessel tracking tool. Using this tool, we seek to establish a sizable database of vessel types and wave height measurements that will provide additional data points to help “fill the gaps” of existing prediction models described earlier in this report.

CHAPTER 3 – METHOD OF INVESTIGATION

3.1 Overview

To generate a broader dataset of vessel types and their associated maximum wave heights, this project utilized a remote camera to record passing vessel traffic along a stretch of the Severn River in Annapolis, MD. Concurrently, an underwater ‘Acoustic Wave and Current Profiler’ (AWAC) was deployed at the same site to record changes in water elevation caused by boat wakes. Video footage recorded over a span of approximately two weeks was analyzed using a Simulink program written in MATLAB. Figure 6 shows the relative positions of where the instruments were deployed for data collection

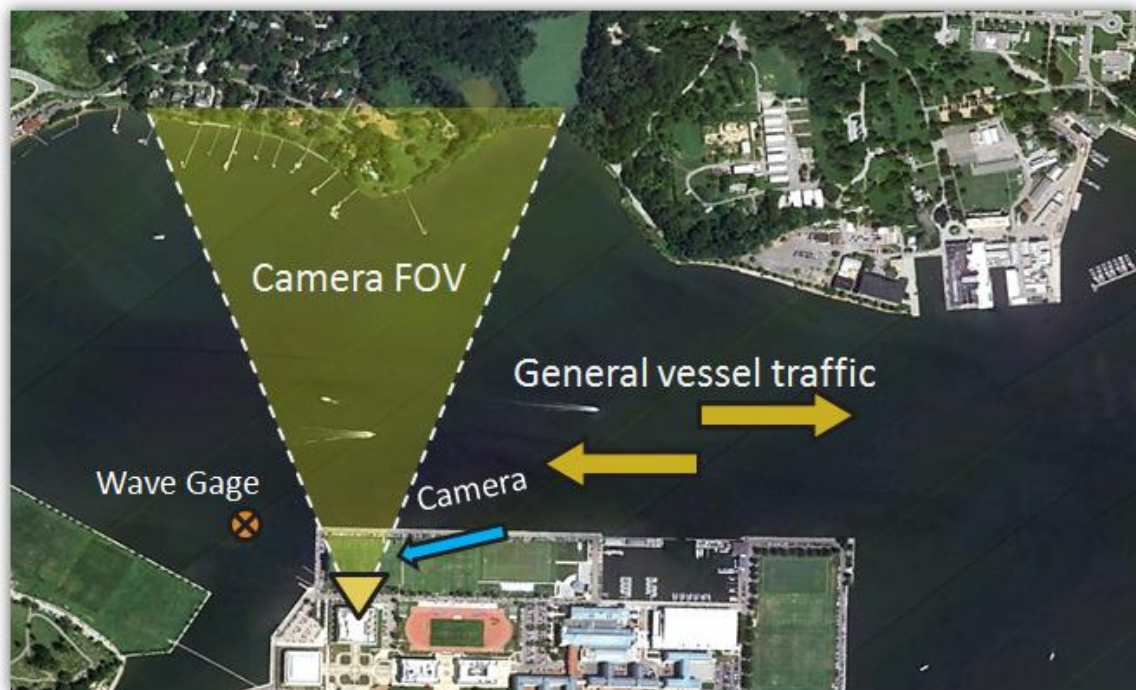


Figure 6: Google Maps view of the data collection site

(Severn River, Annapolis MD)

From the video footage, target boat parameters – such as vessel length, vessel speed, and its distance from the wave gage, were extracted and plotted against the wave record in time. Boats tracked were then matched with its corresponding wave event through a matching process with the aid of wavelet scalograms and an identification criterion adapted from Sheremet *et al.* (2011). In addition to the main dataset of random passing vessels, two additional series of controlled runs using two known vessels were also executed during the same period of experimental data collection. Figure 7 provides a brief overview of the data collection process.

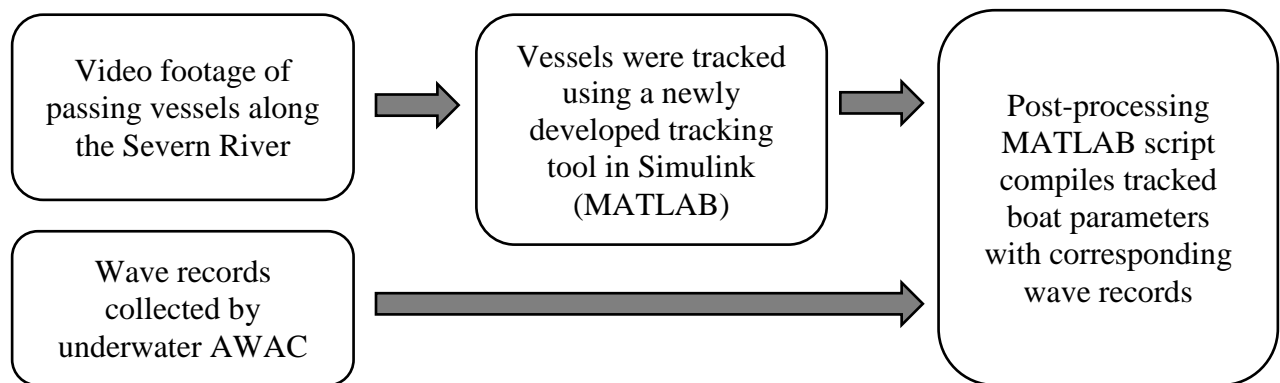


Figure 7: Simplified flowchart of database generation

Control Vessels Used

The two known vessels selected were the Robalo R227 Dual Console recreational boat (LOA = 6.55m / 21'6") as well as the USNA Zodiac SeaRider SR 4.7 (LOA = 4.74m / 15'6") Rigid Hull Inflatable Boat (RHIB). The two vessels, as shown in Figure 8, were selected due to their ability to attain high planing speeds. In addition, the Robalo R227 falls within a typical size of a recreational boat often observed to be transiting along the Severn, while the Zodiac falls within the common small craft category often utilized by the Navy and its small boat units to conduct a myriad of missions. Together, these two vessels will act as control vessels to help evaluate the accuracy and effectiveness of our proposed vessel tracking tool.



Figure 8a: Robalo R227 Dual Console Recreational Boat (www.robalo.com)



Figure 8b: Zodiac SeaRider RHIB

During the experimental data collection phases from 1) 13-18 October 2011 and 2) 20-27 October, approximately 1100 vessels were recorded by the remote camera. This dataset was filtered to eliminate unsuitable data points (e.g. stationary vessels, frames with too many vessels) as well as falsely tracked targets (e.g. triggered by breaking wind waves). The finalized dataset had a total of 471 true vessel-wake events and was subsequently used in the formulation of our model.

3.2 Camera Installation

A remote camera (StarDot NetCam XL, Model: CAM-XL640-01) was used to document vessel traffic along the Severn River to link the wave data recorded by the AWAC to the length, speed and distance of the vessels. The camera was mounted indoors (3rd Level, USNA Rickover Hall) at a height of 19.51 m (or 64.0 ft.) above Mean Sea Level (MSL). The camera was

programmed to record continuously from sunrise till sunset daily (0700hrs -1800hrs) at a RGB VGA video output of 1344x1024 pixels per frame. Images recorded were stored on a web-based server which could be subsequently retrieved by recalling its IP address and viewed on a desktop PC using StarDot DVR Digital Video Recording Software. The camera field-of-view (FOV) was positioned such that vessel traffic will pass horizontally across the screen and parallel to the seawall. Figure 9 defines the image coordinate system that will be implemented in this study. Vessel parameters that will be investigated are included in this Figure 9 as well.

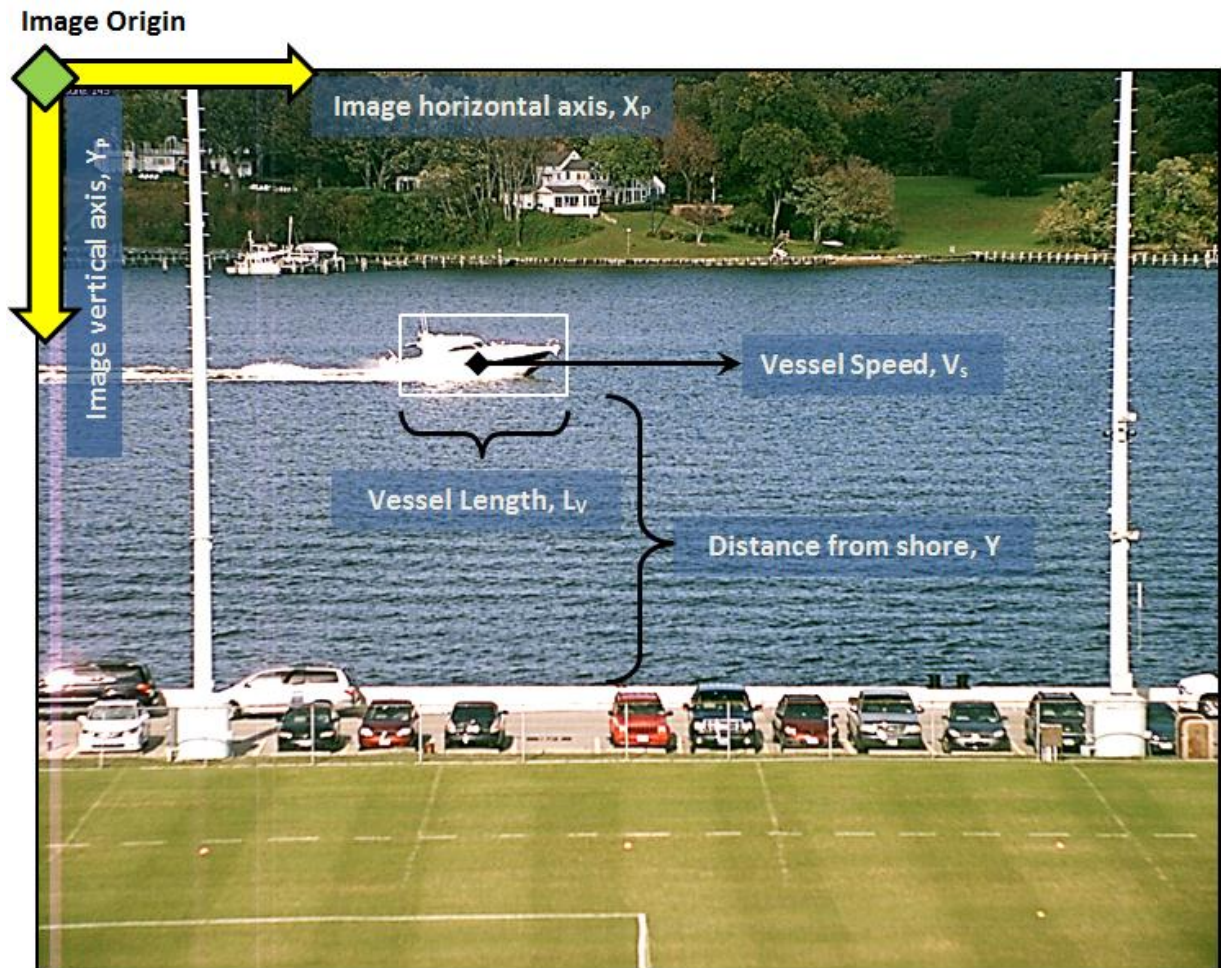


Figure 9: Camera output image (1344×1024 pixels)

3.3 Camera Calibration Methods

Camera calibration is the process of determining appropriate projection equations that will correlate 2D image geometry (measured in pixels) to real-world dimensions (in meters or feet). For an effective tracking measurement system, a new method of camera calibration by assuming trigonometric relationships between the projection plane and the real world horizontal was proposed. This was done by measuring GPS distances of fixed points within the image, from which equations that convert pixel widths into real world distances were established. The trigonometric projection method proved to be sufficiently accurate and was subsequently adopted for vessel tracking. Figure 10 provides a simplified illustration of transposing three different points on the 2D video image from the Y_P and X_P coordinates into the 3D real world coordinates, Z_W , Y_W , X_W .

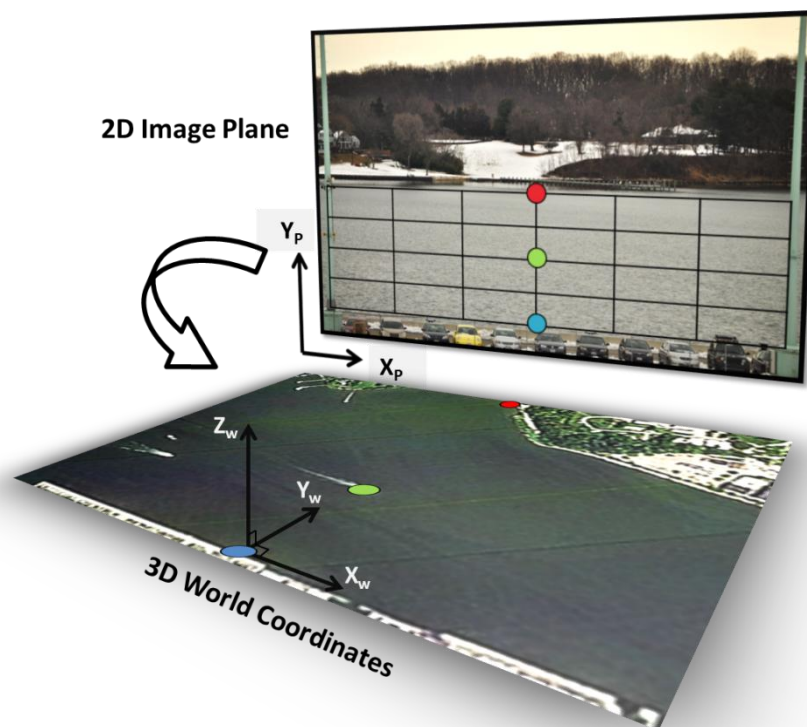


Figure 10: Illustration of transposing 2D pixel positions into 3D real world coordinates

Existing Literature on Camera calibration

Before the trigonometric projection method was adopted, common calibration methods utilized in road traffic monitoring problems were considered as well. Kivanc Bas & Crisman (1998) describes a method that requires the known height and the tilt (defined in Figure 11) of the camera with a pair of parallel lines that are naturally present within the scene to determine the ‘vanishing point’ of the image. In their proposed method, the vanishing point is the point where naturally occurring parallel lines within the image, for example, road lane lines as demonstrated in Figure 12, extends and meets at infinity.

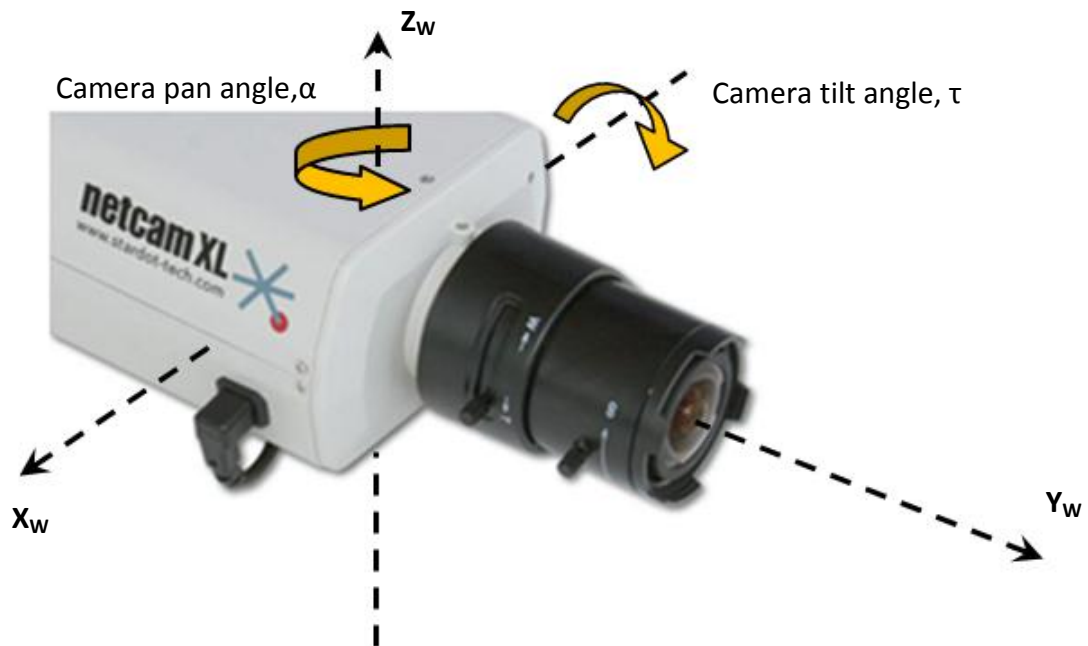


Figure 11: Camera tilt and pan angle

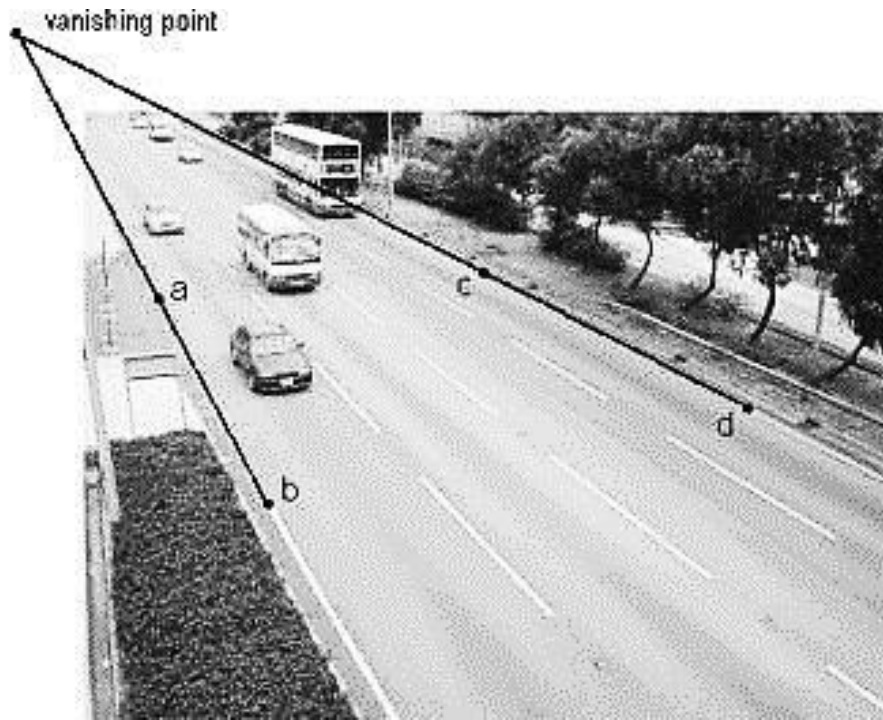


Figure 12: Meeting of parallel lines to find image's vanishing point (Yung *et al*, 2001)

With the coordinates of the vanishing point found, the focal length of the camera, f can then be calculated using:

$$f = -\frac{i_{y\text{van}}}{\tan(\tau)} \quad (11)$$

where τ is the measured camera vertical tilt angle and $i_{y\text{van}}$ is the pixel on the vertical image axis at which the vanishing point is located

The pan angle of the camera, α , was then determined using:

$$\alpha = -\text{atan}\left(\frac{\cos(\tau) * i_{x\text{van}}}{f}\right) \quad (12)$$

where $i_{x\text{van}}$ is the pixel on the horizontal image axis at which the vanishing point is located

Finally, the following set of projection equations allow us to relate points in the image with coordinates in the world frame:

$$w_x = \frac{-(i_y \sin \alpha + i_x \cos \alpha \sin \tau) h}{\sin \tau (i_y \cos \tau + f \sin \tau)} \quad (13)$$

$$w_y = \frac{-(i_y \cos \alpha + i_x \sin \alpha \sin \tau) h}{\sin \tau (i_y \cos \tau + f \sin \tau)} \quad (14)$$

where w_x = Horizontal distance from centroid in the world frame

w_y = Vertical distance from centroid in the world frame

h = Camera height [m]

However, determining the vanishing point in our current FOV proved to be problematic as the natural parallel lines of the river channel lies perfectly horizontal to the frame and will therefore never meet at infinity as prescribed by this method. An attempt to circumvent this was made by utilizing parallel lines present on the soccer field within our FOV, as attempted in Figure 13.

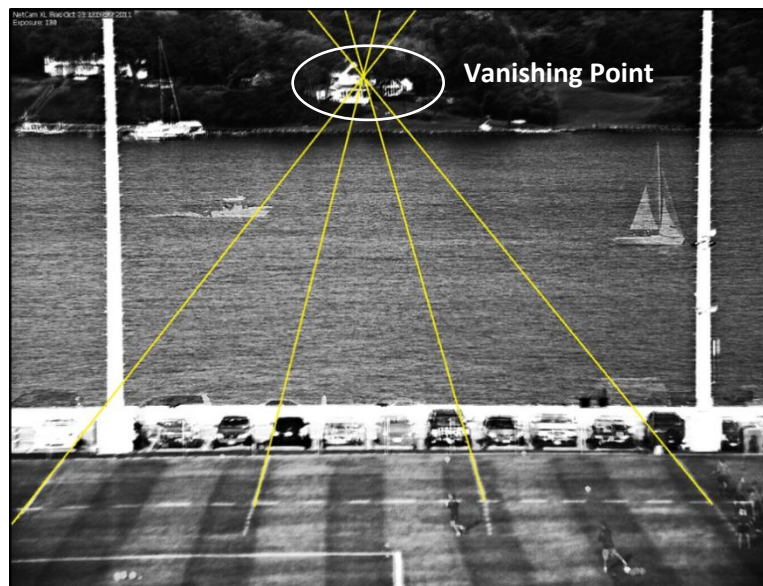


Figure 13: Determining the vanishing point using parallel field lines

In this attempt, the image coordinates of the vanishing point were found to be:

$$\begin{aligned}i_{xvan} &= -47 \text{ pixels} \\i_{yvan} &= 395 \text{ pixels} \\&\text{(From the image center)}\end{aligned}$$

The ‘vanishing point’ method proposed by Kivanc Bas & Crisman works well for traffic monitoring on land in the presence of long, parallel lane lines for easy calibration. However, the use of the shorter parallel soccer field lines was found to produce significant degrees of error when evaluated. 50 still images of the USNA Yard Patrol (YP) crafts (L=31.3m) were measured using the vanishing point method and an average error of 9.6% was observed.

The Trigonometric Projection Method

A new camera calibration method was therefore proposed and evaluated. We derive a trigonometric relationship between fixed, stationary objects in the image and their corresponding real world coordinates found using GPS coordinates. Camera characteristics, such as focal length and camera tilt angle, were not considered in this approach. Figure 14 illustrates a sketch of how this trigonometric relationship was defined.

We first define the upper (far end) and lower edge (seawall) of the river channel within the image as Points P_1 and P_2 respectively. The distance between these two points can be measured in pixels from the image frame itself. In this scenario, P_1 can be found at row 730 and P_2 is at row 220, as shown in Figure 15a. In other words, these two points, P_1 and P_2 , are separated by a total 510 pixels. Using GPS readings, we measure the same width of the channel represented by these two points to be at $Y_1=153.0\text{m}$ and $Y_2=793.8\text{m}$ away from the camera origin, as shown in Figure 15b. The actual width of the channel can therefore be found from the difference to be 640.8m apart, represented by vertical 510 pixels in the image frame.

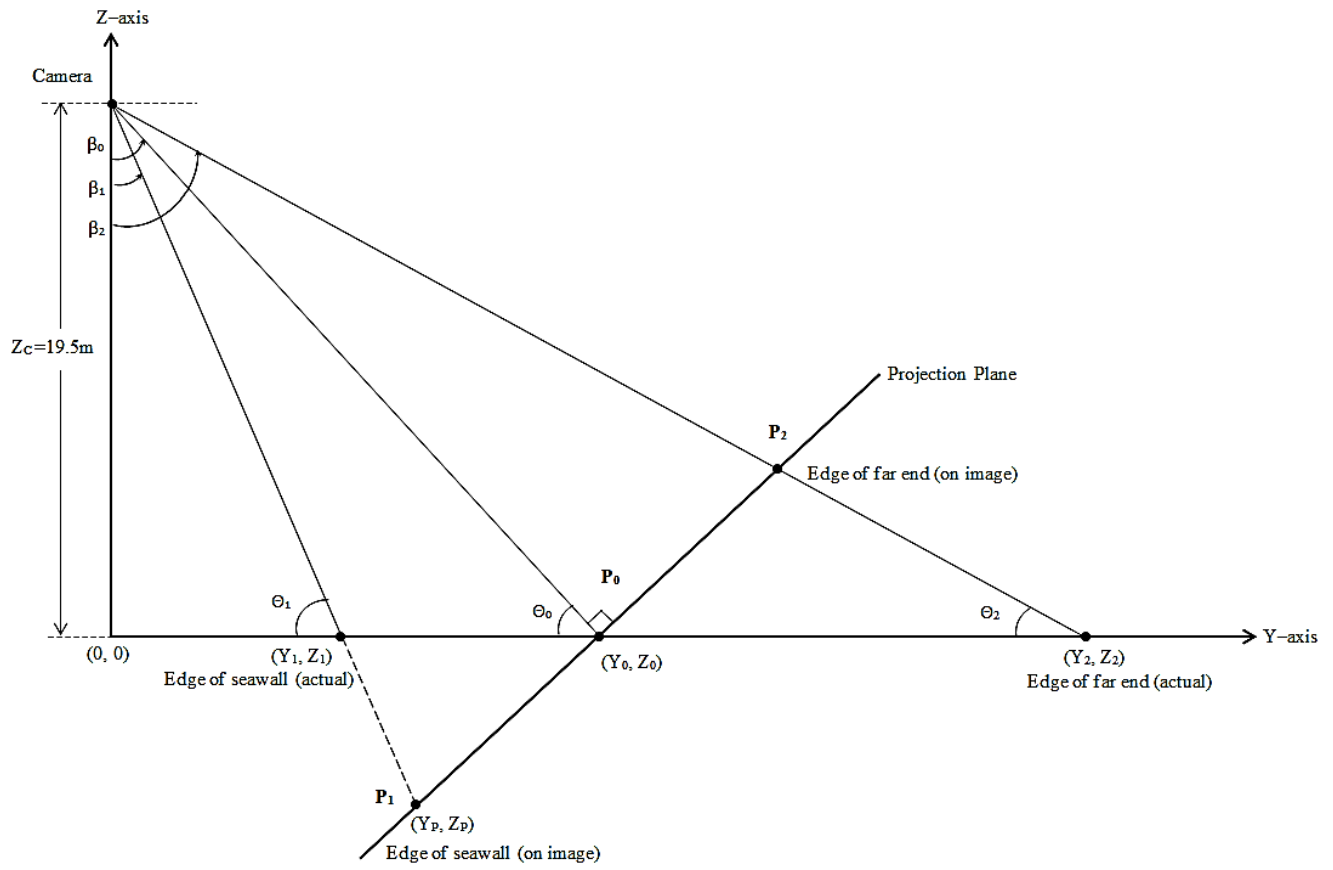


Figure 14: Trigonometric calibration setup

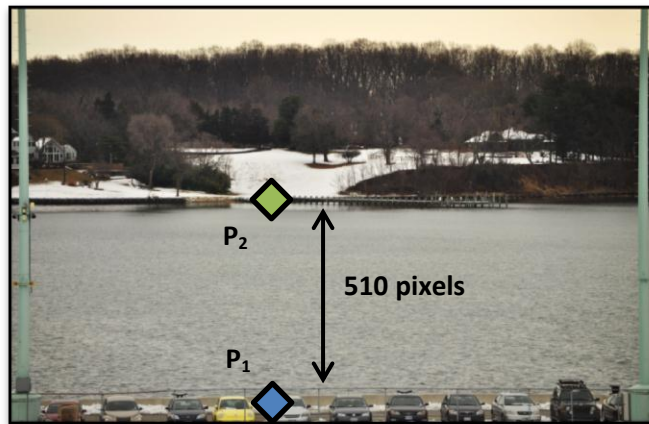


Figure 15a (Left): Project image plane [pixels]

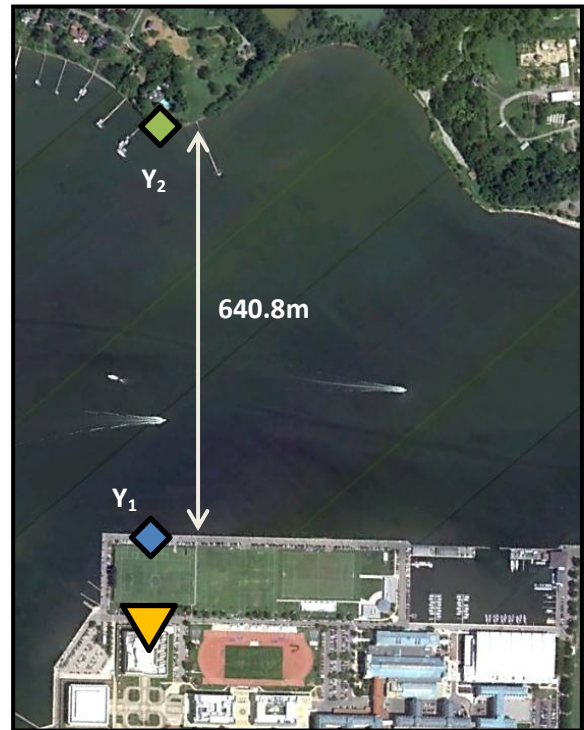


Figure 15b (Right): Real world axis [m]

When we assume a hypothetical midpoint, P_0 that is located equidistant from both P_1 and P_2 in the image, it can be observed that the relationship between pixel number and actual distance from the camera is not a proportional one; The actual distance between Y_2 and Y_0 is larger than that between Y_1 and Y_0 , even though they are represented by the same number of vertical pixels (Figure 16).

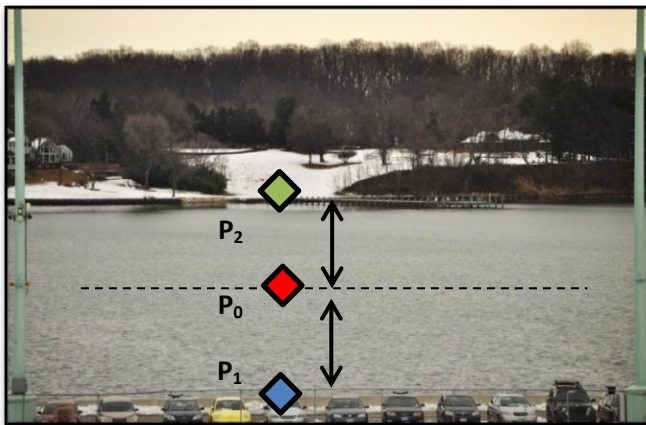
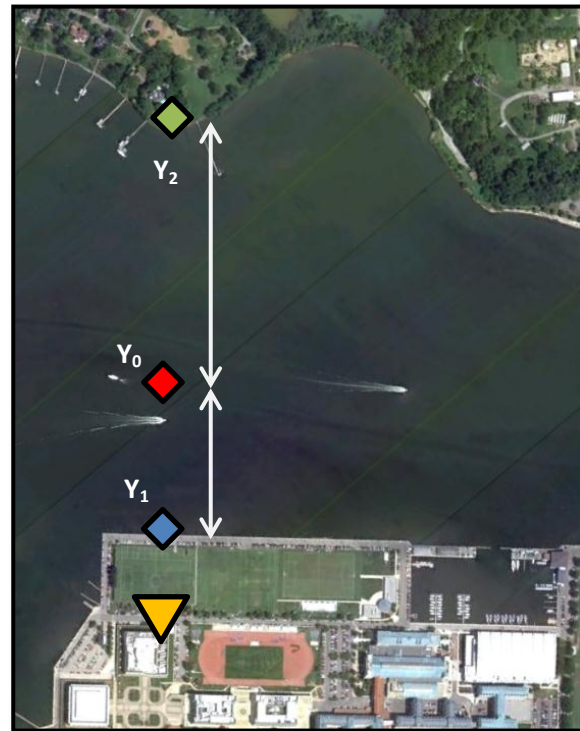


Figure 16a (Left): P_0 on image plane [pixels]

Figure 16b (Right): Y_0 on the real world axis [m]



If we look at the highlighted yellow triangle in the same diagram (illustrated in Figure 17), we find that since both Z_C and Y_1 are known, and are fixed throughout the duration of data collection, the corresponding angle β_1 can be found. Using known values Z_C and Y_2 , β_2 can be derived as well.

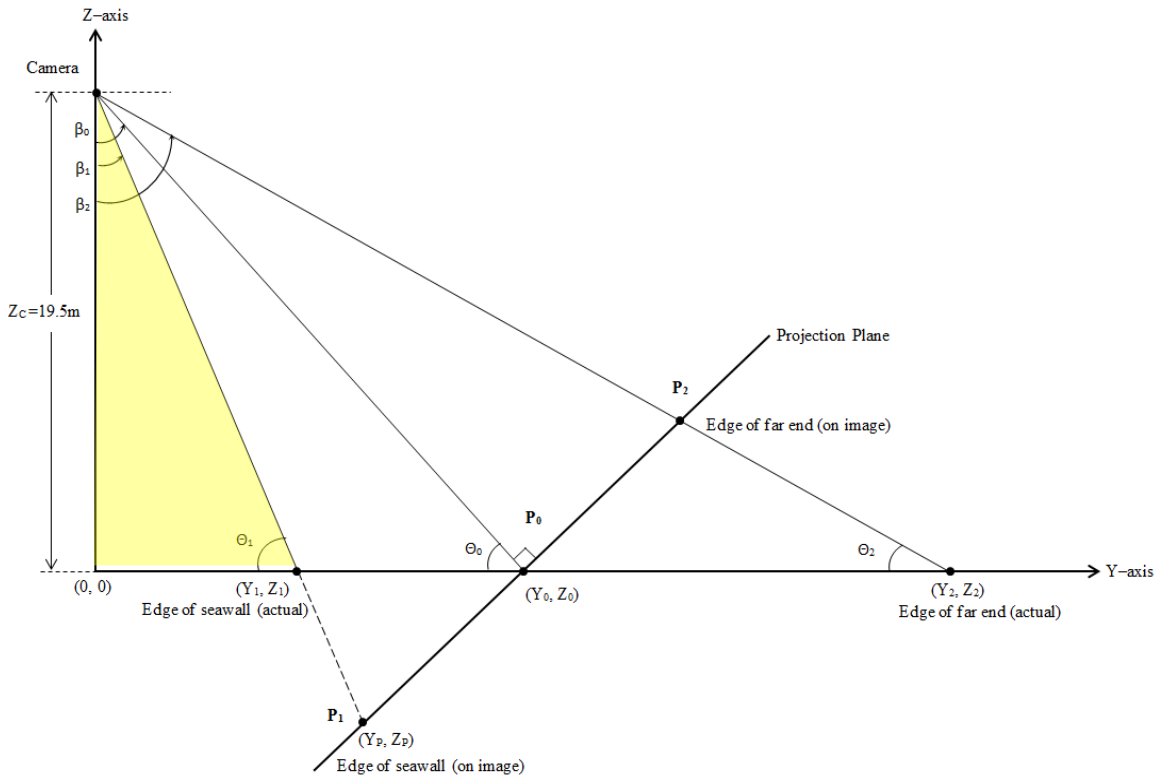


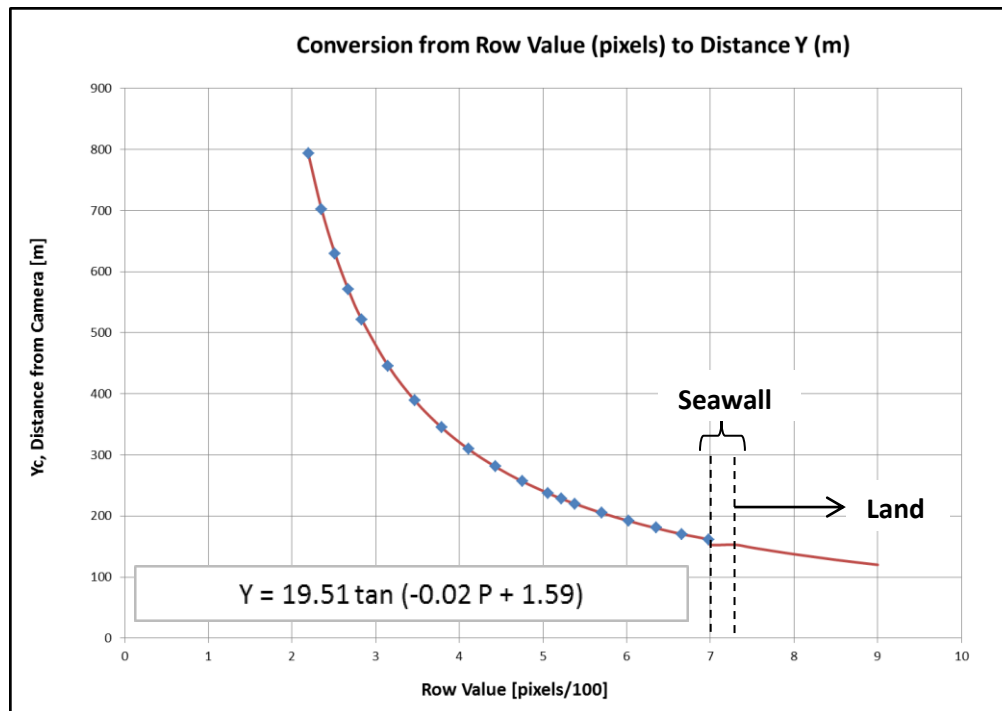
Figure 17: Utilizing trigonometric relationships to find unknown, Y_0

Finding angles β_1 and β_2 is useful as it allows us to determine β_0 which is given by the average of the first two angles. With β_0 and Z_C found, the actual distance of Point P_0 from the camera, Y_0 , can be calculated. As demonstrated by the short example above, the actual or real world distance of Point P_0 from the origin can be found by assuming that the image project plane and the real world horizontal adopt a similar triangle relationship.

By further bisecting the points between P_0 and P_1 , and subsequently P_0 and P_2 , the distance of those points from the camera can be derived. A total of 10 such iterations were calculated, giving us a total of 21 points (or pixel row number), 10 on either side of the original P_0 . For each of these points, the distance Y from the camera origin was calculated using trigonometric relationships similar to how Y_0 was originally derived. A curve (Figure 18) was then fitted through these points, allowing us to draw a relationship between pixel row number, P , with its actual distance, Y , from the camera. Data points obtained are shown in Table 2.

Table 2: Data points used for calibrating P and Y

	Actual Pixel No, P	Modified Pixel No. (P/100)	Relative Pixel No. (From P ₀)	β [deg]	β [rad]	Y, distance from cam [m]
P ₂	220	2.2	255	88.59	1.546	793.76
	235	2.35	239	88.41	1.543	702.38
	251	2.51	223	88.23	1.540	629.86
	267	2.67	207	88.04	1.537	570.90
	283	2.83	191	87.86	1.533	522.02
	315	3.15	159	87.49	1.527	445.68
	347	3.47	127	87.13	1.521	388.79
	379	3.79	95	86.76	1.514	344.76
	411	4.11	63	86.39	1.508	309.66
	443	4.43	31	86.03	1.501	281.03
P ₀	475	4.75	0	85.66	1.495	257.22
	506	5.06	-31	85.30	1.489	237.12
	522	5.22	-47	85.11	1.486	228.19
	538	5.38	-63	84.93	1.482	219.91
	570	5.7	-95	84.56	1.476	205.02
	602	6.02	-127	84.20	1.470	192.00
	635	6.35	-160	83.83	1.463	180.52
	666	6.66	-191	83.47	1.457	170.32
	698	6.98	-223	83.10	1.450	161.20
	700	7	-225	82.73	1.444	153.00
P ₁	730	7.3	-255	82.73	1.444	153.00

**Figure 18:** Conversion from row number to distance Y

Since the distance between the camera and the seawall is occupied by land, pixels located within this region will not be utilized in future calculations. The origin of the final projected equation is therefore adjusted by a value of 153m to give the final calibration plot and equation as shown below:

$$Y = 19.51 * \tan(-0.02 i_y + 1.59) - 153 \quad (15)$$

where i_y is the vertical row number/100 (originally termed P), Y = actual distance from the camera in meters

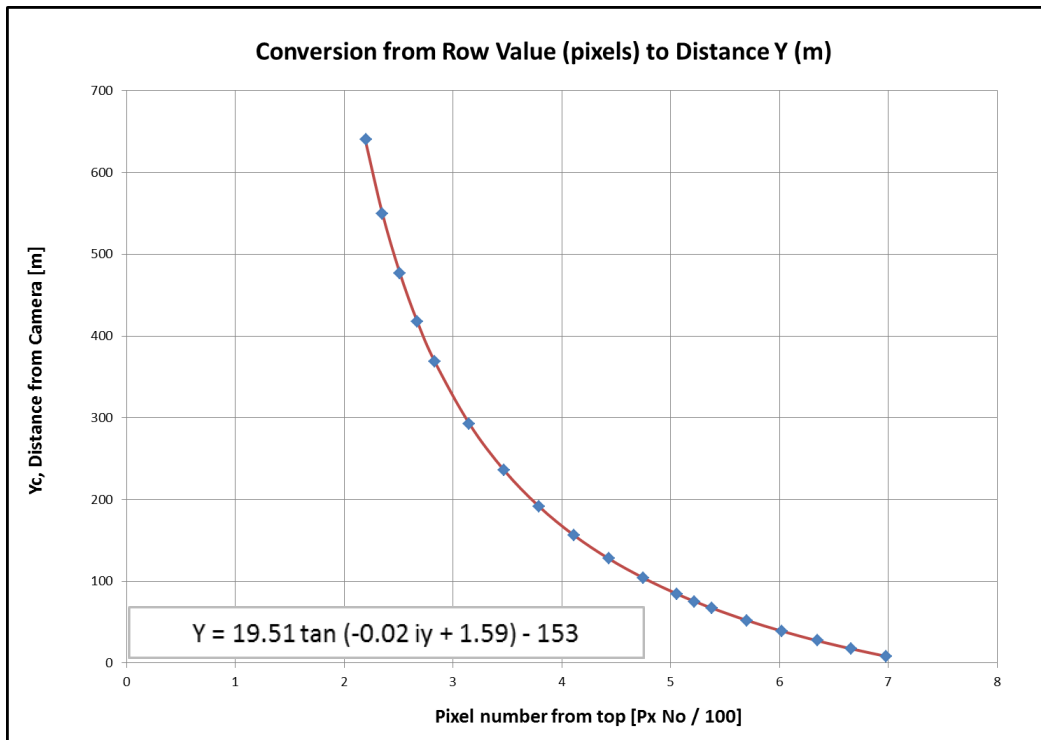


Figure 19: Conversion from row number to distance Y (corrected)

As the distance from the camera, Y increases, it was also observed that the pixel magnitude represented by each pixel in the horizontal x -domain increases as well. A vessel will be represented by fewer pixels (appearing smaller) at a low i_y value as compared to a vessel of

similar size at higher i_y values which will cover more pixels (appearing bigger). To quantify this relationship, the horizontal distance between two fixed stationary points, such as the bollards along the sea wall, were measured in both pixel widths and meters. The row values i_y of the two points being measured were also recorded. Table 3 shows a summary of the stationary points measured.

Table 3: Preliminary values of x_{mag}

Type	i_y	γ	Actual Width [m]	Pixel Width [no. of pixels]	x_{mag} [m/pixel]
Bollards	0.82	-19.3	9.15	380	0.0666
Soccer Field Lines	0.78	-11.4	22.70	874	0.0762
Lamp Post Base	0.79	-12.8	27.24	1044	0.0806

By dividing the actual widths by the number of pixels it takes to represent it on the image, the length magnitude per pixel, x_{mag} , can be derived. However, preliminary values of x_{mag} obtained were sparse and were mostly close to the camera. They are therefore insufficient for establishing a credible projection equation in the horizontal x -domain.

To improve our projection equation, the waterline lengths of the USNA Yard Patrol Crafts (YP) were measured from still video images in pixel widths. By assuming that the YP waterline length remains relatively constant at the known value of 31.3m (ignoring deviations due to draft changes), the x_{mag} values at various i_y were obtained. A total of 50 still images of the YP at various locations within the image frame were used as part of this calibration process and the measurements were added to Table 3 above.

The corresponding plot and projection equation was found to be:

$$x_{mag} = 0.3918 * i_y^{-1.3237} \quad (16)$$

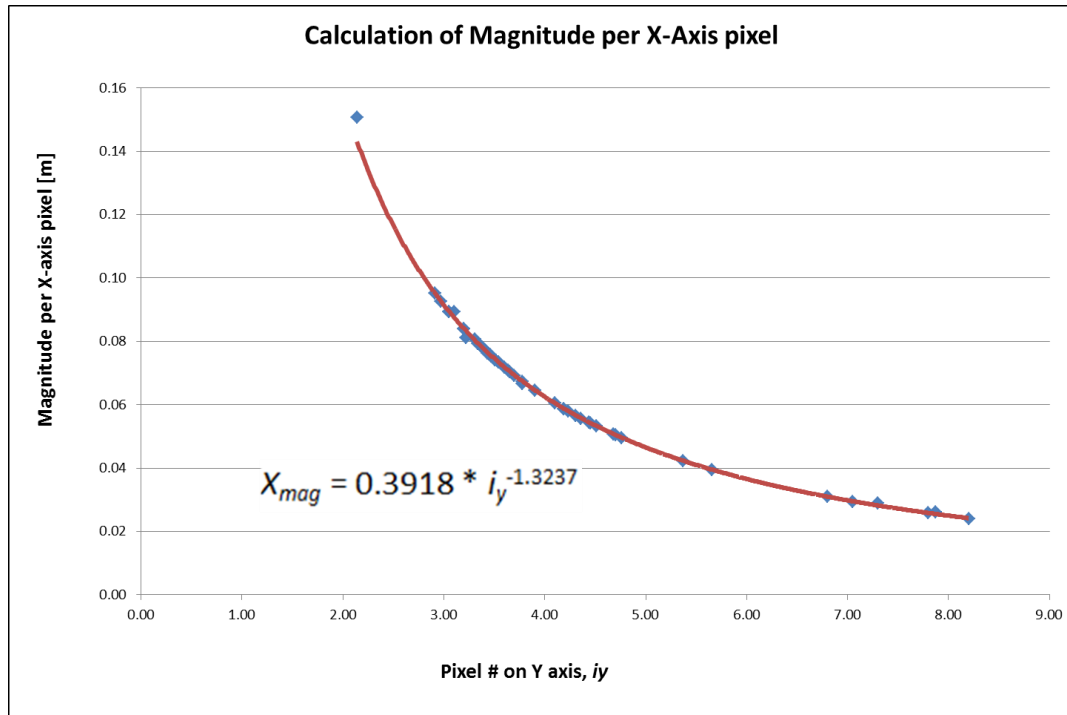


Figure 20: Relationship between x_{mag} and i_y

The length magnitude between any two pixels in the real world horizontal axis, W_X , can therefore be calculated by multiplying the difference in pixel column values by x_{mag} . In other words, by multiplying differences in pixel column number of the bow and the stern of the vessel with the corresponding x_{mag} value at a given i_y , actual vessel length in meters can be obtained.

Evaluation of Calibration Methods

Comparing both methods by measuring the length of a standardized YP craft, the trigonometric projection method was found to be more reliable (1.13% mean error with a standard deviation of 0.43m) in producing an accurate measurement of vessel length as compared to the vanishing point method (9.60% mean error with a standard deviation of 3.52m)

The inaccuracies of the vanishing point methods were largely due to the lack of a reliable pair of parallel lines within the image to determine the exact vanishing point of the camera. The thickness of the soccer field lines (Figure 13) used and its possible curvature are factors that affect the angles of the lines drawn and hence the determination of the vanishing point. Since an accurate measure of the camera's vanishing point cannot be obtained, this method was not used for further measurements.

In conclusion, the trigonometric projection method proved to be a more robust method of calibration and was subsequently adopted for computing measurements within the vessel tracking tool.

3.4 AWAC Profiler Setup

The primary instrument used for wave data collection is the Nortek Acoustic Wave and Current Profiler (AWAC). The AWAC utilizes an Acoustic Surface Tracking (AST) algorithm to detect variations in the surface water elevation, much like how a depth sounder maps a bottom contour using acoustic beams. A short acoustic pulse is transmitted vertically to the water surface and the time difference between the transmitted pulse and its reflection is subsequently used to generate a time series of the surface elevation, as shown in Figure 21.

The AWAC can be deployed remotely for extended periods of time. The duration of its deployment cycle is limited by both battery life and internal memory space (2MB). Both of these are influenced by the deployment sampling rate and sampling interval, which can be configured before the deployment phase by using the accompanying AST software.

In the field testing phase of our study, the AWAC gage was attached to a freely rotating gimbal installed onto a steel frame. The gimbal ensures stability while allowing the central acoustic transducer to be oriented to vertical. The total weight of the frame and additional weights was about 20kg, which ensured self-anchoring on the river bed. The height of the transducer above the sea bed was approximately 0.50m.

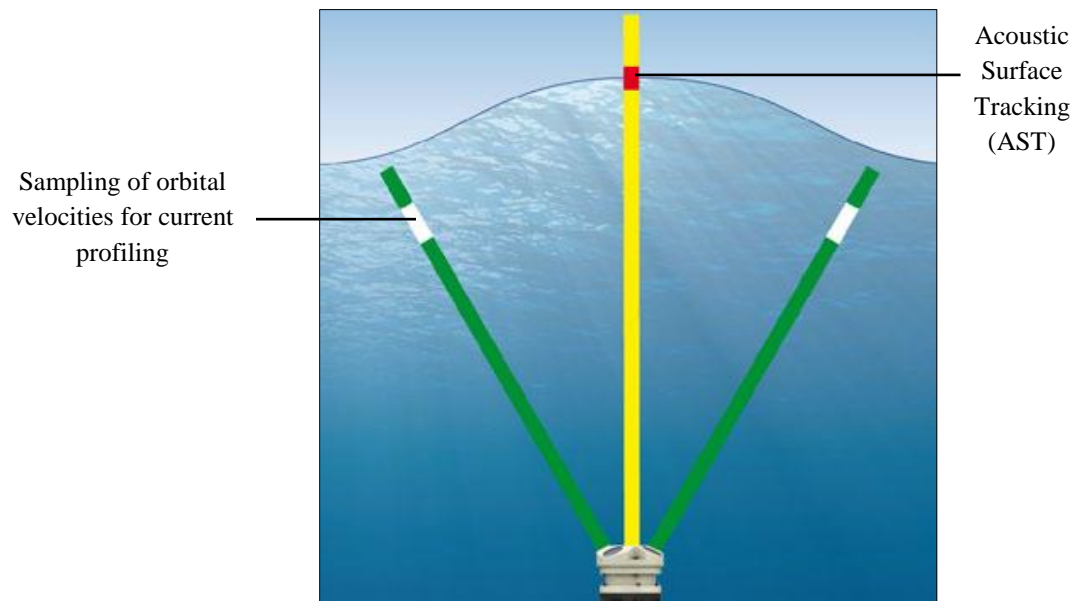


Figure 21: Acoustic Surface Tracking (Yellow Beam) using the AWAC

Advantages of using the AWAC

A major advantage of using the AWAC is that it can collect wave data without causing any obstruction to vessel traffic within the channel. It can be deployed inconspicuously on the river bed, protected from complications at the surface such as harsh weather, vandalism, theft, and ship traffic. The river depth was deep enough for the AWAC to be submerged underwater with more than sufficient clearance between it and the deepest draft vessel expected.



Figure 22: The Nortek AWAC

Limitations of the AWAC

Nevertheless, the AWAC did present some limitations to our study. Designed for long deployments to monitor wave current profiles over long periods of time, the AWAC was not optimized for continuous data collection at high sample rates. Even when optimized for our study, the AWAC had a maximum sampling rate of 4Hz. Despite the possibility of omitting higher frequency waves due to the low sampling rate, the typical frequency of boat wakes (usually within the range of 0.2 – 1.0 Hz, less than the AWAC's Nyquist Frequency of $4/2=2\text{Hz}$) means that they will most likely be captured without significant integrity loss. The AWAC was also programmed to record data in bursts of 512s (8.5mins) during every trigger window of 600s (10mins), with the remaining 1.5min used to process and store the wave data.

In other words, the AWAC wave record is not entirely continuous – it was only in recording mode approximately 85% of the deployed duration. This implied that vessel wakes would not be detected if passed over the AWAC during remaining 15% of the time. Nevertheless, this shortcoming was deemed to be acceptable given the large number of vessel passages expected.

When deployed, the AWAC was configured to collect wave data at a rate of 4Hz. The sampling time was 8.5 minutes every 10 minutes, thus creating 2048 data points for each record. The AWAC was lowered into position and retrieved by a three man team onboard a small USNA owned Zodiac Rigid Hull Inflatable Boat (RHIB) in the vicinity of the College Creek area, at a distance of 61.0m (or 200ft.) extending parallel outwards from the left-most edge of the same seawall shown in the camera FOV, at depths of approximately 5.5m (18.0ft). At this depth, the vessel-generated waves will be classified as deep water waves. The rationale behind its location within the mouth the College Creek bay away from the seawall is to reduce the effect of waves reflected off the seawall from cluttering the actual vessel wake.

3.5 Wave Logger Setup

The Ocean Sensor Systems Wave Logger was selected as a secondary wave data collection instrument, initially to augment the data collect by the AWAC. It is a surface-penetrating device that measures continuous changes in the water elevations over time at much higher sampling rates of up to 30Hz. Similar to the AWAC, it can be configured easily with accompanying software available off the public site of Ocean Sensor Systems. Its biggest advantage over the AWAC for continuous wave measurements implies that no vessel-wake

events will be omitted and discounted during the experimental data collection phase. However, due to the need for a supporting frame, the wave logger has a greater logistical requirement associated with its deployment. Since the protruding frame did pose an obstruction to vessel traffic, it can only be deployed for short durations during the day and required constant manning, unlike the inconspicuous nature of the AWAC.

The deployment site of the wave logger was approximately 10ft further to the left of the AWAC, parallel to the seawall. A 6.10m (20ft) tall lightweight aluminum frame was constructed with the aid of the USNA Hydromechanics Lab for this purpose. The frame was designed for quick deployment and retrieval in mind. It is portable enough to be deployed by a one to two man team onboard a Zodiac RHIB while concurrently providing sufficient vertical stability while recording wave measurements.

To ensure consistency between measurements taken by both the AWAC and the wave logger, a series of calibration tests were conducted in the 120' and 380' wave tanks using both instruments, as well as two other independently calibrated wave gages used by the USNA Hydromechanics Lab - the RBR Capacitance Wave Gage and the Sonic Wave Probe, respectively. During this calibration process, the instruments were exposed to waves of frequency ranges of $f = 0.3 \sim 0.8\text{Hz}$ ($T = 1.25 \sim 3.75\text{s}$) as well as a set of random JONSWAP wave spectrum. Results show that both the AWAC and the wave logger are accurate when compared to the independently calibrated RBR capacitance gage and sonic wave probe.



Figure 23: Wave Logger deployed at the mouth of College Creek - Annapolis, MD



Figure 24: 6.1m (20ft) Aluminum frame used to deploy the wave logger

CHAPTER 4 – VIDEO PROCESSING

4.1 Overview

The use of remote cameras and other imaging devices to document vessel traffic activity is not unprecedented. Past studies have utilized video recordings and Synthetic Aperture Radar (SAR) imagery as a means to investigate vessel wake relationships. However, they are generally used to visually link a wake event with its corresponding vessel, as demonstrated in Houser (2011). In Houser's study, cameras were set to record images at 1 min intervals throughout the day, while representative properties of the vessels, such as their speeds and lengths, were measured using other instruments or gathered from Coast Guard vessel records. Others, such as Sullivan and Shah (2008), utilized computer vision techniques for tracking vessels to design visual vessel surveillance and classification for port security purposes.

Traditional detection and tracking of moving objects within a video or image frame follows a simplified process as shown:

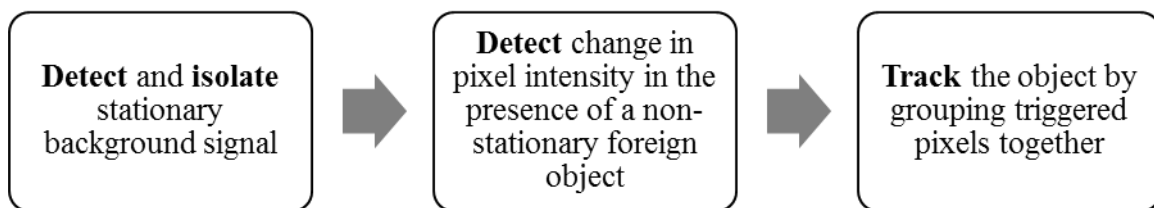


Figure 25: Simplified Flowchart for Vessel Detection and Tracking

To aid further explanation, a summary of key terminologies used in computer vision and image processing is provided below:

- 1) Thresholding – Thresholding is a fundamental step in image processing that converts a color or gray intensity image into a binary mask that contains either a ‘0’ (background) or ‘1’ (foreground). The level of threshold, usually specified by a scalar value, determines the sensitivity level at which objects of interest are detected and separated from the background signal.
- 2) Region Processing – Once the image is passed through the threshold, regions of significance are isolated by applying morphological operations to remove small insignificant regions (known as ‘morphological opening’) or fill up gaps and holes present within the binary image (known as ‘morphological closing’).
- 3) Region Analysis: Bounding Box – The final step of an object tracking process, the bounding box is defined as the smallest rectangular region that contains the region of interest (in this case, the vessel). The dimensions of this box can then be utilized to calculate target parameters, such as vessel length, and the change in position of this box can be used to compute velocity. Placing a size criterion on the bounding box further eliminates unwanted targets.

Vessel tracking along a water body poses unique challenges as compared to tracking moving objects on land. Firstly, the presence of both wind-generated waves and vessel wakes increases the amount of disturbance within a recorded image, making it harder to differentiate moving vessels of interest in the foreground from a non-stationary background. Secondly, a

flowing water body lacks fixed calibration points that can be utilized for camera calibration, which is an essential process if accurate measurements are to be derived from the video footage.

Zhang *et al.* (2009) describes the process of ship detection and tracking using background subtraction, a technique based on detecting change from a background scene. Their study highlights the difficulty in object detection and tracking in many real world applications where the background may consist of moving water surfaces and illumination changes, and subsequently proposes a new approach of segmenting targets with an adaptive threshold. The adaptive threshold as recommended by Zhang *et al.* is calculated using the following equation:

$$TH = \frac{FX - FM}{2} + FM \quad (17)$$

where TH = threshold, FX = the maximum of the frame difference intensity,

FM = mean of frame difference intensity

Using this adaptive threshold, movement in a frame can be detected when compared to a stationary background frame, as demonstrated by Figure 26 a) to c). Morphological operations were then applied to remove noise caused by moving surface waves to produce a clean binary region of interest as shown in Figure 26f.

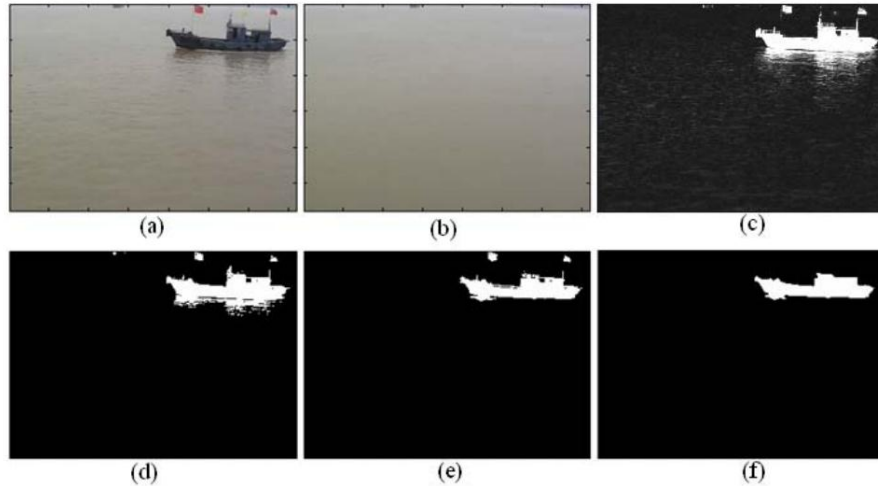


Figure 26: Background subtraction and filters used to detect ship movements (Zhang *et al.* 2009)

Alternatively, another common object detection method, known as Optical Flow Analysis, may be utilized for vessel tracking. Introduced by Horn & Schunck (1980), this method has since been studied widely and commonly applied in computer vision systems, such as those installed for autonomous visual navigation by vehicles and robots. In simple terms, it is a method of estimating a 2D projection of a 3D real world motion by calculating the magnitude and direction of brightness changes between adjacent image frames. Kanawathi *et al.* (2009) conducted a study focused on optimizing parameters for the Horn-Schunck method in MATLAB. Their findings identified the optimum values for MATLAB parameters, namely the number of iterations ($1 < n < 6$) and smoothness level ($0.0001 < s < 0.002$) to produce optimal optical flow results associated with the least amount of error.

4.2 Vessel Tracking Tool

A unique vessel tracking program was developed in this project using the Computer Vision Toolbox in Simulink (MATLAB) in order to achieve the goal of establishing a broad database of vessel types and their associated maximum wave heights. Recorded footage was first downloaded from the StarDot Netcam XL and exported in .avi format at 10 frames per second (fps) in order to provide a valid video input. A summary flow diagram of the simulation program is shown in Figure 27.

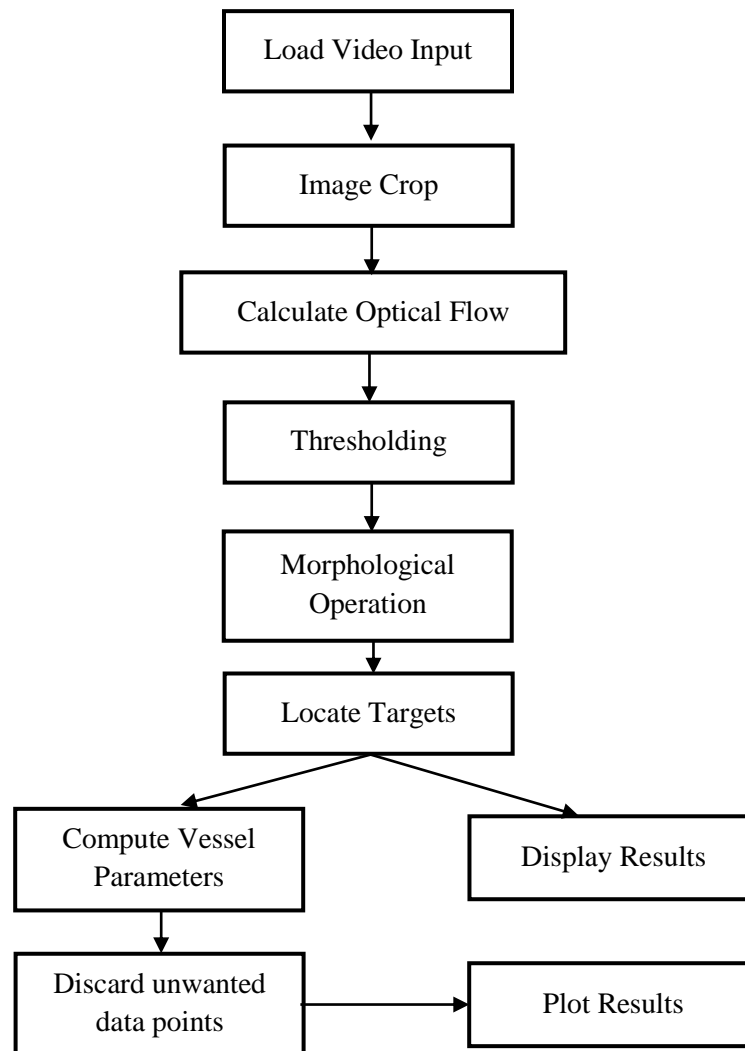


Figure 27: Flow diagram of simulation process

In this simulation file, the input video will first be cropped to include regions within the river channel only. Motion detection was implemented using the optical flow block in Simulink to calculate flow velocity vectors between adjacent video frames. Moving objects within the video frame will be indicated by optical flow velocities above a mean threshold value, and will appear as white binary image against a black stationary background. Motion from surface wind waves and vessel-generated white wash are detected as well, and these disturbances appear as noise which can be filtered out by morphological operations. Finally, the remaining ‘blob’ image, representing the body of the transiting vessel, will be tracked by a bounding box. The parameters of this box region, such as its centroid and major axis length, can then be used to calculate target vessel parameters using the projection equations developed in Chapter 3 Section 3.3. Parameters for each processing step are further detailed in the following section.

Optical Flow Calculation

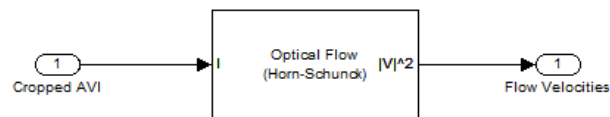


Figure 28: Optical Flow Block

Motion detection was implemented using the *Optical Flow* block. It uses an iterative process to calculate the magnitude of optical flow velocities between two image video frames. In this block, the Horn-Schuck method calculates an estimate of the velocity vector field by assuming that optical flow is smooth over the entire frame. A $[u, v]$ vector is computed for each pixel. In this simulation, the block outputs the optical flow matrix in a ‘magnitude-squared’ form, where each element is of the form $u^2 + v^2$. The smoothness factor was set at a value of 0.02 for optimal results.

Image Thresholding

The next step is to process the video and calculate the ‘background’ or ‘ambient’ motion value of a vessel-free frame. Similar to background subtraction, this calculated ‘ambient frame velocity’ sets the threshold value which enables objects entering the original vessel-less scene to be detected. To accomplish this, the mean velocity over the entire input and the mean velocity per frame (running mean) were calculated. Together, these two blocks compute the mean threshold, which represents the small, ambient motions present in the background (e.g. small surface eddies).

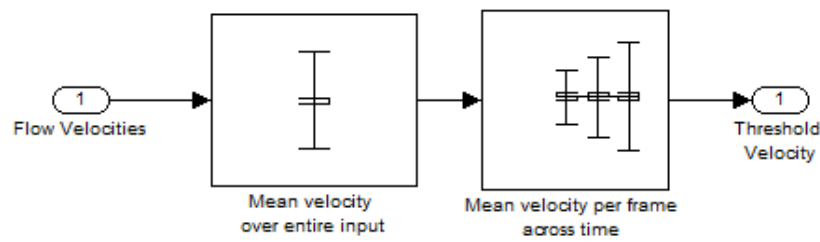


Figure 29: Velocity Threshold Block

Input flow velocities from each new frame were compared against the velocity threshold. In this simulation, an additional gain block was used to provide further sensitivity control over the threshold value, as shown in Figure 27. If this value is high, both the target vessel and a significant amount of background will be detected. Conversely, if the value is small, a small portion of the target vessel might be eliminated. A median filter block then computes a median over a specified neighborhood size (16 by 9 pixels) to produce a binary mask, assigning a ‘1’ value for every pixel that triggered the threshold and a ‘0’ value for those below.

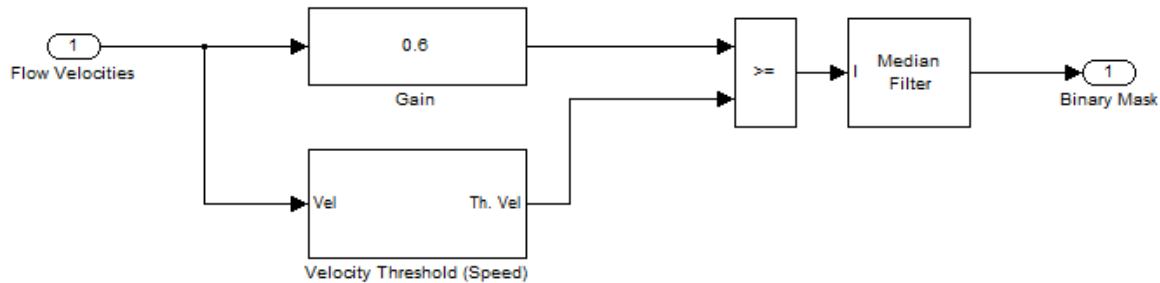


Figure 30: Median Filter Block

Morphological Operation

A challenge presented through this simulation is the issue of separating the vessel body from its wake, especially in cases where the vessel is travelling near its critical speed and its resultant wake is large and turbulent. To remove the vessel wake trailing behind the vessel, morphological operations were used to filter the image. These operations reduce unwanted wake detection and fill holes in the binary image by applying a structuring element. The neighborhood size, and the size and shape of the structuring element, determine which features survive.

A simplified description of common morphological operations is provided below:

Dilation – If binary shape matches the structuring element, the shape is expanded by a pixel magnitude outwards

Erosion – If binary shape matches the structuring element, the shape is shrunk by a pixel magnitude inwards

Opening – Applies erosion followed by dilation on the binary shape. Used when removing noise while preserving overall shape is the priority.

Closing – Applies dilation followed by erosion on the binary shape. Used when filling up gaps within the image is the priority.

In our simulation, morphological opening is performed to preserve the shape of the vessel while removing vessel wakes.

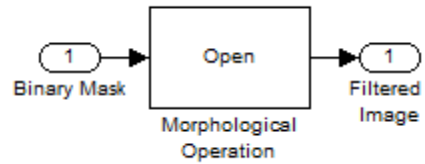


Figure 31: Morphological Opening Block

Figure 32 provides an illustration of the effect of increasing the neighborhood size of the structuring element, while Figure 33 illustrates the effect of modifying the size of the structural elements. The neighborhood size determines the pixel area where the structural element will be applied. A large neighborhood size means that more pixels are included each time an element is applied, producing a better quality picture that will allow more accurate measurements to be made. However, the larger number of pixels involved in each computation means a higher computational cost, and processing time will increase as a consequence.

It is also important to note that not all vessel wakes can be removed using morphological opening. For smaller vessels with a slender side profile, the vessel size and the height of its wake are approximately similar, making it impossible to differentiate them. When such events are detected, the time of occurrence was recorded, and vessel parameters were measured manually instead by locating the relevant pixels (e.g. bow and stern location) in the corresponding image stills.

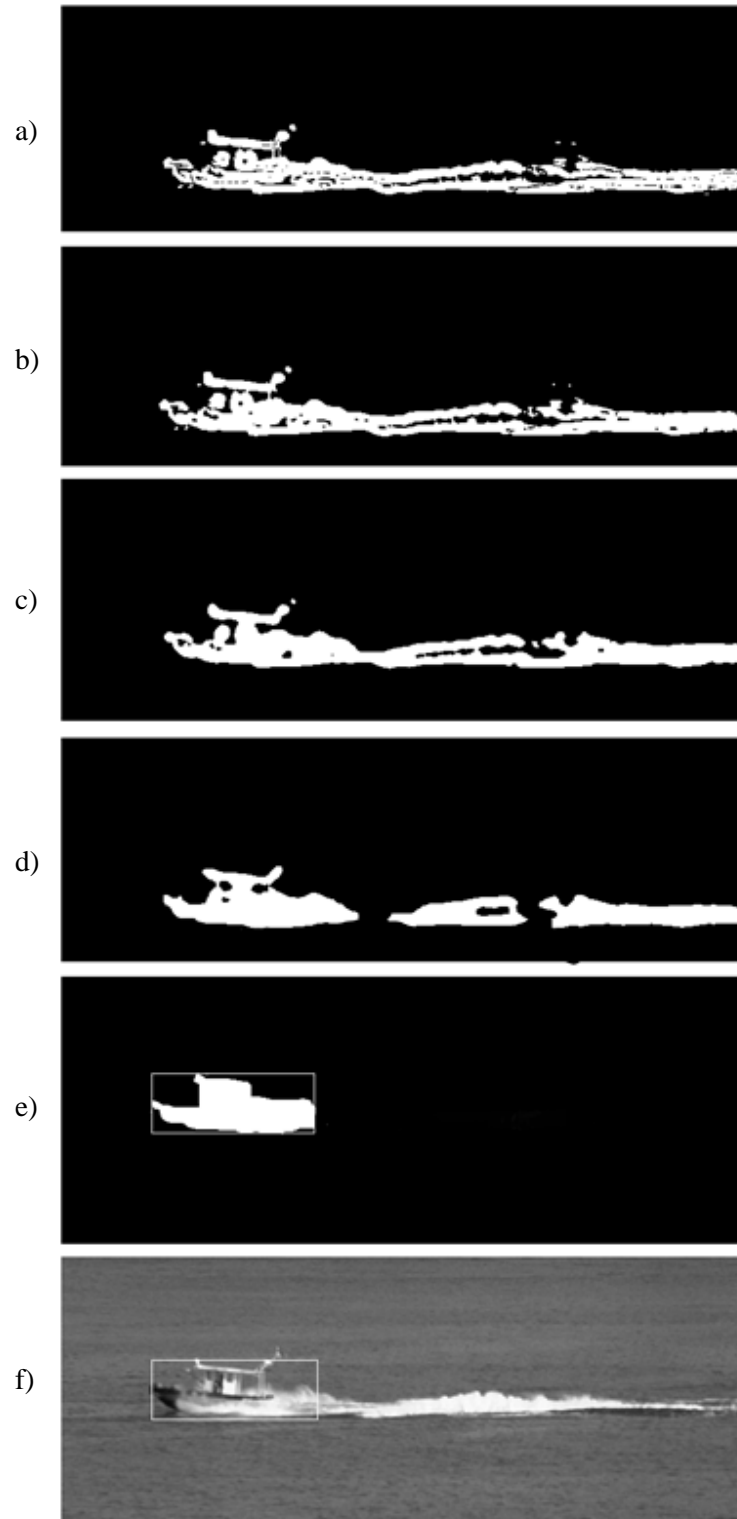


Figure 32: a) to d) Effect of increasing neighborhood size on binary silhouette

e) Bounding box around final tracked target f) Original vessel

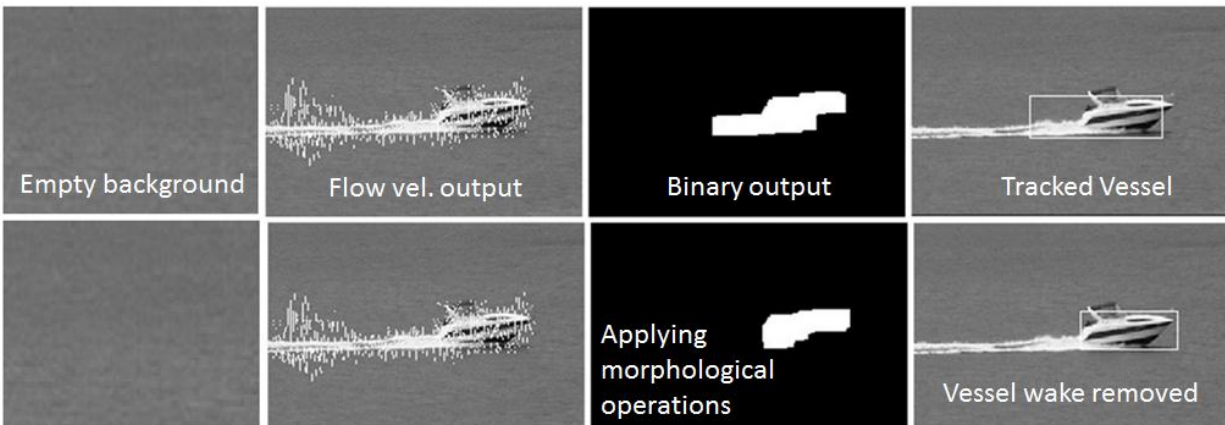


Figure 33: Effect of modifying structural element size to remove vessel wake

Locating the Target

Even after thresholding and applying morphological opening, some binary shapes, or ‘Blobs’, might remain due to remnant wakes and vessel wash left by earlier vessels. The next and final step before a vessel could be tracked is to identify the binary shapes that correspond to real vessel targets. The ‘Blob Analysis’ block in Simulink defines a rectangular bounding box around any input silhouette that meets a preset criteria. It acts as a size filter which further cleans up the image, removing objects that are either too large or small in area.

As vessels closer to the camera are observed to be larger and occupy more pixels than those further away, the video frame is segmented into two, equal horizontal regions to allow appropriate filter limits to be set for each of them. Finally, the outputs for the ‘Blob Analysis’ blocks are obtained, as shown in Figure 34. These values were subsequently used for calculating vessel parameters and will be described later in the next section.

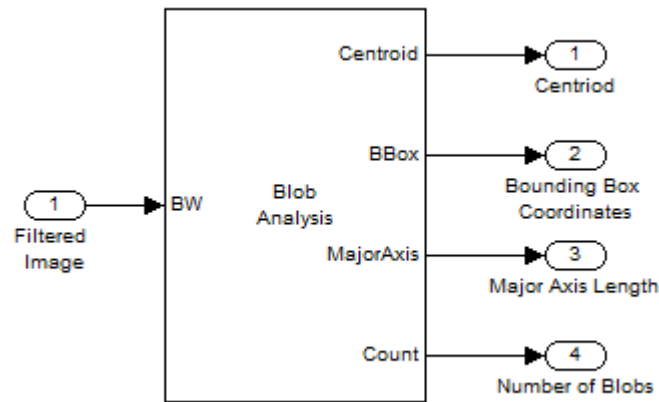


Figure 34: ‘Blob Analysis’ block

Measurements and Outputs

The matrix outputs from Blob Analysis were fed through a subsystem that implements the projection equations (Eqn. 12 & 13) from the camera calibration process, as indicated by the yellow shaded box in Figure 35. Output port 1 of this subsystem (Figure 35) is fed to and overlaid with the original video image. The remaining output ports 2, 3 and 4, contains values for the desired boat parameters – Vessel Length, L_V , Vessel Speed, V_S , and Distance from Seawall, Y , respectively. The computed values were exported at the end of each simulation into the MATLAB workspace for further processing.

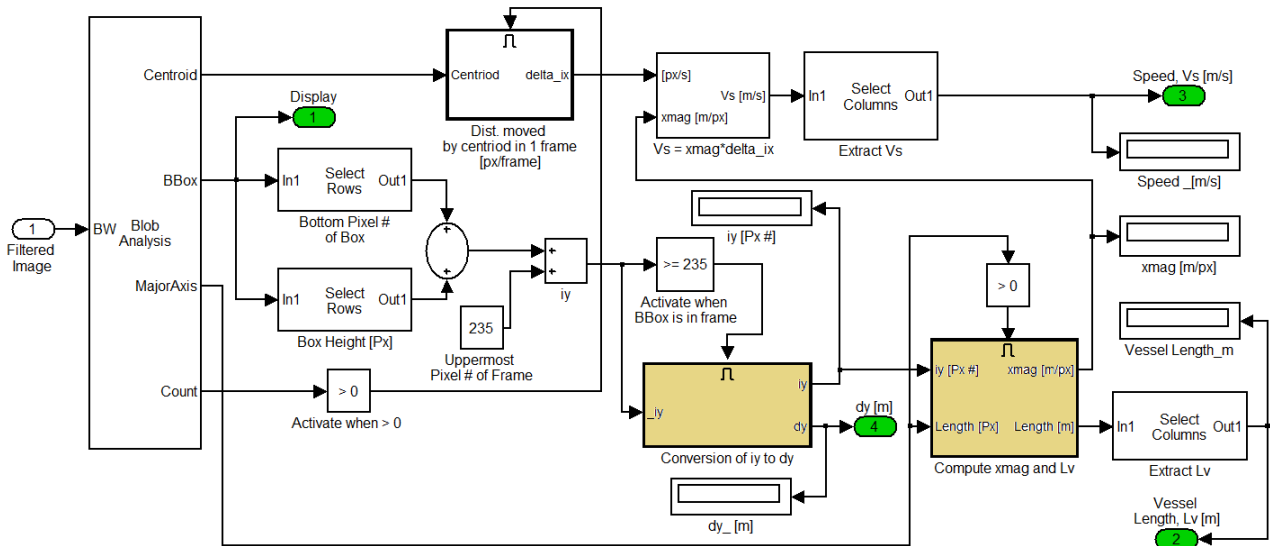


Figure 35: Overview of Measurement Subsystem

This step involved adjusting the data point measured from the video file's time series into real time, by means of a conversion factor that can be found using the video duration. Since a new video .avi file was created for every hour of footage recorded, all .avi files used in the simulation had one hour of recorded footage. However, due to the way the StarDot DVR software handled compression and video frame rate, the actual .avi file duration containing one hour of recorded footage differed slightly. The conversion factor as shown therefore allows the vessel events processed in the video time to be adjusted to real time.

$$convf = \frac{\text{actual time passed (sec)}}{\text{file duration (sec)}} \quad (18)$$

Tracked vessel data were also screened in MATLAB to remove data points that were deemed unsuitable for further consideration due to their lack of wave making effect. This includes vessels that were too small ($L_v < 4\text{m}$), too far away from the camera and the wave gage

($Y > 350\text{m}$), or vessels that were not moving, or were travelling slowly ($|V_s| < 1.0\text{m/s}$), – instances where the vessel-generated waves were too small for detection. Figure 36 and 37 shows a plot of the vessel parameters found before and after applying the selection criterion respectively. The remaining data points also smoothed to give an approximate average reading for each vessel-wake event. As illustrated by Figure 38, the finalized L_v , V_s and Y values can then be read off and compiled into a database.

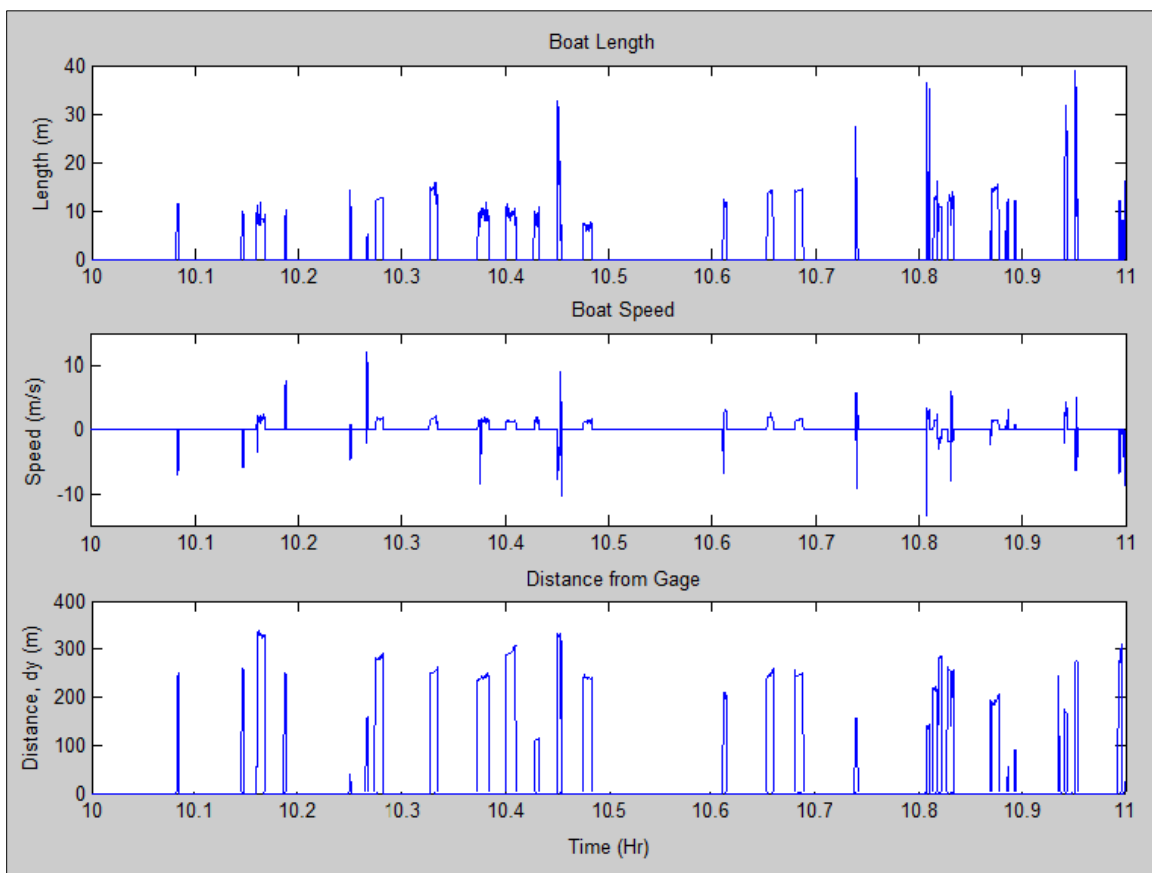


Figure 36: Raw video simulation output

(Positive speed indicates right-to-left travel, while negative speed indicates left-to-right travel)

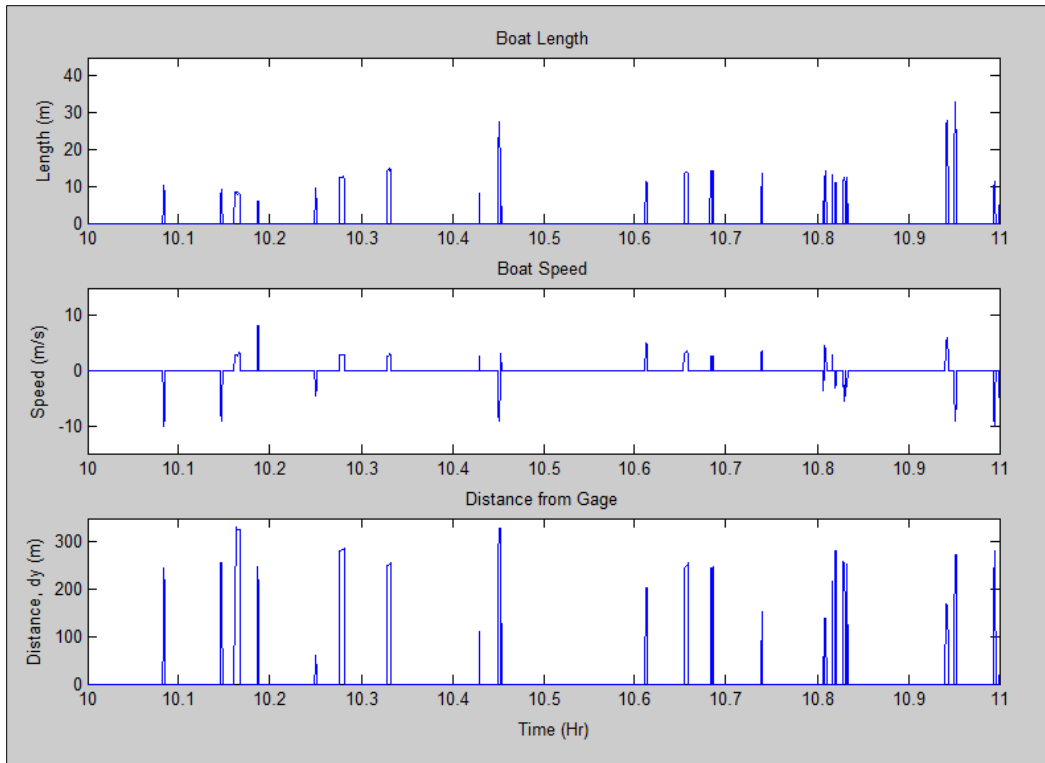


Figure 37: Video simulation output (filtered)

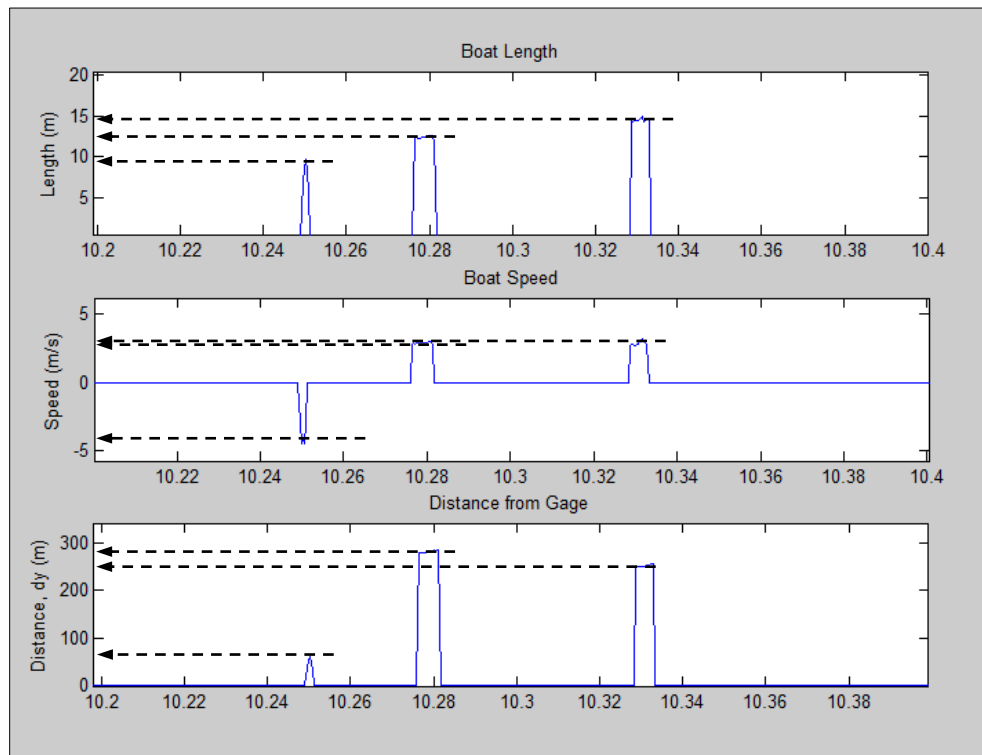


Figure 38: Video simulation output (magnified)

CHAPTER 5 – WAVE FILTERING AND PROCESSING

5.1 Overview

In addition to accurately tracking the vessels of interest and calculating the required parameters, there are also many challenges involved in obtaining the required vessel wave heights in an open channel environment. The uncontrolled process through which vessels were sampled along the river makes it difficult to accurately identify and match each wave disturbance to their respective vessel of origin. Furthermore, smaller boat wakes may even be masked by background wind waves, making it extremely challenging to distinguish them.

While traditional Fourier analysis allows the separation of wave signals into their specific frequencies, the non-linear and non-stationary nature of vessel wakes makes it inappropriate to filter the wave spectrum solely through the use of traditional band-pass filters. In an uncontrolled and open environment, it is also highly likely that the frequency band of the wind waves present and the vessel waves generated will overlap, making the two groups of waves indistinguishable.

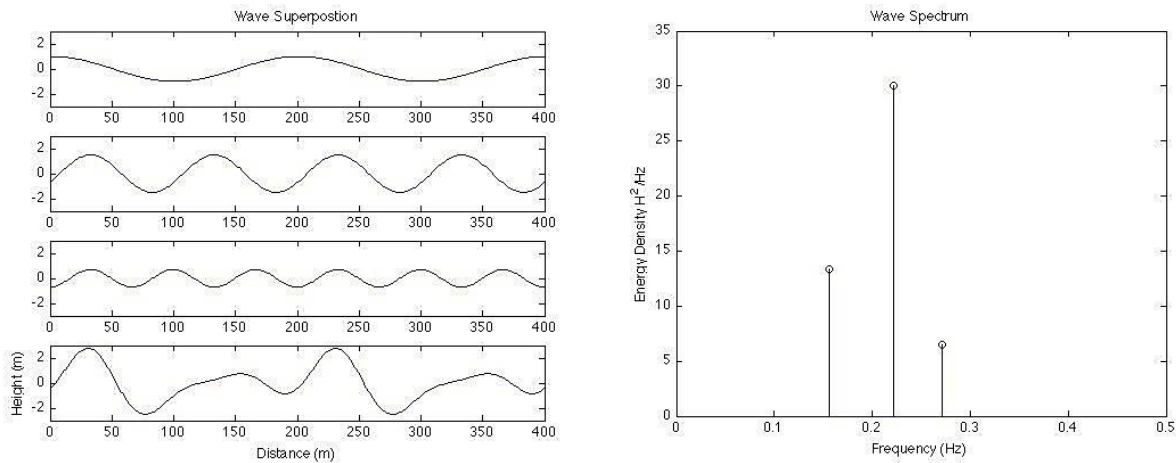


Figure 39a: Example of three distinct and separate wave signals, followed by a resultant combination wave

Figure 39b: The resulted wave is separated using Fourier analysis into its three component signals

(Source: NNMREC Oregon State University)

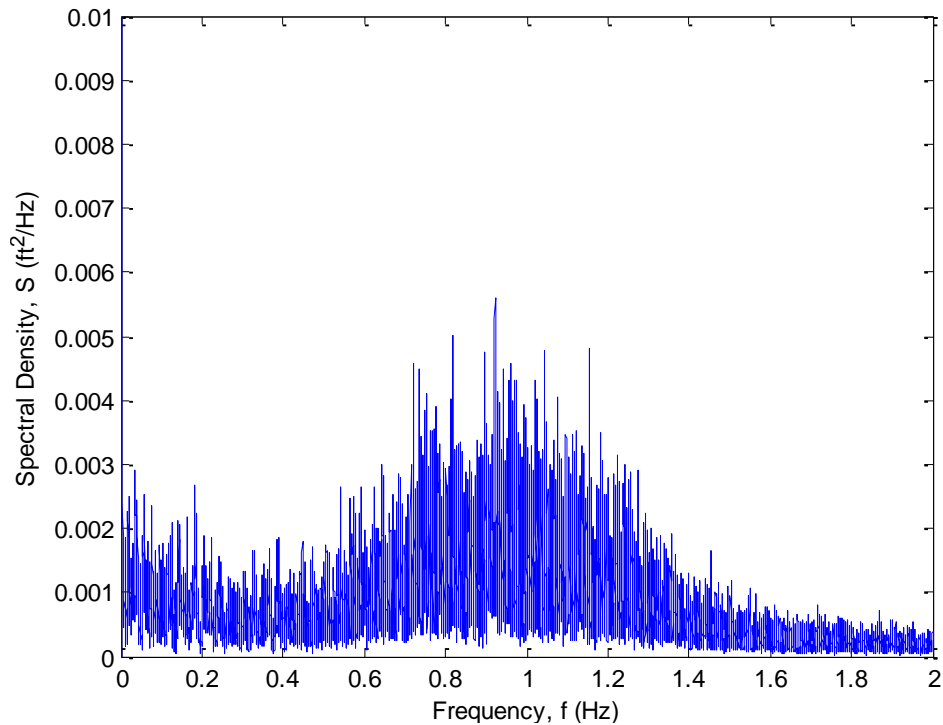


Figure 40: Example of a typical wave frequency spectrum obtained from a single day of wave data collection in an open, uncontrolled environment

Introduction to Wavelet Analysis

Wavelet analysis provides a solution to this problem, and has been utilized in similar open environment simulations in Jensen Beach, Florida (Shermet *et al*, 2011) and Savannah River, Georgia (Houser, 2011). Despite the issue of both wind and vessel-generated waves occupying similar frequency bands, it is still possible to differentiate the two by resolving the wave signal in the time domain. Typically, wind waves are spatially homogenous and stationary over a time scale of the order of 1 day, while vessel generated waves are transient, directional pulses that usually last for 1 minute. Wavelets can therefore be used to quantify such variations present within a spectral signal over a range of temporal or spatial scales (Houser, 2011), highlighting in time the location and duration of these transient vessel wakes.

Similar to Fourier analysis, wavelet transforms decompose the input wave signal and provide a pictorial representation of time-frequency shifts via a scalogram output. The common ‘Morlet’ wavelet, a Gaussian windowed complex exponential, is used to detect local frequency changes within a given signal by amplifying frequency shifts hidden within and representing them on an intensity scale, otherwise known as a scalogram. As illustrated by the scalogram in Figure 41, vessel generated wakes appear as short series of asymmetric disturbances, or ‘streaks’ above the background wind waves, with each wave group having a leading edge of longer, lower frequency waves followed closely by higher frequency waves. This can be explained by linear wave theory, according to which wave celerity, or its speed of propagation, is inversely proportional to the wave frequency in deep water. The lowest-frequency waves of a wave group travel the fastest and they arrive before other, higher-frequency waves.

This observation, which is unique to vessel generated waves, was utilized by Sheremet *et al.* (2011) for their criteria of correctly identifying vessel wakes. In their study, wakes were identified based on the following four distinguishing properties. Figure 42 shows a magnified image of a well-defined vessel wake and its associated characteristics.

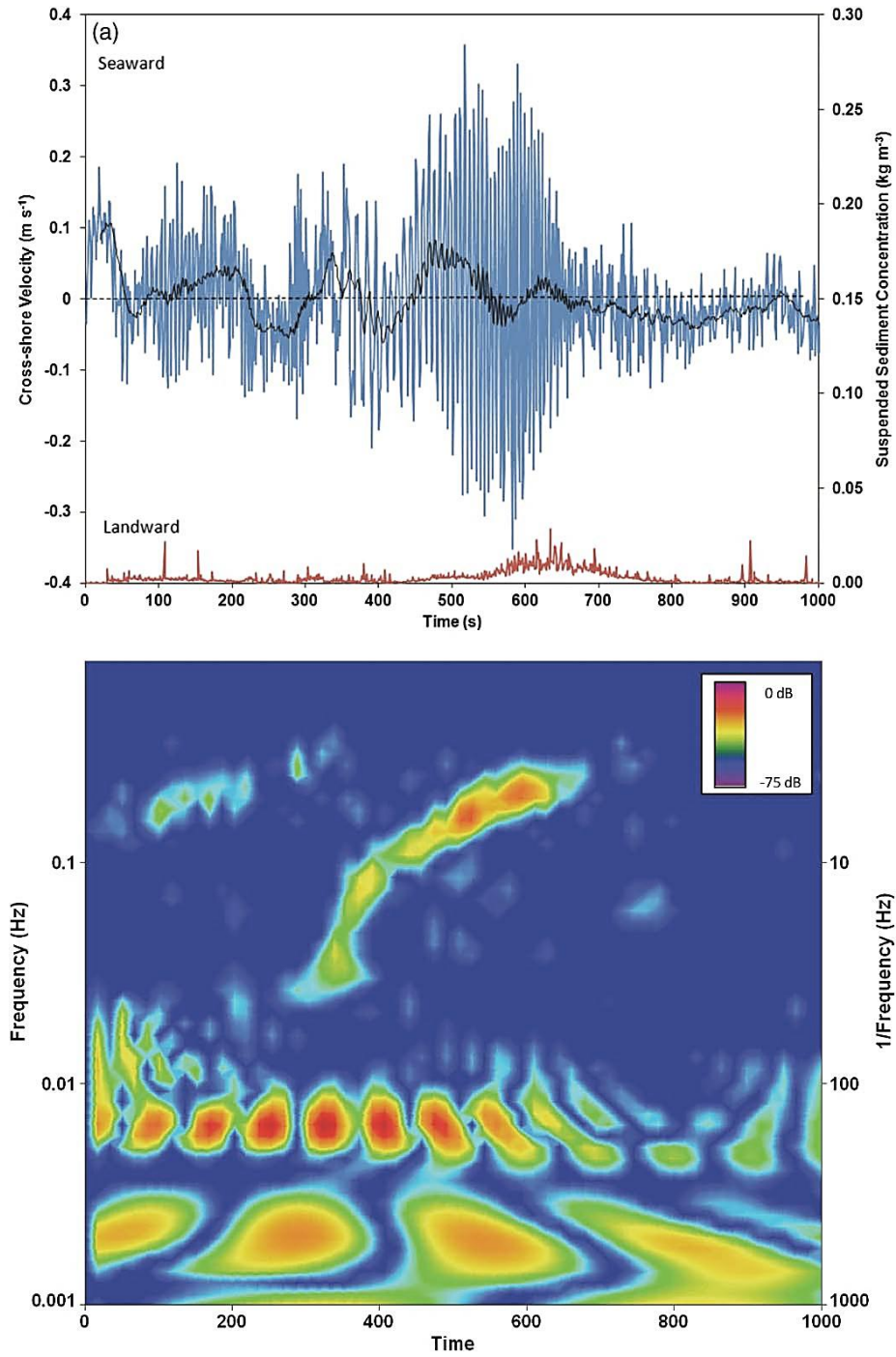


Figure 41: Application of wavelets in the identification of vessel generated wakes (Houser, 2011)

The four distinguishing characteristics of vessel-generated waves are:

- 1) Large Amplitudes – Strong wakes have relatively larger amplitudes and appear as distinguishable disturbances against the ambient waves. However, this method is not applicable when boat wakes have similar amplitudes as the ambient wind waves.
- 2) Low-frequency leading edge – As explained by linear wave theory, the lower frequency waves travel faster away from the point of disturbance (Figure 42, Points A-B)
- 3) Time-Frequency shift – The low frequency waves are closely followed by waves of higher frequencies, causing a stronger return on the scalogram output (Figure 42, Points B-C).
- 4) Correlated pressure and velocity fields – Unlike surface wind waves which generate low pressure signals due to their weak depth penetration, the low frequency leading edge of vessel wakes penetrates deeper into the water. This criterion was not utilized in the current investigation as wave measurements were recorded at deeper waters, resulting in low pressure returns.

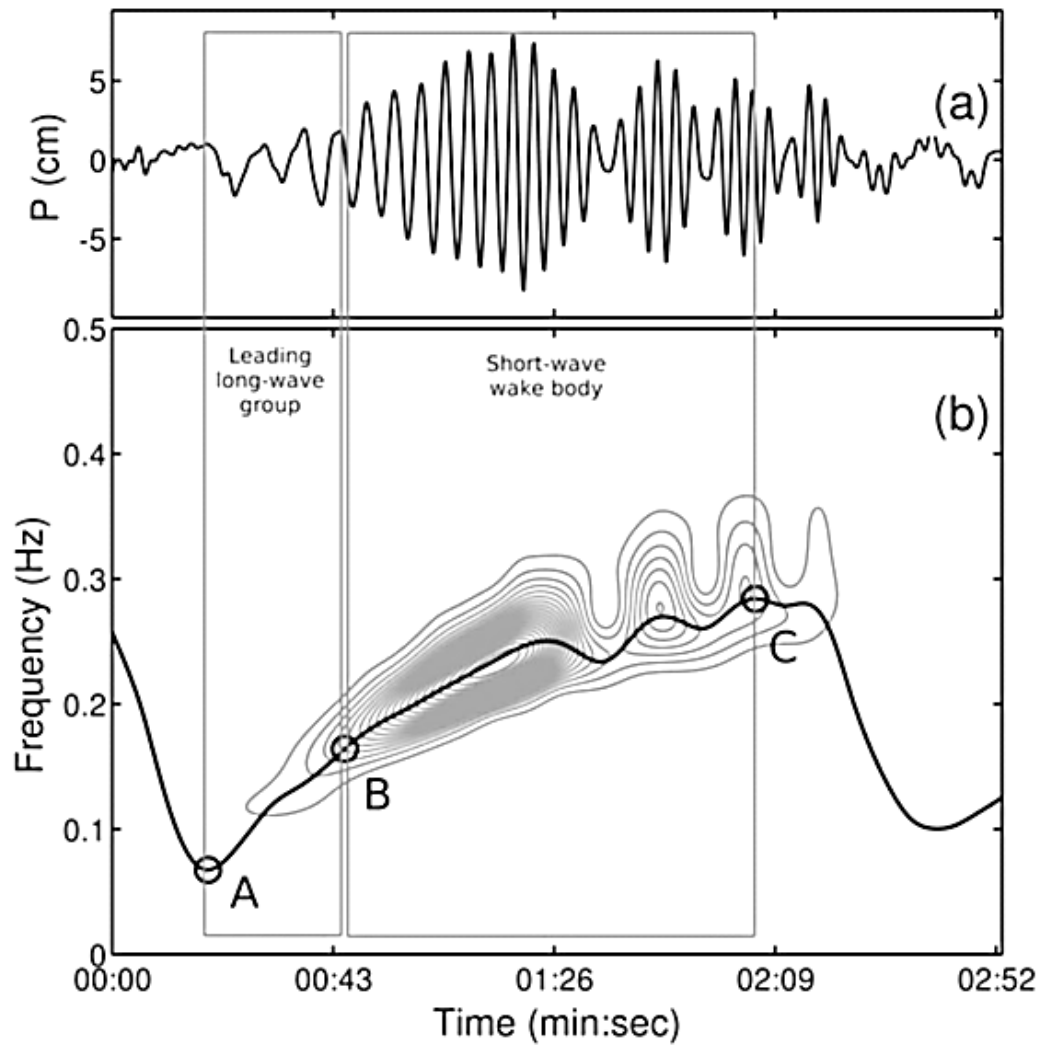


Figure 42: Definitive Characteristics of a Vessel-generated Waveform (Sheremet *et al*)

5.2 Wave Processing Methods

Overview

To establish the database of vessel-general wave heights and boat parameters, wave height measurements recorded by the AWAC were first treated by the following process to remove tides and other anomalies. The resulting wave plots and wavelet scalograms were then analyzed to identify and match the wake events with their respective vessels.

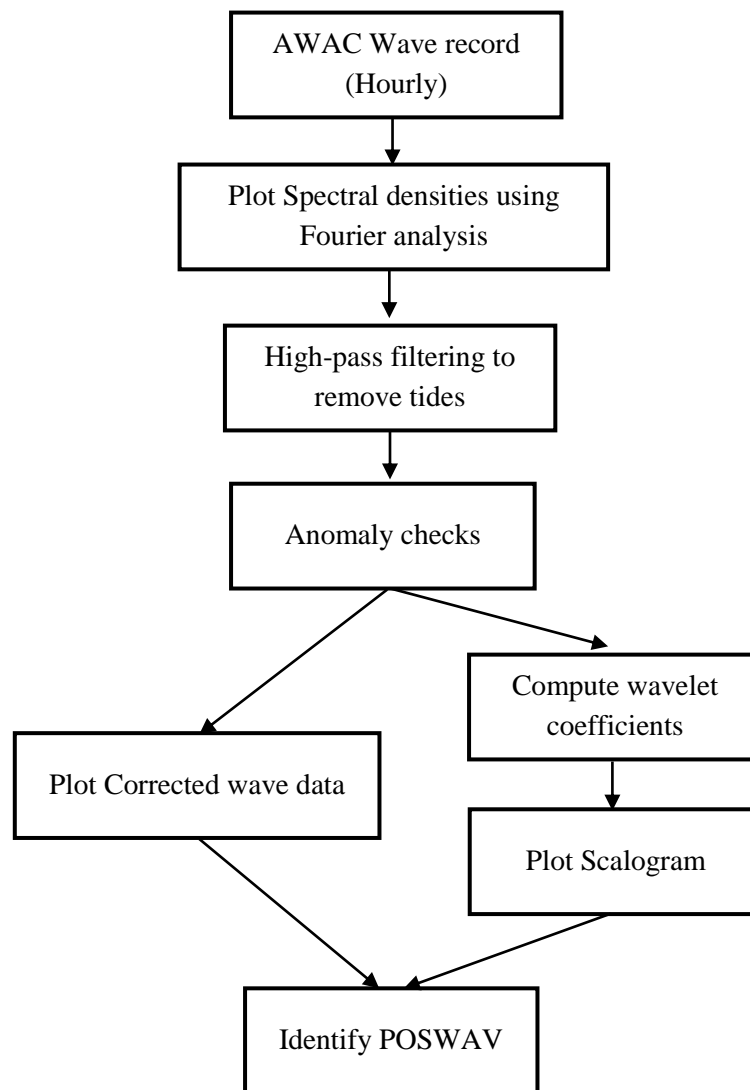


Figure 43: Flow diagram for wave processing

Spectral Analysis

Fast Fourier Transform (FFT) was used to first decompose the wave signal into various Fourier coefficients represented on a spectral density plot, as shown by Figure 44a. The magnitude of the spectral density, S , indicates the total amount of wave energy present within a particular frequency, f . As previously discussed, the non-stationary nature of vessel-generated wakes makes it inappropriate to separate wind and vessel waves by means of applying a band-pass filter. Since they occupy similar frequency bands, it is impossible to eliminate one without removing portions of the other. Nevertheless, a high pass filter can still be applied to remove the lower frequency tidal fluctuations present within the data. A high pass filter of $f_p = 0.2\text{s}$ was used in this study. Figures 44~45 illustrate the effects of the filtering process.

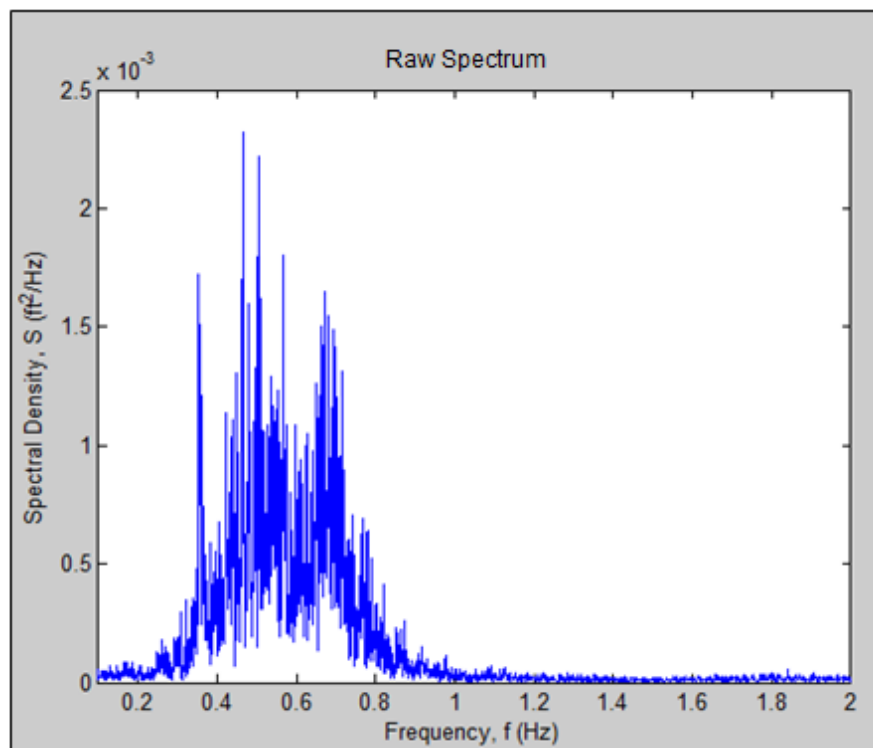


Figure 44a: Raw Wave Spectrum

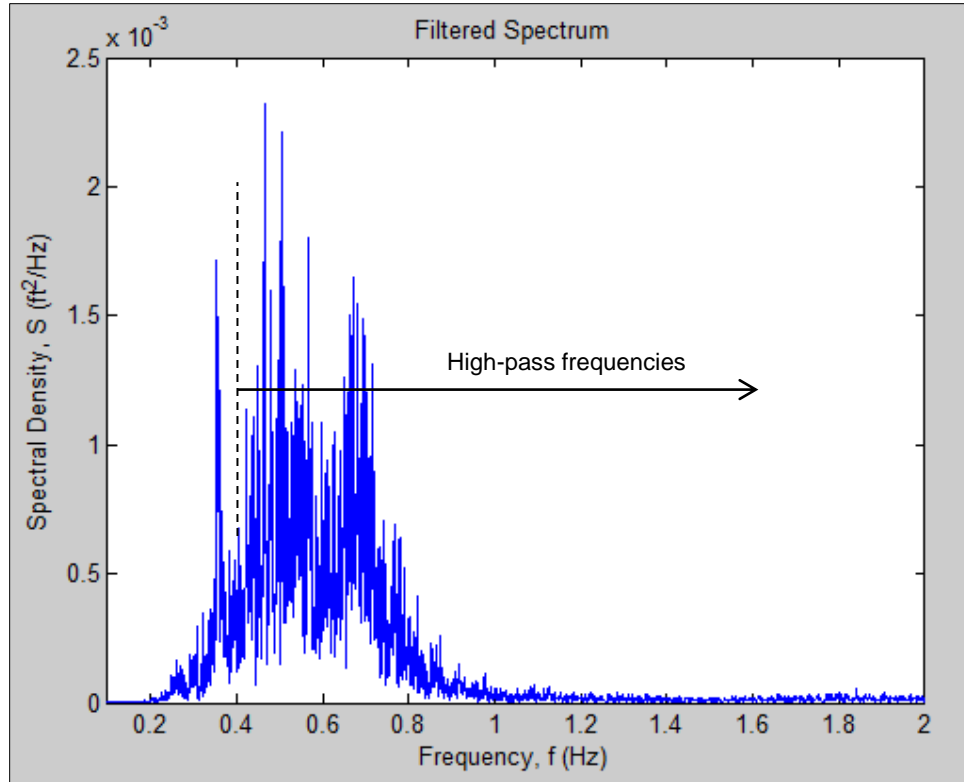


Figure 44b: Filtered Spectrum (Low tidal frequencies removed)

The AWAC data was observed to contain several ‘anomalous bursts’ as indicated in Figure 45a. These bursts are characterized by a sudden increase ($>1.0\text{m}$) in the wave displacement (typically affecting 1 to 2 data points), which were unlikely since vessel wakes arrive as a wave train with gradually increasing amplitudes. This can be attributed to instrumental error. The AWAC measures water elevation by projecting acoustic beams towards the surface. Despite having a small beam angle (1.7° opening angle), the beam develops a beam width of approximately 0.15m when it reaches the water surface (assuming 5.0m deployment depth).

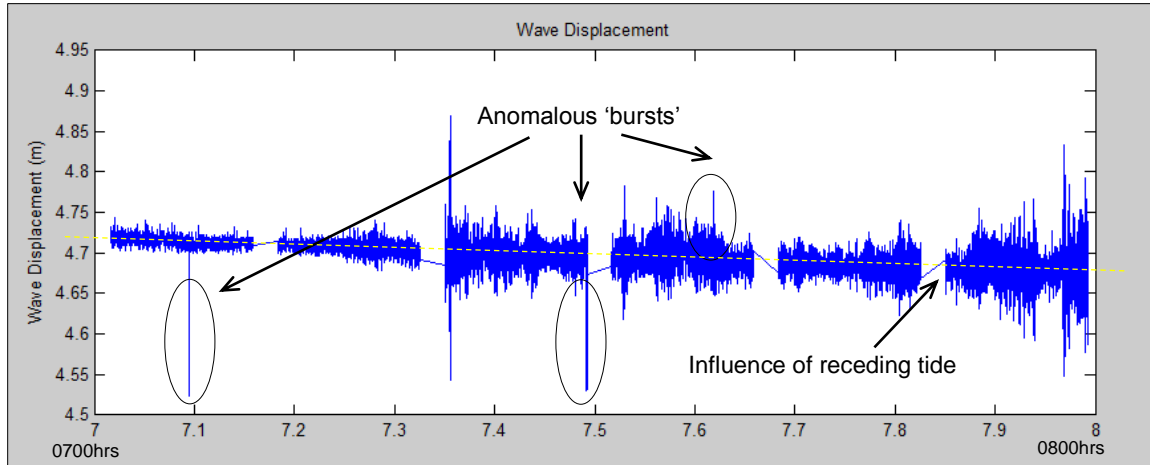


Figure 45a: Raw Wave Data

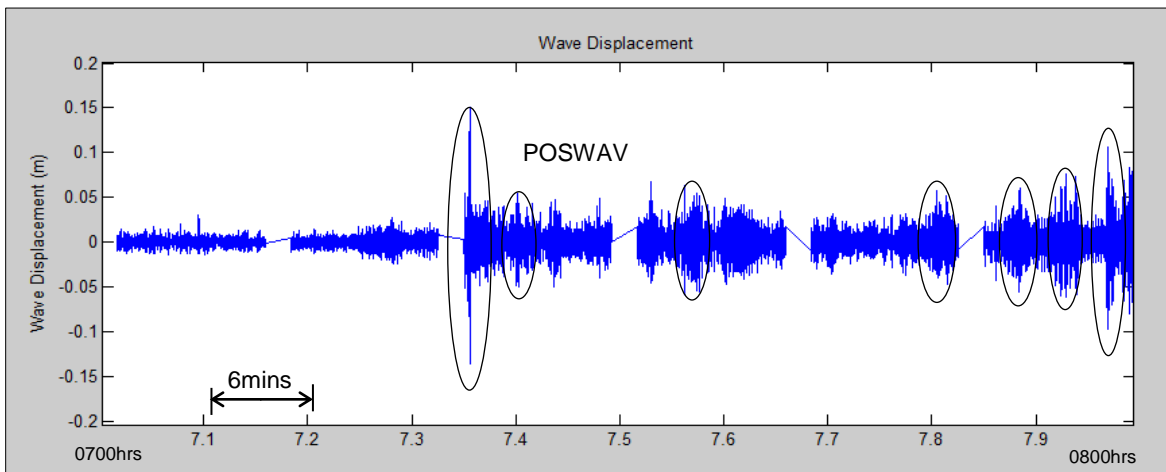


Figure 45b: Corrected Wave Data

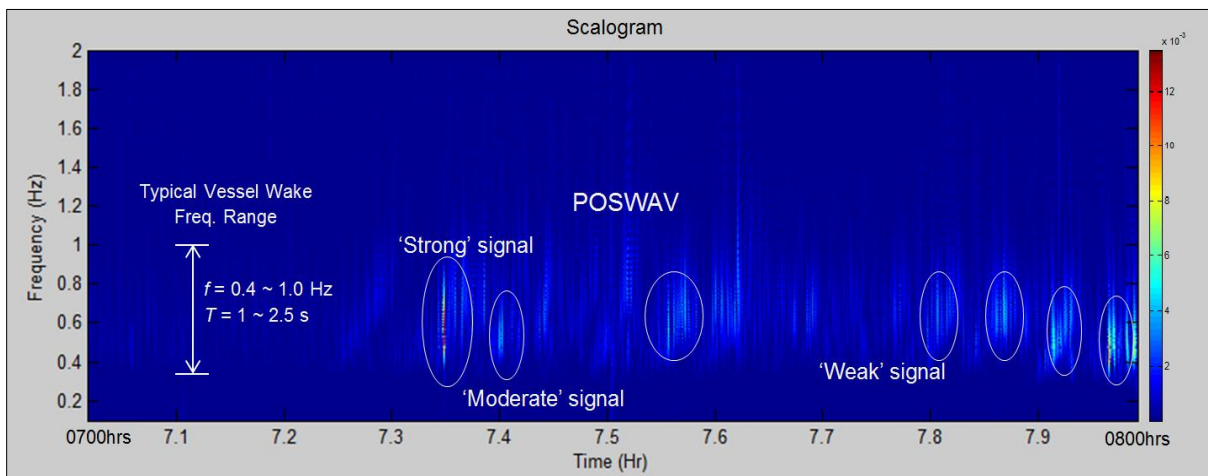


Figure 45c: Wave Scalogram

The anomalous burst can possibly be attributed to waves breaking within this small projection area, preventing the vertical ‘ping’ from being reflected back to the transducer, as illustrated in Figure 46. Corrections were thus included to eliminate these isolated anomalies by artificially inserting a padding value of ‘0’ to wave displacement data points when the difference in wave displacement between a preceding and its following point exceeds 0.5m. Wavelet analysis was then performed on the corrected wave data to produce a wave spectrum scalogram (Figure 45c).

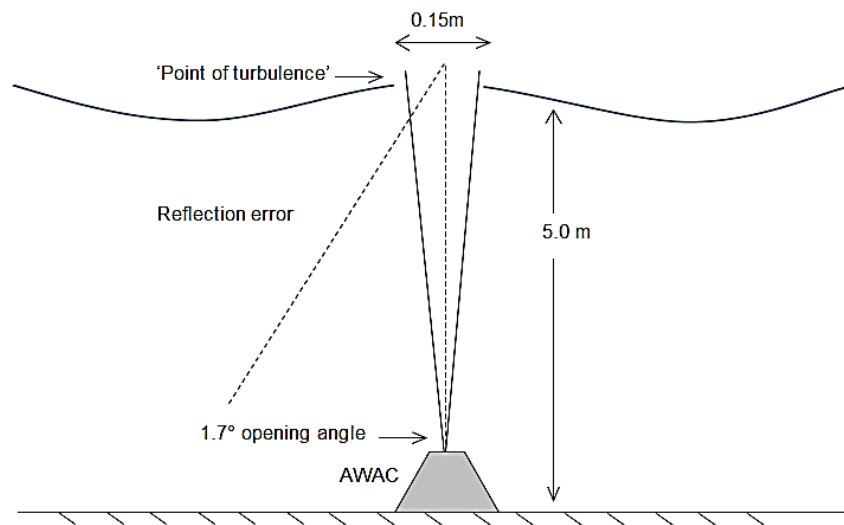


Figure 46: Anomalous bursts caused by beam reflection error

Vessel-Wave Identification

Time is required for a vessel-generated wave to travel from its point of origin to the wave gage. This distance travelled is represented by the vessel’s sailing distance from the seawall, y that was obtained during video processing. As such, there is a time delay between the time of vessel detection and the time when its wake arrives at the wave gage. To estimate the time of

arrival, we use the knowledge of the vessel's speed V_s , distance y , and an angle of propagation estimate θ . Figure 47 illustrates the geometry behind this relationship.

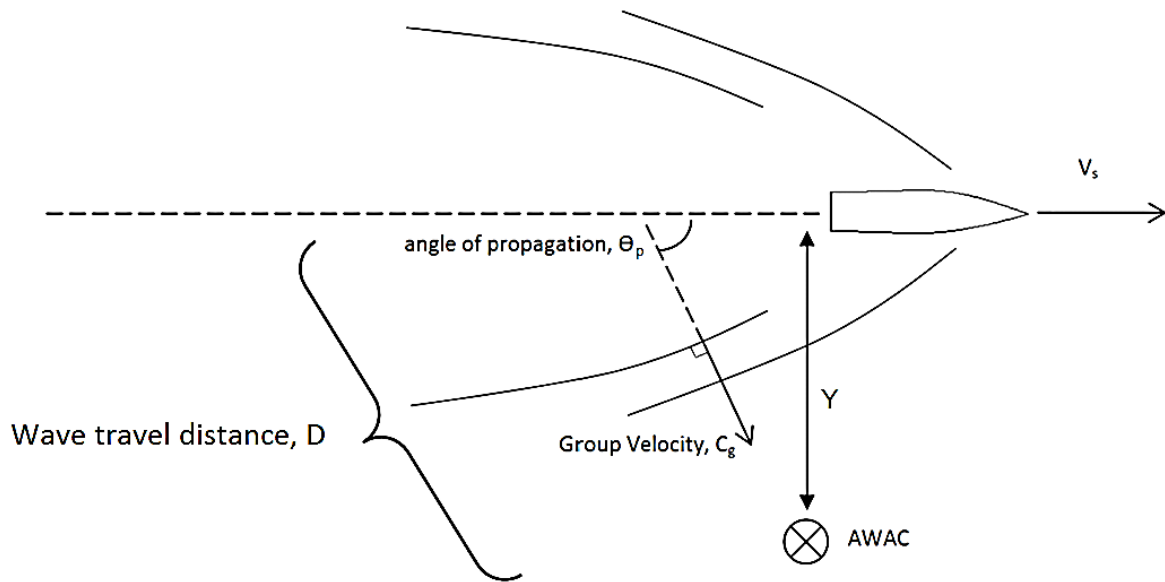


Figure 47: Geometry of vessel wave propagation

Angle θ_p is usually dependent on the depth Froude number. To obtain arrival time estimation, a simplified analysis of vessel wave propagation will be used with the θ_p value assumed to be at a constant of 35.27° . Wave celerity C is assumed to be a function of vessel speed and is used to estimate a group propagation velocity, C_g using the following relationship:

$$C_g = \frac{C}{2} = \frac{V_s \cos \theta}{2} \quad (19)$$

Using C_g , the time taken for the vessel wave to travel across distance y was found using Eqn. 20. This time delay, Δt , was then factored into the time of vessel detection to estimate the time of wave arrival at the wave gage.

$$\Delta t = \frac{D}{cg} = \left(\frac{y}{\sin \theta} \right) * \left(\frac{2}{V_s \cos \theta} \right) = \frac{(2dy)}{V_s \sin(35.27^\circ) \cos(35.27^\circ)} = 4.25 \left(\frac{dy}{V_s} \right) \quad (20)$$

In addition to estimating wave arrival time, wavelet scalograms were also used to aid the identification of possible vessel-wake events (POSWAV) by revealing regions where time-frequency shifts occur. The color scale indicates the strength of the returns which correlates with the likelihood that the wave is a transient, localized vessel-generated wave. As expected, the spatially homogenous wind-waves correlate with weak time-frequency shifts, creating a background from which the vessel-wake events can be identified. Figure 48 shows an example of determining maximum wave height, H_{\max} with the aid of the corresponding scalogram.

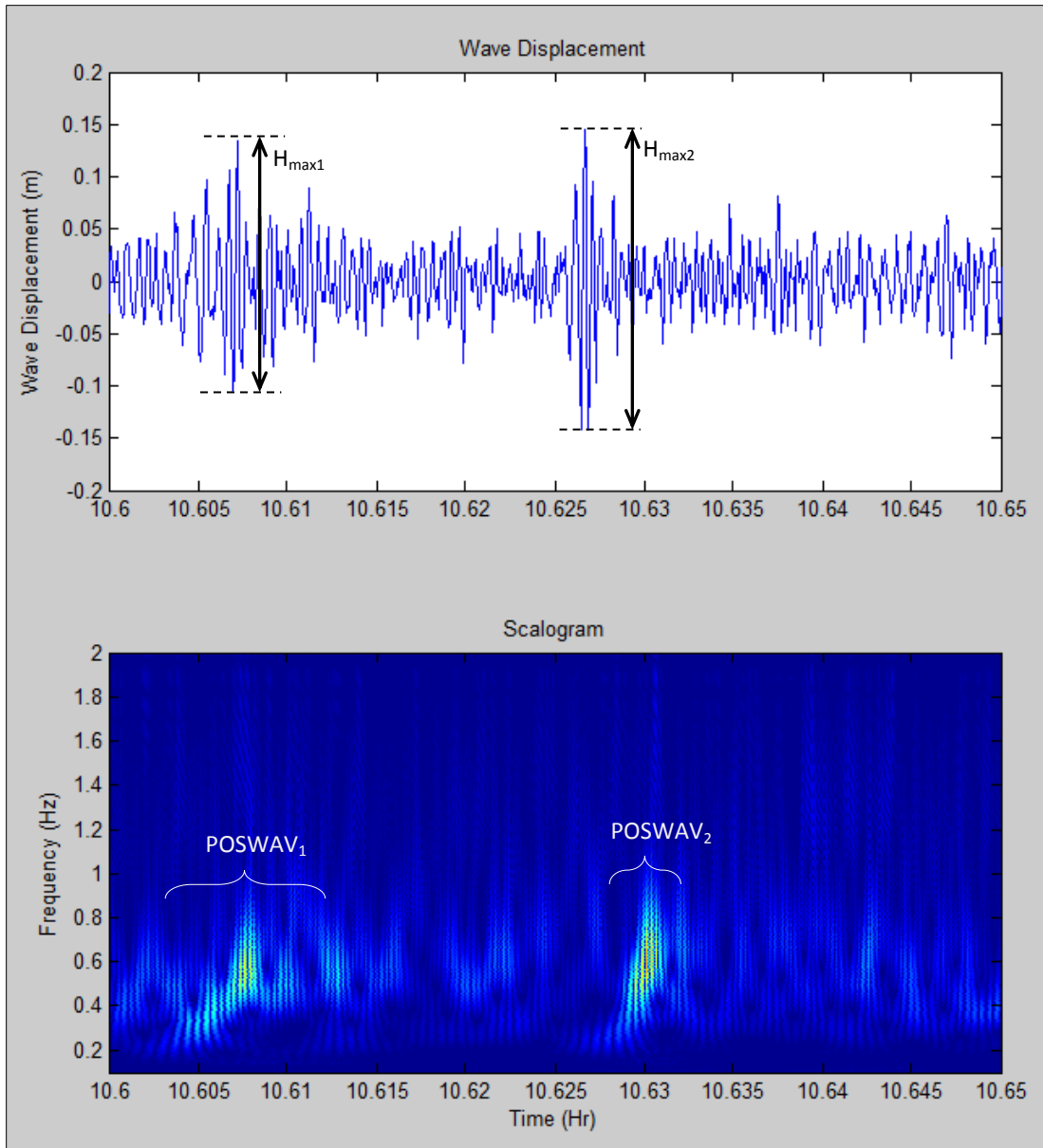


Figure 48: Determining H_{\max} with the aid of wavelet scalogram

CHAPTER 6 – RESULTS

6.1 Model Development

The dataset obtained from video processing and wave height records was analyzed to develop a new empirical formula that seeks to provide a more general description for the vessel-wake relationships derived by past studies. In total, 471 data points were generated for analysis from field data collection. Figure 49 shows a breakdown of the general vessel sizes tracked.

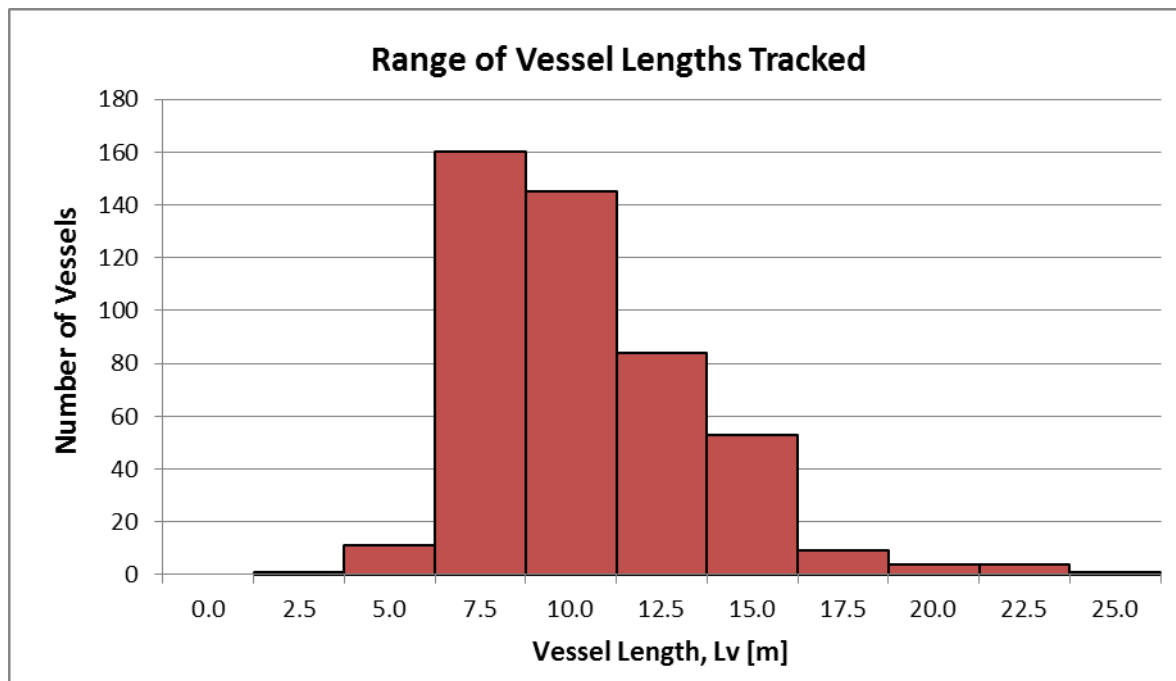


Figure 49: Range of Vessel lengths tracked

In the development of a new equation model, dimensional values obtained from our data set were first normalized. Assuming a deep water relationship, the amplitudes of vessel-generated waves vary as a function of the length based Froude number F_L . Based on physical arguments, the amplitude of the bow wave for a moving ship should scale according to the

velocity head, given by $\frac{v^2}{2g}$. Kriebel and Seelig suggest that the wave can therefore be normalized in the form of $\frac{gH}{v^2}$. The distance of wave measurement relative to the sailing line of the vessel, y , can also be normalized in the form of $\left(\frac{y}{L}\right)^{-1/3}$ as suggested in their study.

Knowing that wave amplitude decreases exponentially as it travels further away from the sailing line (dispersion relation), we apply the $\left(\frac{y}{L}\right)^{-1/3}$ factor to normalize wave height values obtained at a distance y for comparison at $y/L=1$. An empirical relationship of wave height H and F_L could then be established in the form of Eqn. 21 below. Figure 50 illustrates the relationship of correcting the measured wave height, H_{\max} , to H_1 from different y/L values.

$$\frac{gH_1}{v^2} = \frac{gH_m}{v^2} \left(\frac{y}{L}\right)^{1/3} \quad (21)$$

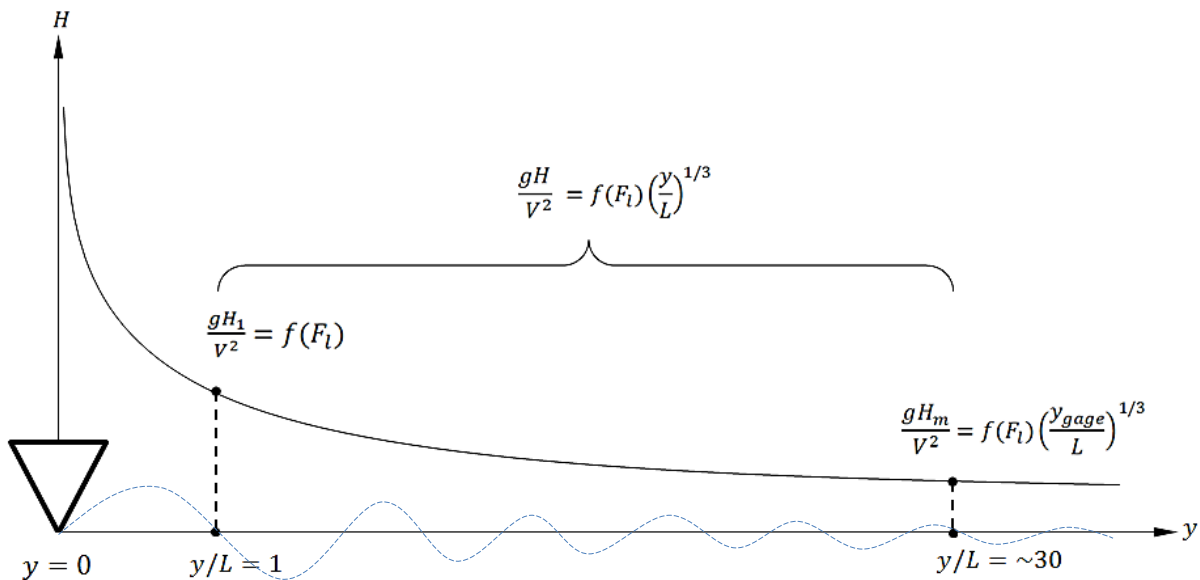


Figure 50: Normalizing wave heights at different (y/L) values,

where f is a function of length Froude number F_L

The following plots demonstrate the effect of correcting the measured wave height, H_{\max} to the standardized distance of $y/L=1$, H_1 , for the two control vessels. Wave height was plotted against vessel speeds to illustrate this relationship. Additionally, the dataset from the Robalo and the Zodiac follow the expected trend as proposed by Maynard (2005), as shown in Figure 52 and 54.

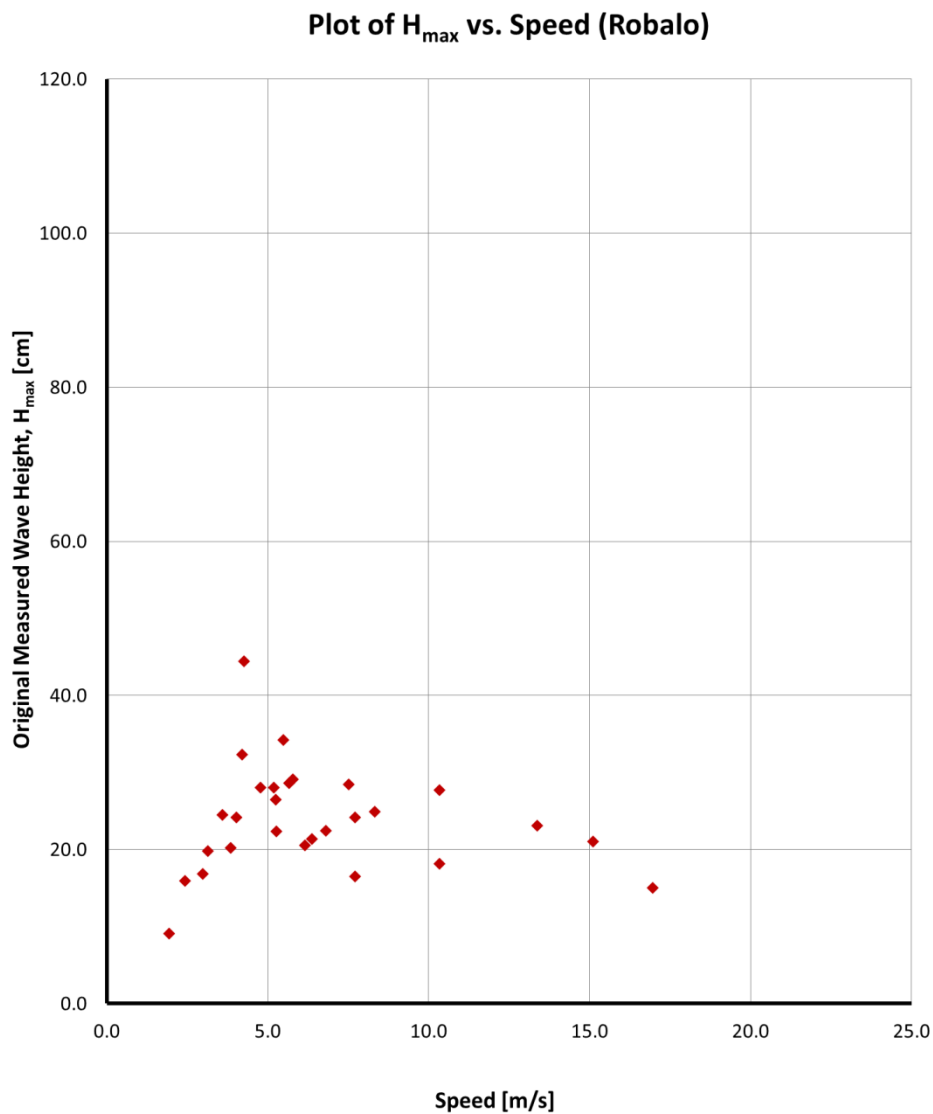


Figure 51: Original H_{\max} vs. Vessel Speed for Robalo dataset

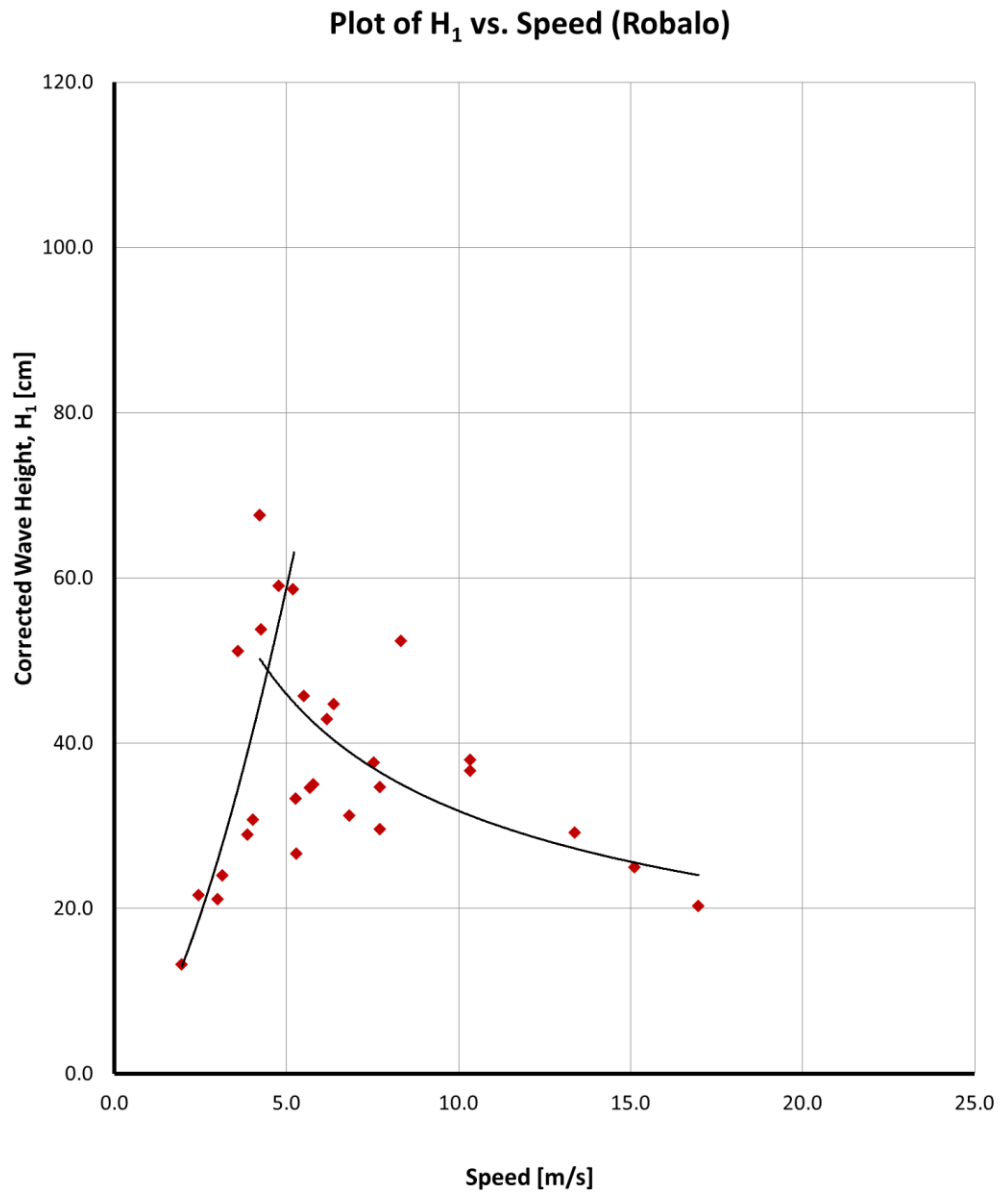


Figure 52: Corrected H_1 vs. Vessel Speed for Robalo dataset

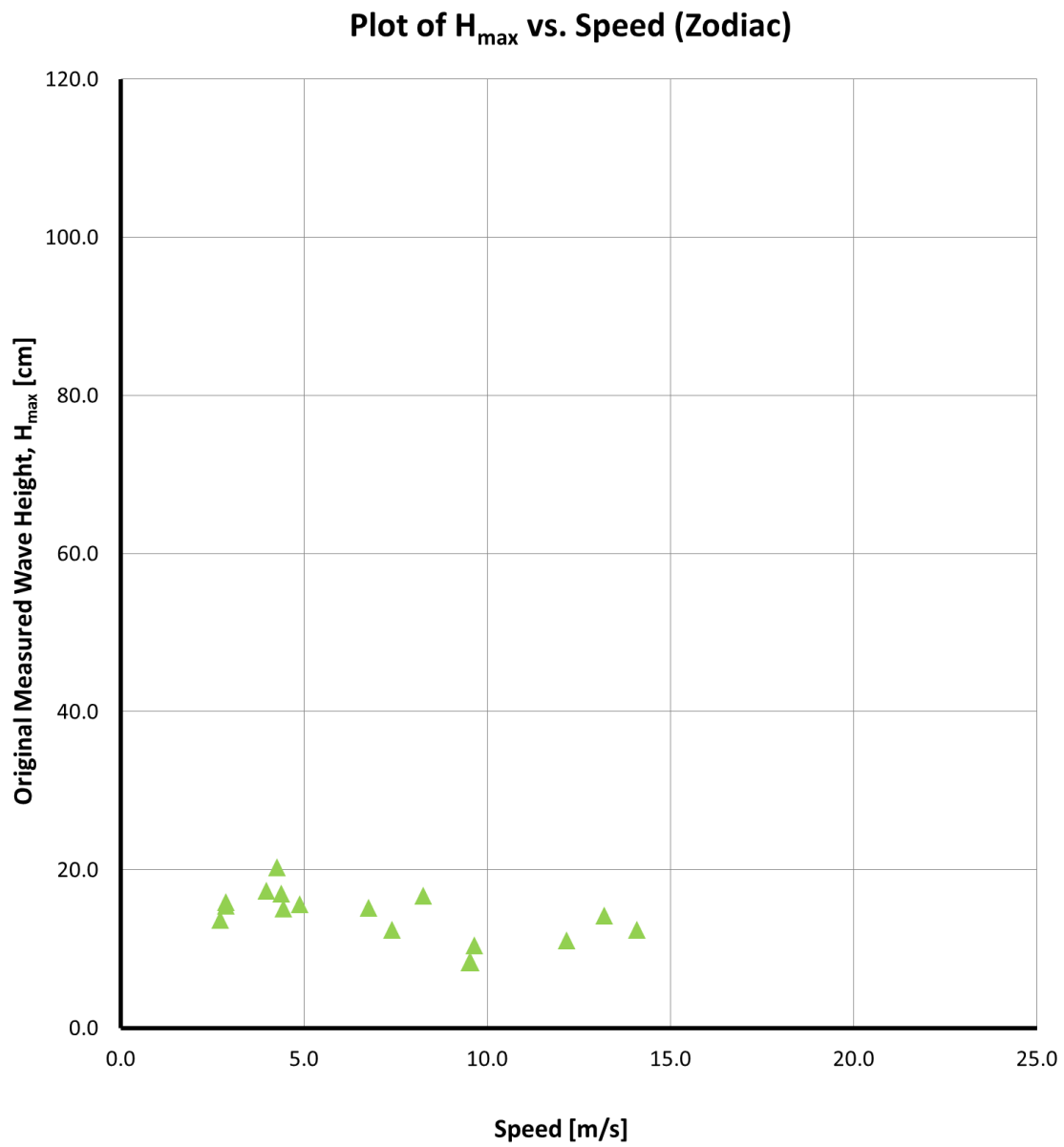


Figure 53: Original H_{\max} vs. Vessel Speed for Zodiac dataset

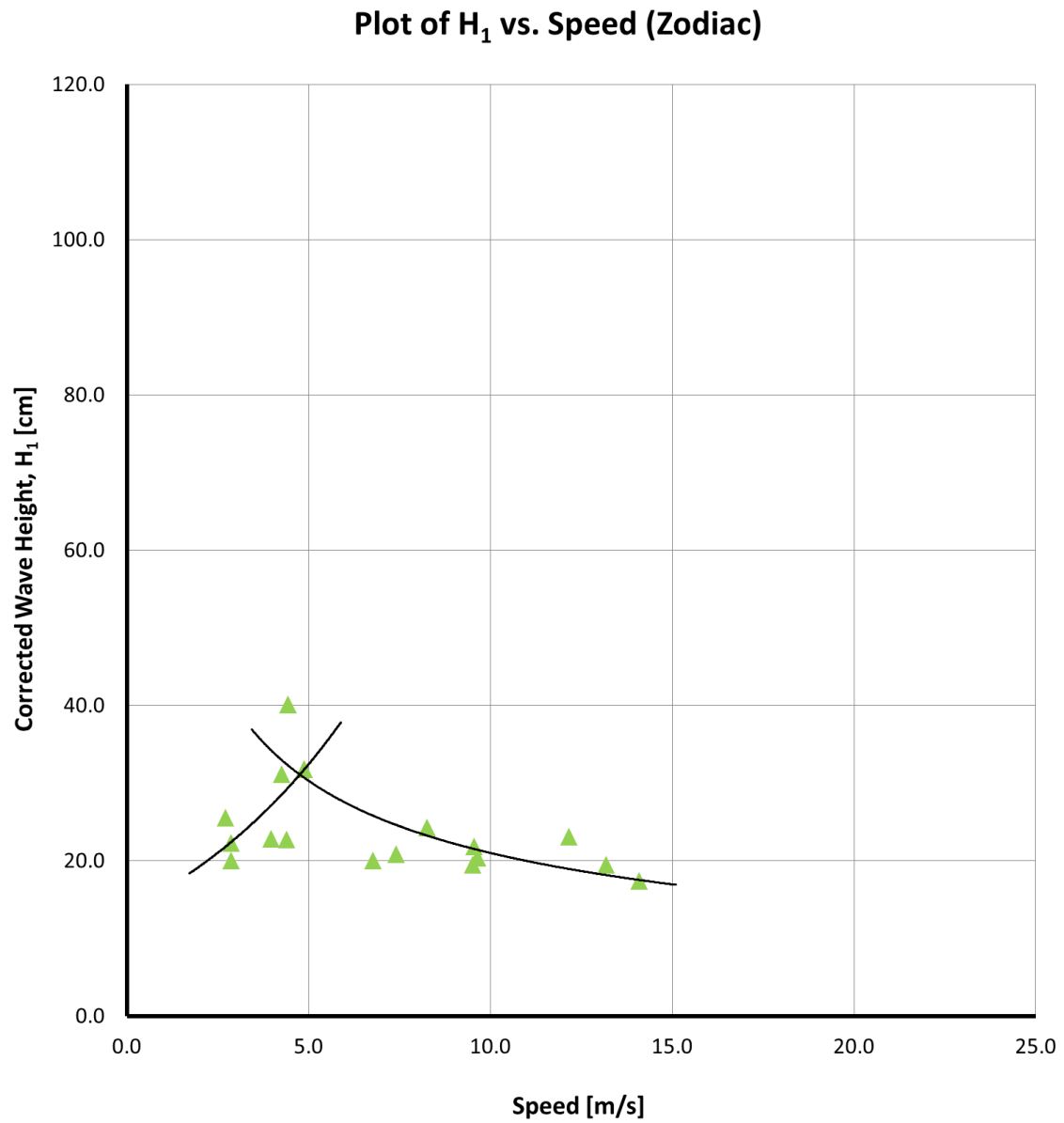


Figure 54: Corrected H_1 vs. Vessel Speed for Zodiac dataset

However, the trend observed in the Robalo and Zodiac datasets were quickly lost when all 471 data points were included (Figure 55). To better illustrate the relationship between H_{\max} and boat parameters, we will plot the normalized wave height gH/V^2 against the vessel's Froude number. In this study, both F_L and F_V were used to evaluate the data.

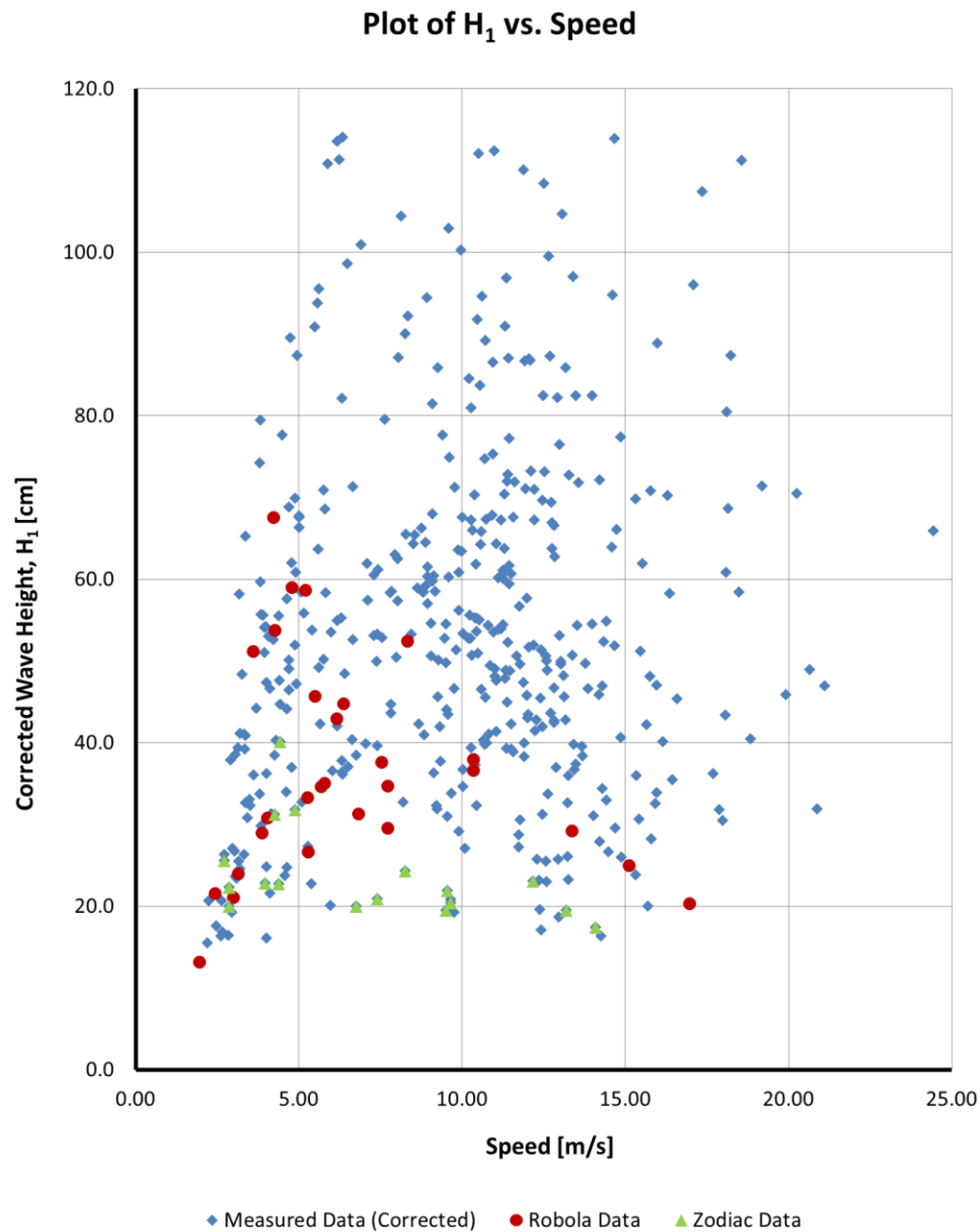


Figure 55: Corrected H_1 vs. Vessel Speed for the entire dataset

In Maynard (2005), an alternative method of normalizing the distance from the sailing line using the variable $\nabla^{1/3}$ (cube root of displacement) instead of vessel length L_V was proposed. His equation adjusts the maximum wave height measured at distance y to H_0 at the sailing line ($y=0$) by using a $\left(\frac{y}{\nabla^{1/3}}\right)^{-0.42}$ relationship. However, since the variable $\nabla^{1/3}$ was not measured in our study, a conversion equation was introduced to find $\nabla^{1/3}$ given vessel length L . Three different classes of powerboats (a total of 26 individual vessels) with commercially available specifications such as length and displacement were studied. Specifications of the individual vessels can be found in Appendix A.

A comparison of $\nabla^{1/3}$ and L values show that parameter $\nabla^{1/3}$ adopts a linear relationship with increasing L_V . Figure 54 shows the linear relationship between $\nabla^{1/3}$ and L . The averaged conversion factor of $\nabla^{1/3} = 0.1748L$ was found and subsequently used to calculate F_∇ .

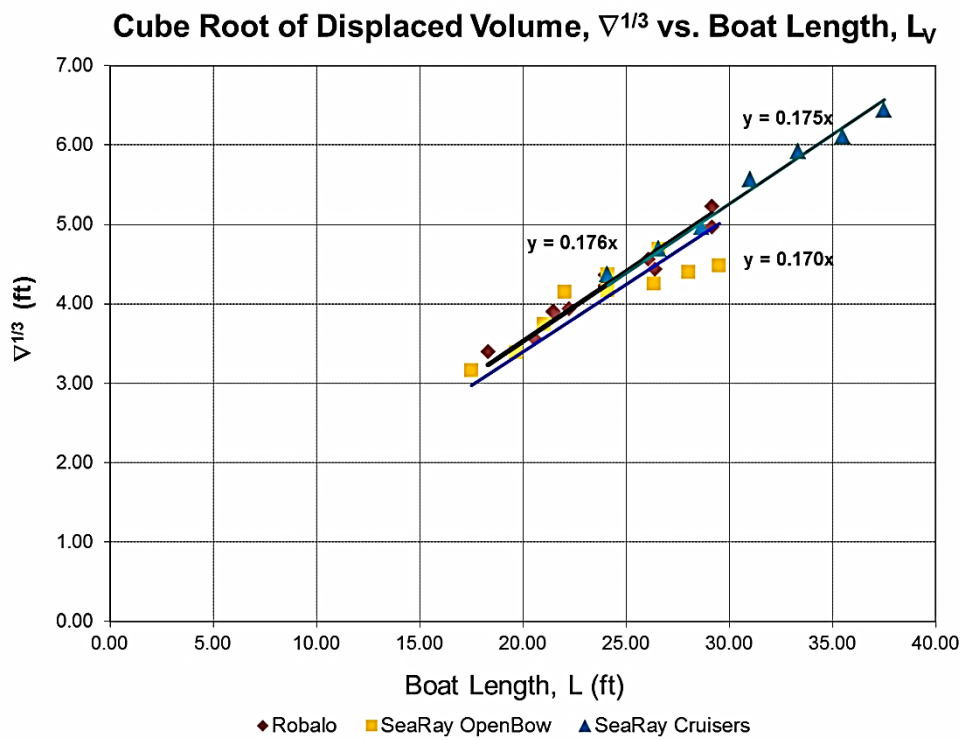


Figure 56: Comparing the relationship between $\nabla^{1/3}$ and L_V

6.2 Experimental Data Analysis

The resultant data plot of normalized wave height vs. Froude number peaked at approximately $F_V = 1.00$ and $F_L = 0.4$ as expected by theory. As shown by Figure 55 and 56, both plots using the two Froude numbers exhibited similar trends, with the only difference being the value of the asymptote. Both the Robalo and Zodiac datasets were included in the plots as well, and both of these data followed the general trend of the entire measured dataset. The family of regression equations fitted through the data points exhibited similar R^2 values, ranging from 0.794 – 0.803.

Since both Froude numbers exhibited the similar properties when applied to our dataset, the volume Froude number, F_V was eventually selected since it works better for vessels in the semi-planing and planing mode (For F_V values ranging from 1.0 – 3.0 as per Table 1). The effectiveness of these regression equations was then evaluated by plotting the measured wave heights vs. the wave heights predicted using the following three proposed equations obtained using the F_V dataset from Figure 57:

Power Form ($R^2=0.799$)

$$gH_1/v^2 = 0.489 * (F_V)^{-2.389} \quad (22)$$

Exponential Form ($R^2=0.777$)

$$gH_1/v^2 = 0.405e^{-(0.722 * F_V)} \quad (23)$$

Hyperbolic Tangent Form ($R^2=0.760$)

$$gH_1/v^2 = 1 - \tanh^{0.265}(0.38 * F_V) \quad (24)$$

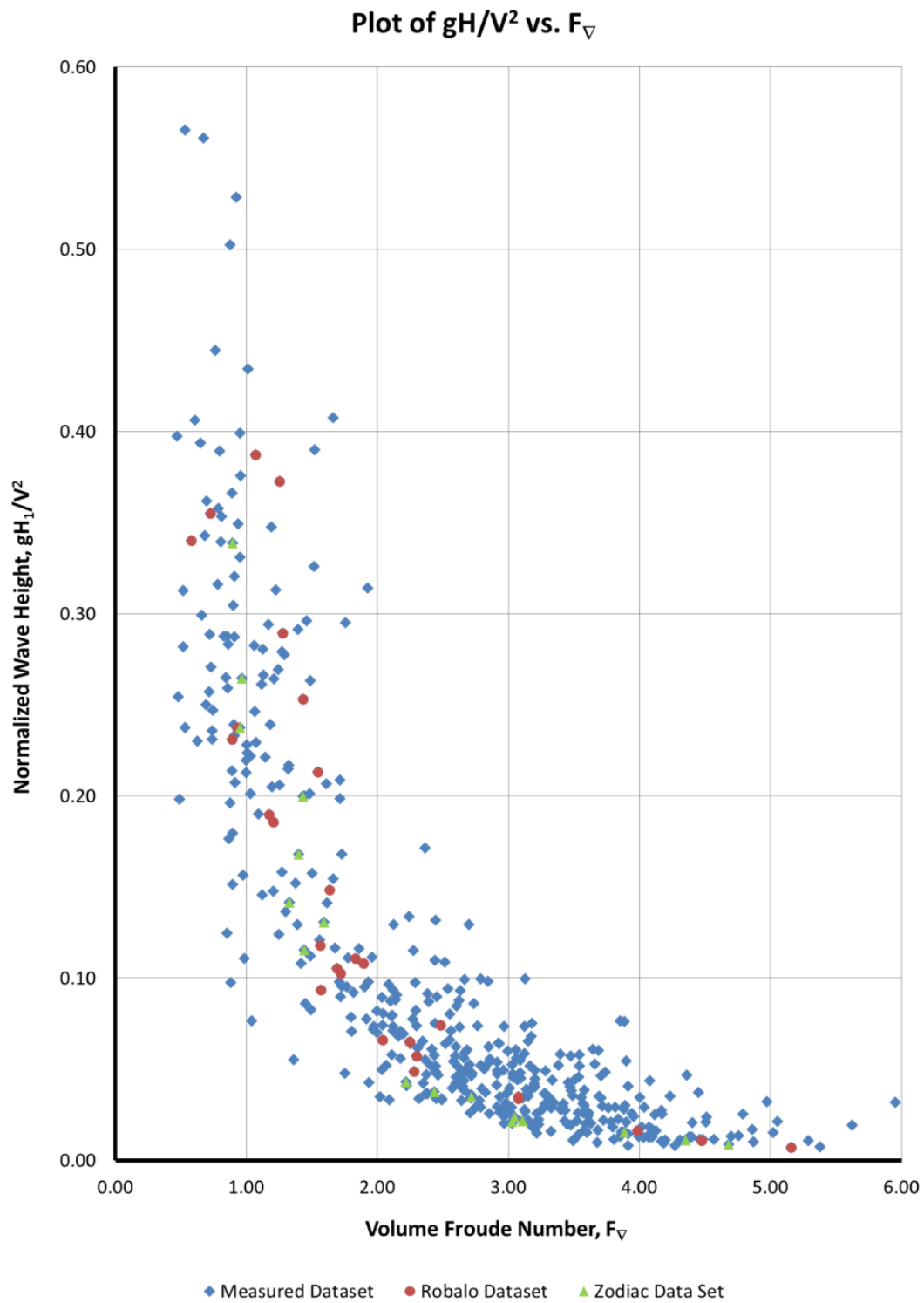


Figure 57: Normalized Wave Height vs. F_V plot

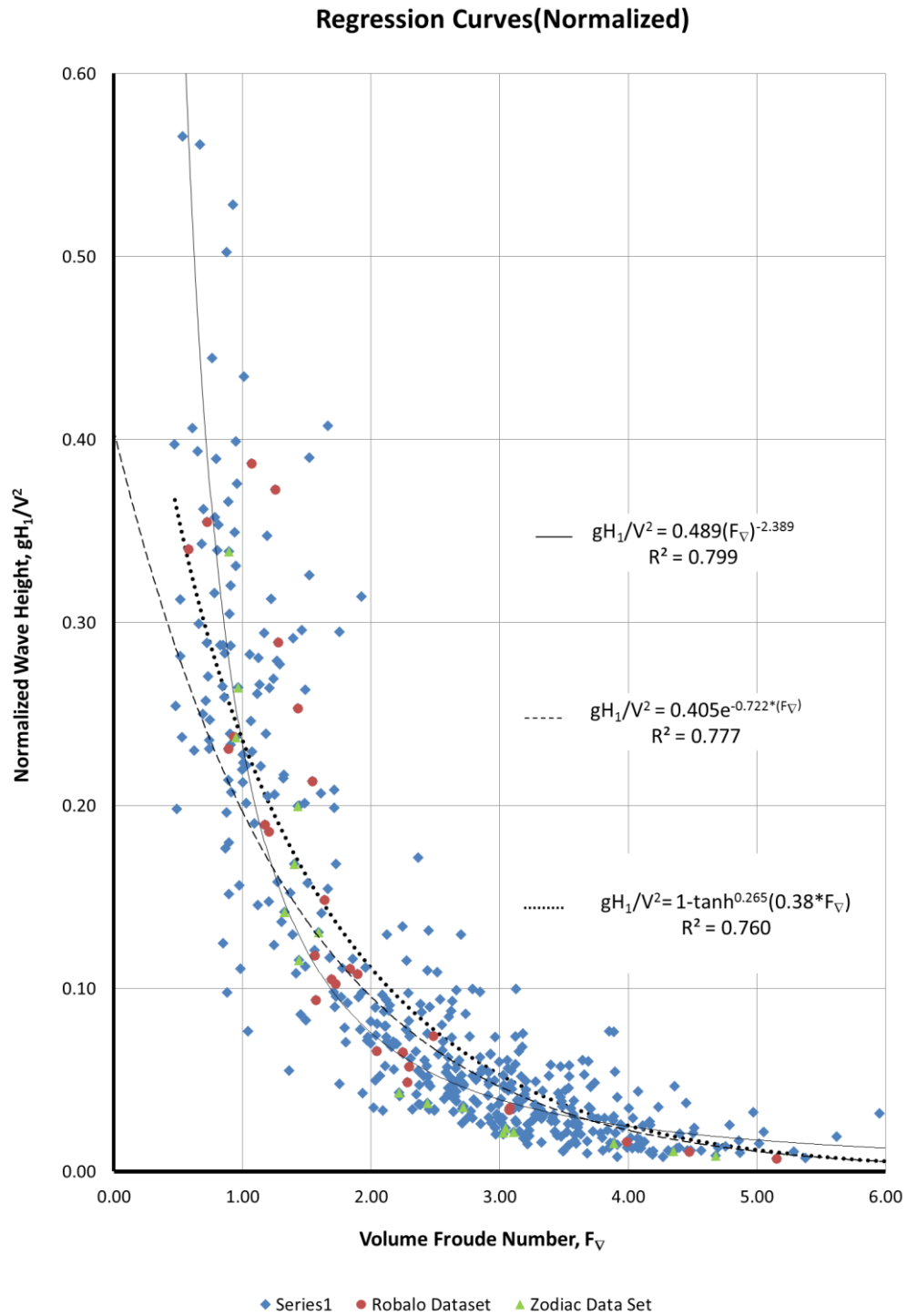


Figure 58: Plot of Dataset with Regression Curves

As deduced from the R^2 values, all three equation forms were equally effective at predicting the measured wave heights. A closer comparison by plotting the measured gH/V^2 vs. the predicted gH/V^2 (Figure 59) shows that there is a closer correlation between the measured values and the regression values at lower magnitudes of gH/V^2 . Above $gH/V^2 > 0.2$, the power form seems to be significantly overestimating the wave heights, while the exponential form seems to be slightly underestimating it. The hyperbolic tangent seems to be the most appropriate at predicting gH/V^2 at these higher ranges of gH/V^2 .

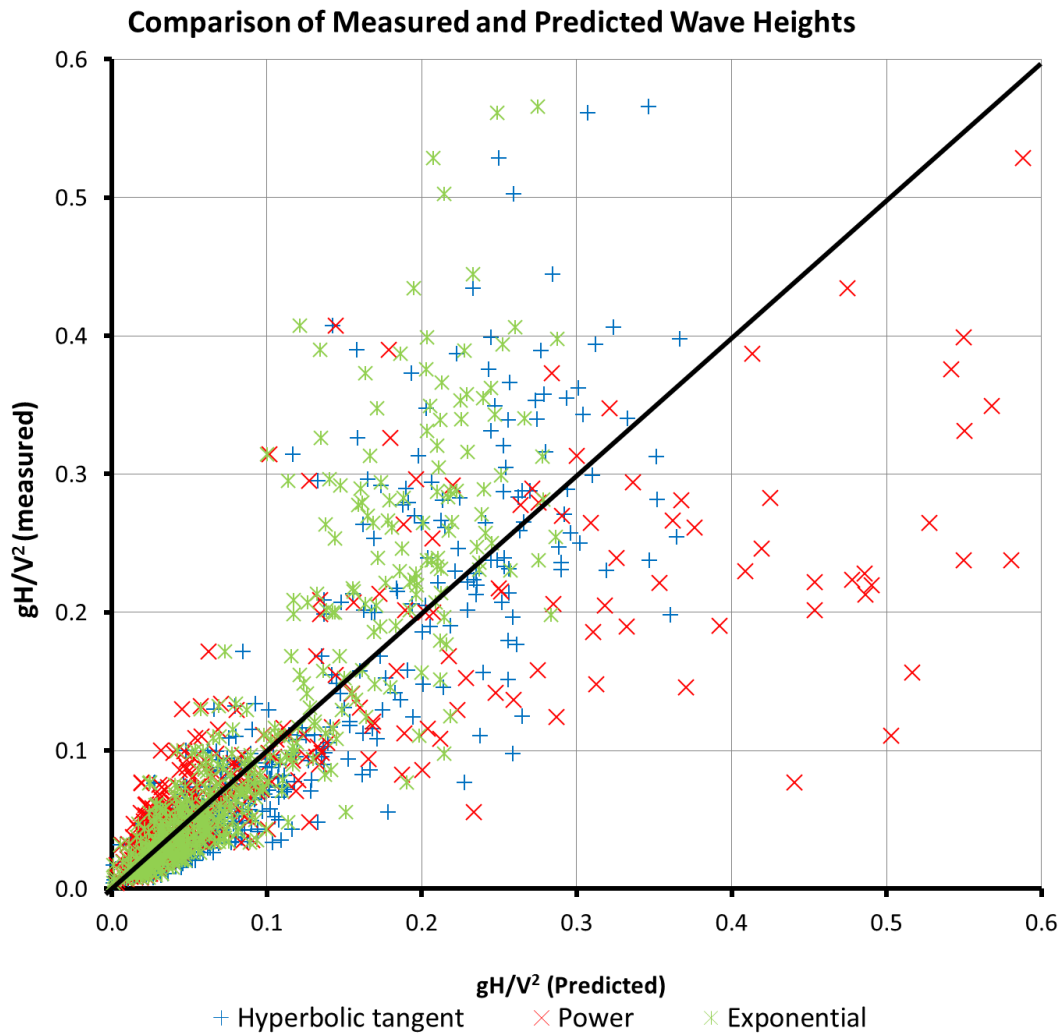


Figure 59: Comparison of gH/V^2 measured from the AWAC and gH/V^2 predicted from the three regression equation forms

To further compare the effectiveness of the three regression equations, predicted values of wave heights were found for the two control vessels, and these data points were then compared with the measured values shown earlier in Figures 51 - 54. Figure 60 and 61 shows the resultant plot for the Robalo and the Zodiac respectively. As shown in these plots, both the exponential and hyperbolic tangent curves seem to predict the expected trend sufficiently well. The hyperbolic tangent seems to produce the best prediction at lower speeds. The peak of the curves, however, was translated slightly to the right (at higher speed values) as compared to the actual values measured. Additionally, the power regression equation was found to be limited in its ability to predict maximum wave heights in the dimensional form as it only reproduces the expected trend at higher Froude numbers (beyond the critical value), despite having the highest R^2 value among the three equations. The power regression curve was therefore not utilized for further analysis.

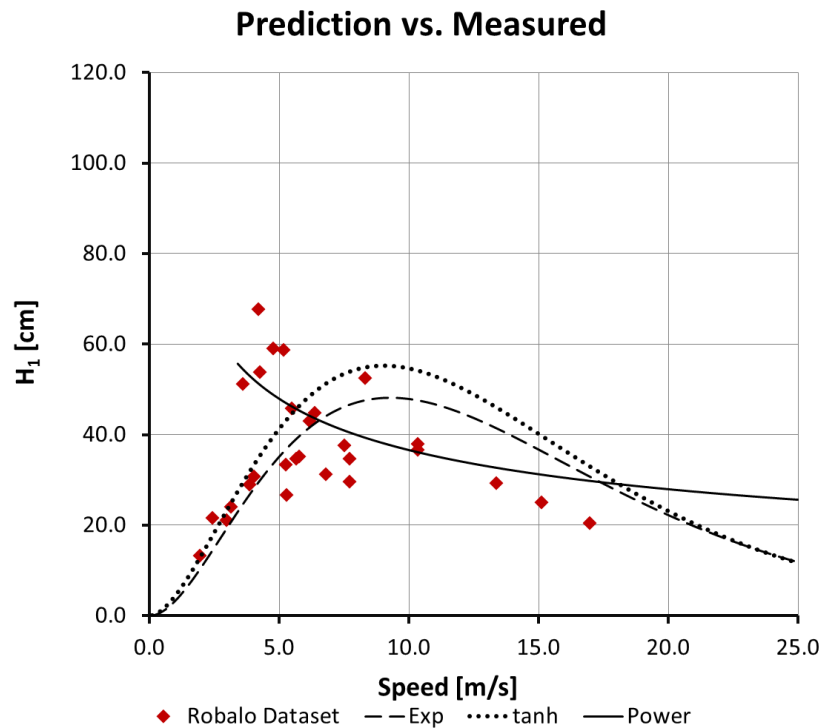


Figure 60: Comparison of Predicted vs. Measured wave heights for Robalo

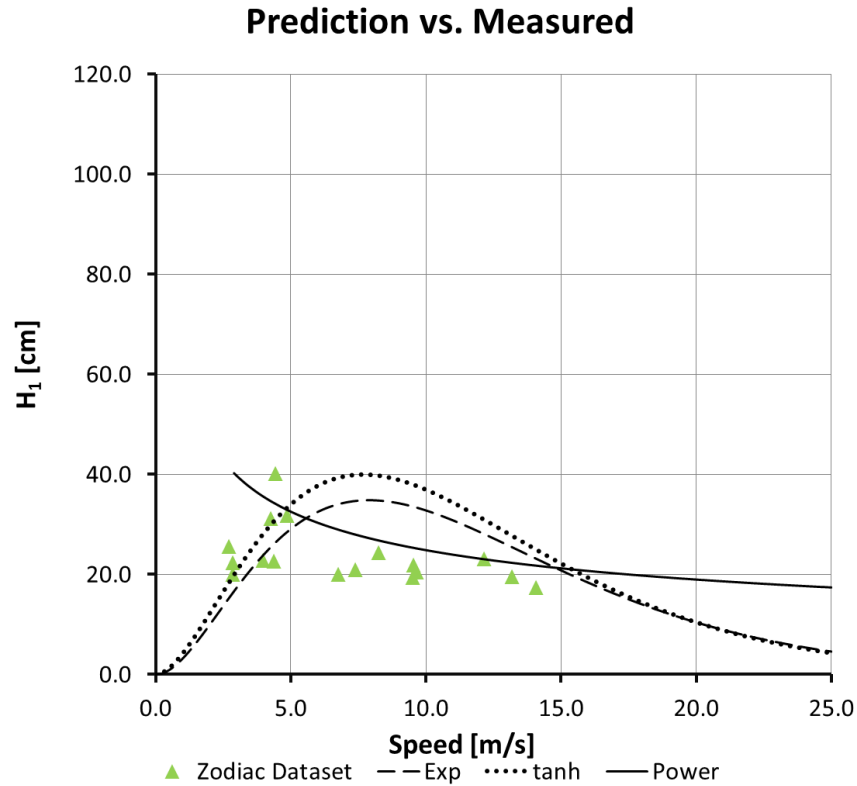


Figure 61: Comparison of Predicted vs. Measured wave heights for Zodiac

For further analysis, data points were grouped by their vessel lengths into different bins to evaluate any effects of vessel lengths on the prediction equations. By theory, the effect of varying vessel lengths should have been eliminated when the $\left(\frac{y}{L}\right)^{-1/3}$ factor was applied to normalize the distance of the vessel away from the sailing line. Figure 62 shows a plot of gH/V^2 vs. Froude number, similar to Figures 57 and 58 albeit with the different vessel length groups labeled. The effect of varying vessel lengths was further accentuated when the data points were plotted on a logarithmic scale as shown in Figure 63.

In the following Figures 64-68, measured wave heights were plotted against the prediction equations for the mean vessel length of that length group. For example, in Figure 64, measured data points of the “ $2.5 < L < 5.0\text{m}$ ” bin were plotted against the predicted wave heights found by applying the mean vessel length of the vessels within that group (4.36m) to the exponential and hyperbolic tangent prediction equation, Equations (23) and (24). While the measured data points do seem to clutter around the peaks of the prediction equation, the amount of scatter is too significant to draw any useful conclusions.

The scatter observed in our dataset can be attributed to other factors such as the vessel’s hull form that influences the size of the vessel’s wake in other ways. However, due to the limitations of our tracking tool, such parameters were not recorded during the course of this study. Further refinement of the tracking tool to include the ability to measure a vessel’s bow angle will allow such relationships to be studied.

gH/V^2 vs. F_{∇} Plot

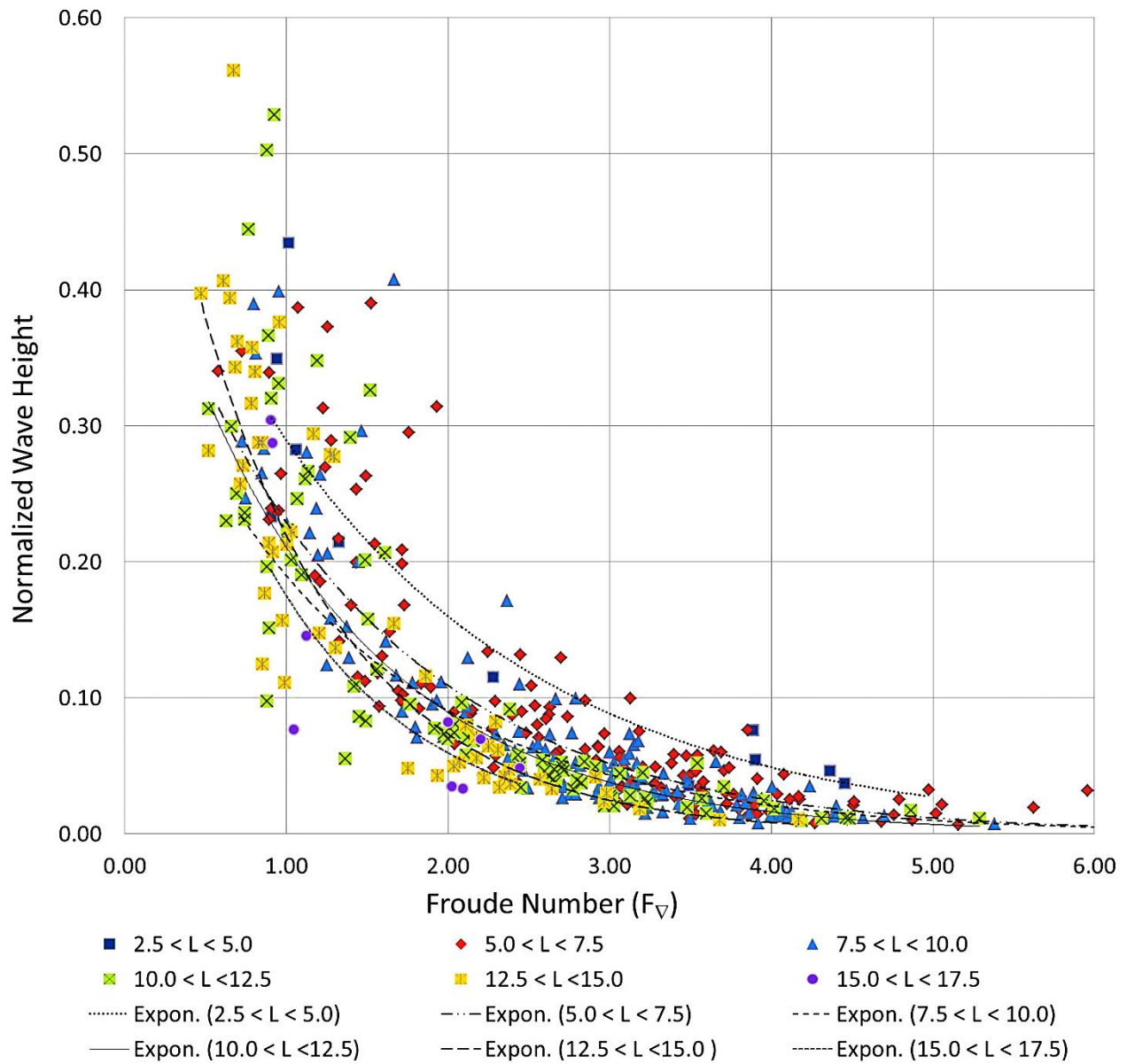


Figure 62: Normalized Wave Height gH_1/V^2 vs. F_{∇} plot differentiated by length

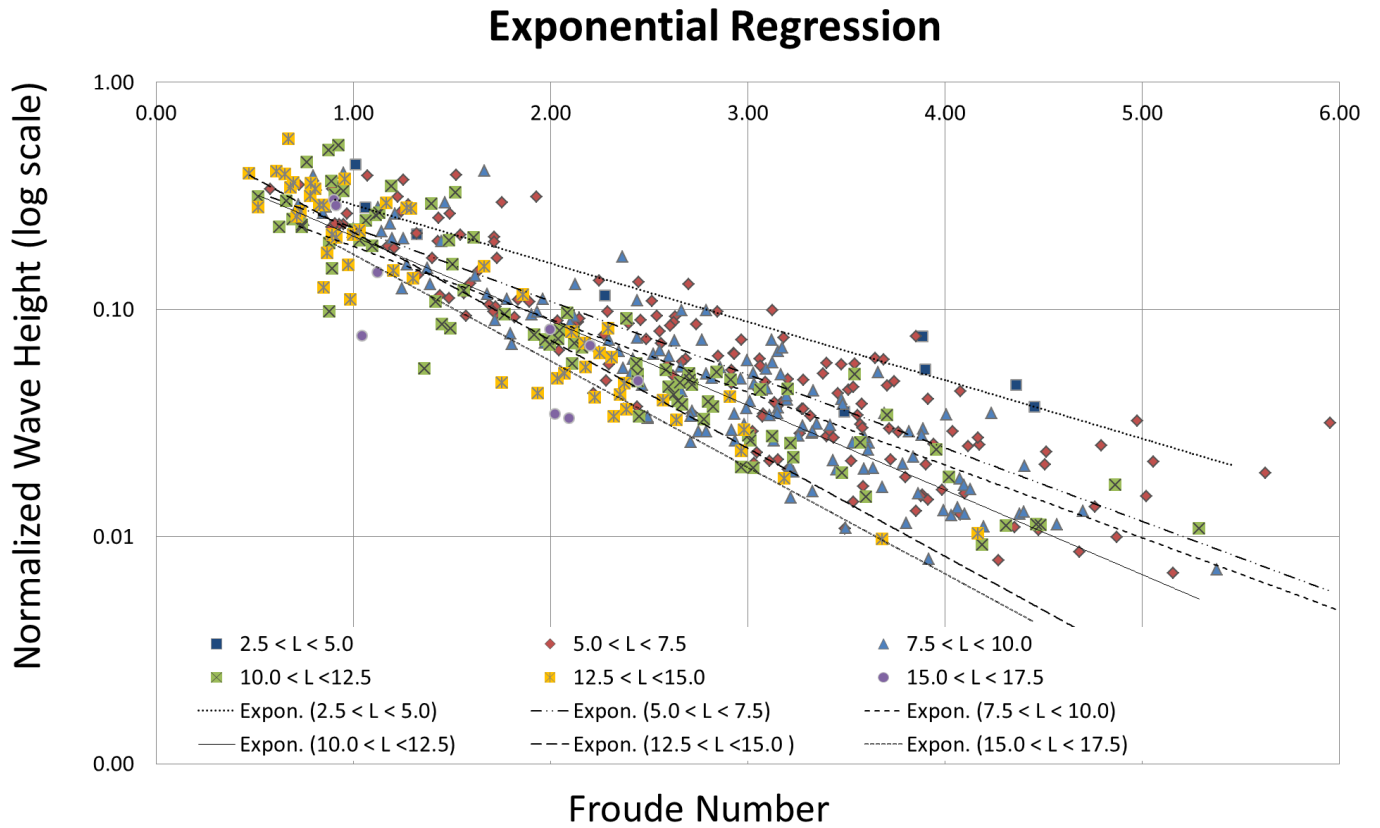


Figure 63: Normalized Wave Height vs. F_v plot (log scale)

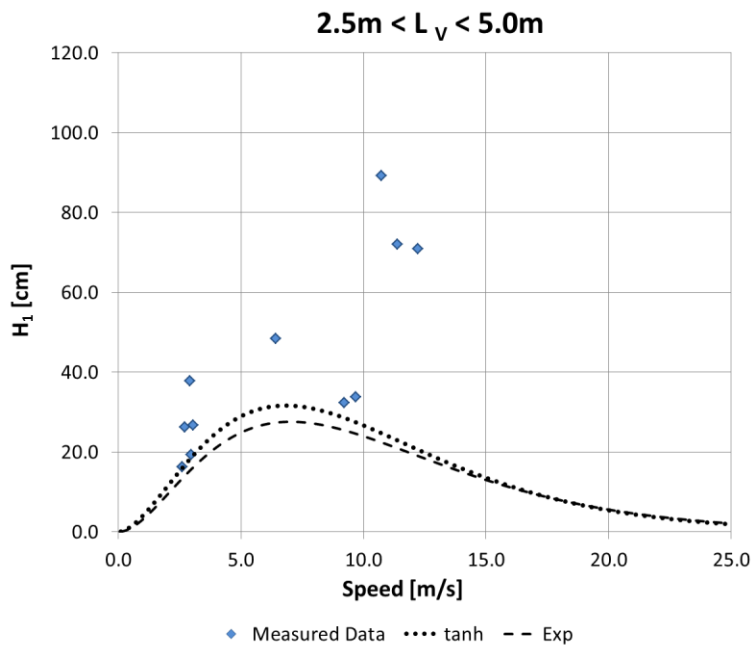


Figure 64: H_1 vs. Speed Plot for 2.5m < L < 5.0m

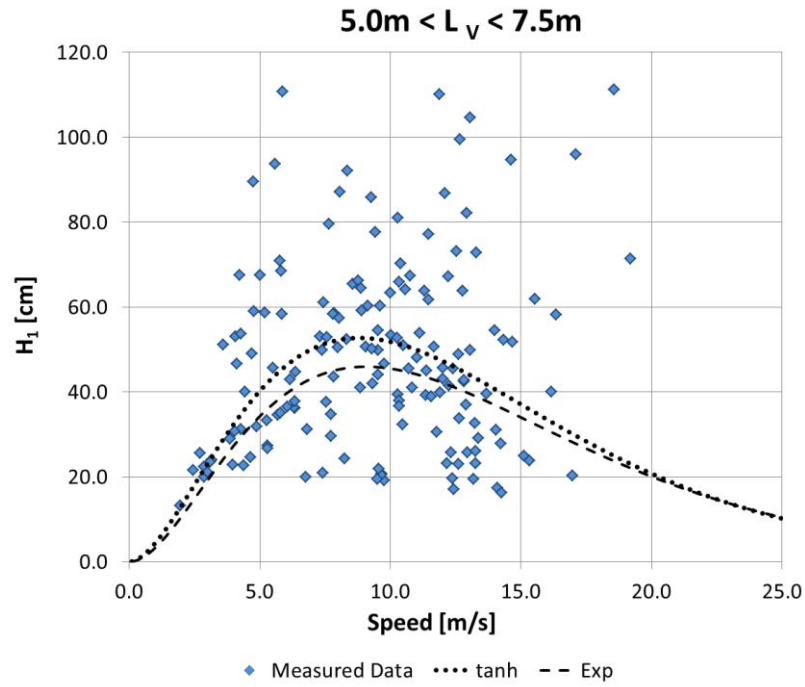


Figure 65: H_1 vs. Speed Plot for $5.0\text{m} < L < 7.5\text{m}$

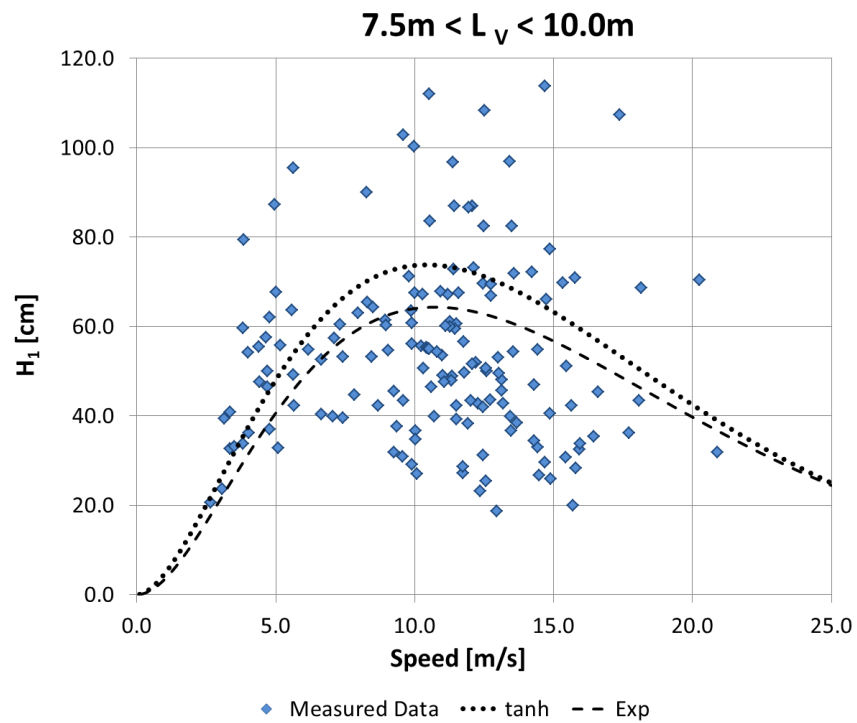


Figure 66: H_1 vs. Speed Plot for $7.5\text{m} < L < 10.0\text{m}$

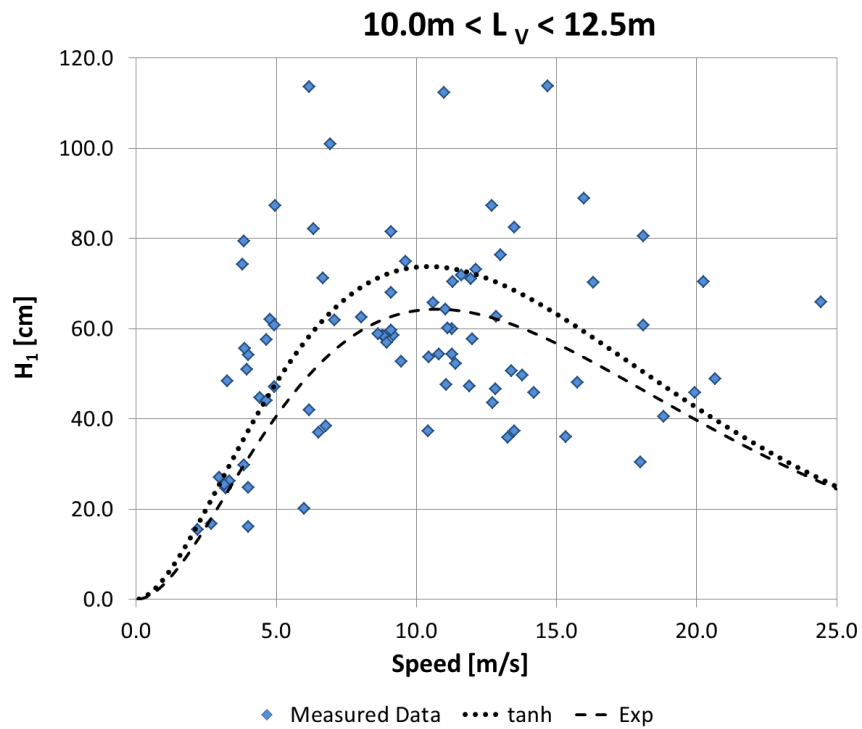


Figure 67: H_1 vs. Speed Plot for $10.0\text{m} < L < 12.5\text{m}$

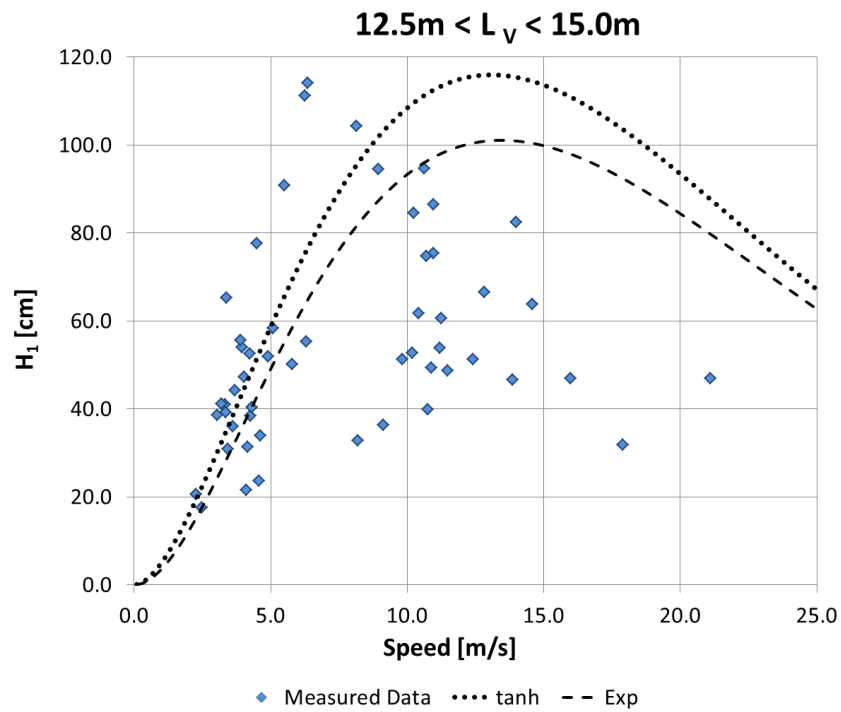


Figure 68: H_1 vs. Speed Plot for $12.5 < L < 15.0\text{m}$

CHAPTER 7 – CONCLUSIONS

The goal of this study was to develop an updated equation model capable of predicting boat-generated wave heights given a set of basic vessel parameters. Through the use of video observations, we were able to obtain target parameters, such as vessel length, speed, and its relative distance, and correlate these measurements with wave height records. Overall, this study demonstrated the viability of conducting future vessel wake studies in a low-cost and efficient manner, which can be used to support and better analyze the environment impacts of boating and vessel traffic. Several key milestones were achieved during the data collection and analysis phase of this research.

Firstly, a novel camera calibration method was established using trigonometric relationships present between the image projection plane and real world space. These projection equations were validated by measuring the lengths of known vessels such the USNA YP Patrol Crafts, and were subsequently shown to be an effective method of calibrating the camera in an environment where the absence of parallel grid/lane lines makes it difficult to establish a vanishing point. Such a camera calibration method may be adapted for use in port or harbor surveillance applications as well, where speed detection might be a requirement along certain portion of a parallel water channel (e.g. providing early warning for a suspicious vessel approaching at high speeds towards a port facility).

Secondly, the wave records obtained during the data collection phase were successfully filtered to remove anomalous data points and tidal effects. Nevertheless, the overlapping of

vessel wake frequencies with those of ambient wind waves makes it challenging to separate and distinguish them. The use of wavelet scalograms was shown to be a useful aid towards the identification process. Nevertheless, the presence of wave interference between the desirable vessel-generated waves and the unwanted wind waves meant that our dataset is influenced by constructive addition and deconstructive subtraction of wave heights magnitudes, which may contribute significantly to the amount of random error present within the data. This influence might be reduced with the use of additional wind sensor instruments that record wind speed and wind direction fluctuations over time. The information on wind speed and direction will allow estimations regarding wind wave periods and frequencies to be determined, and these calculations can subsequently be used to reduce the effect of the ambient wind waves on wave heights measured.

In all, a total of 471 data points were obtained using the Simulink program created. This database is larger than any database generated or available in past literature, and therefore expands on the current knowledge available from vessel wake studies. The numerous vessel types and models captured within our dataset also strengthen the universality of our derived equations. However, even though Simulink provides a good platform software for video processing, a large amount of time was spent processing the video data, and this process was further limited by the amount of processing memory available. On several occasions, manual verification was also required to ensure the accuracy of the vessel parameters tracker. Nevertheless, with the use of batch methods and the aid of multiple processing servers, video processing can be made more efficient for future investigations of a similar nature.

Finally, as illustrated by Figures 60 and 61, our updated equations are able to predict the general trend of vessel wake variation with vessel speed with the two controlled vessels investigated in our study. This illustrates the potential of these equations to provide a more unified description of boat wave heights across the full spectrum where past models were limited at doing so. However, this study also recognizes that due to the large amount of data scatter present in Figures 64 -68, the updated equations are still limited in their ability to account for the variability between the numerous vessel types and hull forms. Further development of our equation model will therefore be required before they can be fully implemented for effective use.

In conclusion, despite the limitations of our present equation model, the study had demonstrated the effective use of video observations to track and obtain vessel parameters as an alternative method of conducting vessel wake studies. The viability of such an alternative will reduce the amount of time and logistical effort required to obtain a broad set of vessel parameters that can be used to further theories regarding shoreline wake management and other environmental impacts of boat traffic wakes.

ACKNOWLEDGEMENTS

First, I would like to thank my primary project advisor, Professor David L. Kriebel, whose wisdom, guidance, professionalism, patience and encouragement were essential to my completion of this project. I would also like to thank my secondary advisors: Associate Professor Jenelle A. Piepmeier from the Weapons and Systems Engineering Department, for her joyful attitude as well as her guidance and expert knowledge in computer vision methods; without which this project would not be a success, and Visiting Professor Patrick J. Hudson from the Naval Architecture, Ocean Engineering Department, for his advice and recommendations throughout the duration of the project.

Next, I would like to show my appreciation to Ms. Louise Wallendorf of the USNA Hydromechanics Laboratory, as well as the rest of the Hydrolab staff: Mr John Zselezky, Mr Don Bunker, and Mr Dan Rhodes, whose instruction and hands-on guidance were crucial to the experimental and testing phase of the project. To my roommates over the duration of the project: Aaron Nowlin, Terrell Raley, Jonathan Happy and Kameron Wright; thanks for enduring my numerous late nights. Your jokes and encouragement have kept me moving on.

Finally, I would also like to thank Professor Carl Wick and the Trident Scholar Committee for their constructive input as well as the unique opportunities granted through this program.

REFERENCES

- Bas, E.K., Crisman, J.D, (1998) “An easy to install camera calibration for traffic monitoring”. Northeastern University. Boston, Massachusetts
- Begovic, E., Benassai, G., Nocerino, E., Scamardella, A., (2006) “Field investigation of wake wash generated by HSC in the Bay of Naples” University of Naples Federico II, Naples, Italy.
- Bhowmik NG, Soong TW, Reichelt WF, Seddik NML. (1991) “Waves generated by recreational traffic on the upper Mississippi River System. Research Report 117”. Illinois State Water Survey: 33–35.
- Blount DL. (1993) “Reflections on planing hull technology.” A Century of Progress in Power Boats. The Society of Naval Architects and Marine Engineers, Southeast Section, University of Miami: F1–F11.
- Crawford, R.E., Stolpe, N.E., Moore, M.J, (1998). “The environmental impacts of boating” Proceedings of a workshop at Woods Hole Oceanographic Institution. Technical Report WHOI-98–03.
- Glamore, W.C., (2008) “A Decision Support Tool for Assessing the Impact of Boat Wake Waves on Inland Waterways”, University of New South Wales, Water Research Laboratory.
- Houser, C. (2011) “Sediment Resuspension by Vessel-Generated Waves along the Savannah River, Georgia” Journal of Waterway, Port, Coastal, and Ocean Engineering, ASCE
- Kanawathi, J. Mokri, S.S., Ibrahim, N., Hussain, A., Mustafa, M.M., (2009) “Motion detection using Horn Schunck algorithm and implementation”, International Conference on Electrical Engineering and Informatics, 2009. ICEEI '09.
- Kivanc Bas, E. Crisman, J.D., (1997) “An Easy to Install Camera Calibration For Traffic Monitoring”, IEEE Conference on Intelligent Transportation Systems.
- Kriebel, D.L., Seelig, N.S, (2001) “An Empirical Model for Ship Generated Waves”.
- Kriebel, D, Seelig, W. and Judge, C. (2003) “A Unified Description of ship-generated waves”, Proceedings of the PIANC Passing Vessel Workshop, Portland, Oregon
- Maritime Navigation Commission, (2003) “Guidelines for Managing Wake Wash from High-speed Vessels”, Working Group 41, International Navigation Association.
- Maynard, S.T, (2001) “Boat waves on Johnson Lake and Kenai River, Alaska.” US Army Corps of Engineers Research and Development Center

- Maynard, S. T. (2005) "Wave height from planing and semi-planing small boats", *River Research and Applications*. 21: 1–17.
- Sheremet, A., Gravois, U., Tian, M. and Blakenship, T.K., (2011) "Boat-wake Observations at Jensen Beach, Florida" University of Florida, Gainesville, FL
- Sorensen, R.M., (1967). "Investigation of ship-generated waves" *ASCE Journal of Waterways and Harbors Division* 93.
- Sorensen, R.M., Weggel, J.R. (1984) "Development of ship wave design information" *Proceedings of the 19th Coastal Engineering Conference*. ASCE: Houston, Texas; 3227–3243
- Stumbo, S., Fox, K., Dvorak, F. and Elliot, L, (1999) *The Prediction, Measurement, and Analysis of Wake Wash from Marine Vessels*, *Marine Technology*, Vol. 36, No. 4.
- Weggel, J. and Sorensen, R., (1986) "Ship wave prediction for Port and Channel Design" *ASCE Ports'86*, pp. 797-814
- Whittaker, T.J.T., Doyle, R. and Elsaesser, B., 2001. "An Experimental Investigation of the Physical Characteristics of Fast Ferry Wash." *HIPER'01 2nd International Euro Conference on High Performance Marine Vehicles*, Hamburg, pp. 480-491.
- Yung, N.H.C. and Lai, A.H.S., (2001) "An effective video analysis method for detecting red light runners", *IEEE Transactions on Vehicular Technology*, vol. 50(4), pp. 1074-1084.
- Zabawa, C., Ostrom, C., (1980) "The role of boat wakes in shore erosion in Anne Arundel County, Maryland." *Maryland Department of Natural Resources*.
- Zhang, S., Qi, Z., Zhang, D., (2009) "Ship Tracking Using Background Subtraction and Inter-frame Correlation" *National Ocean Technology Center*, Tianjin, China.
- US Army Corp of Engineers, (2003) *Coastal Engineering Manual*, US Army Corp of Engineers.

APPENDIX A

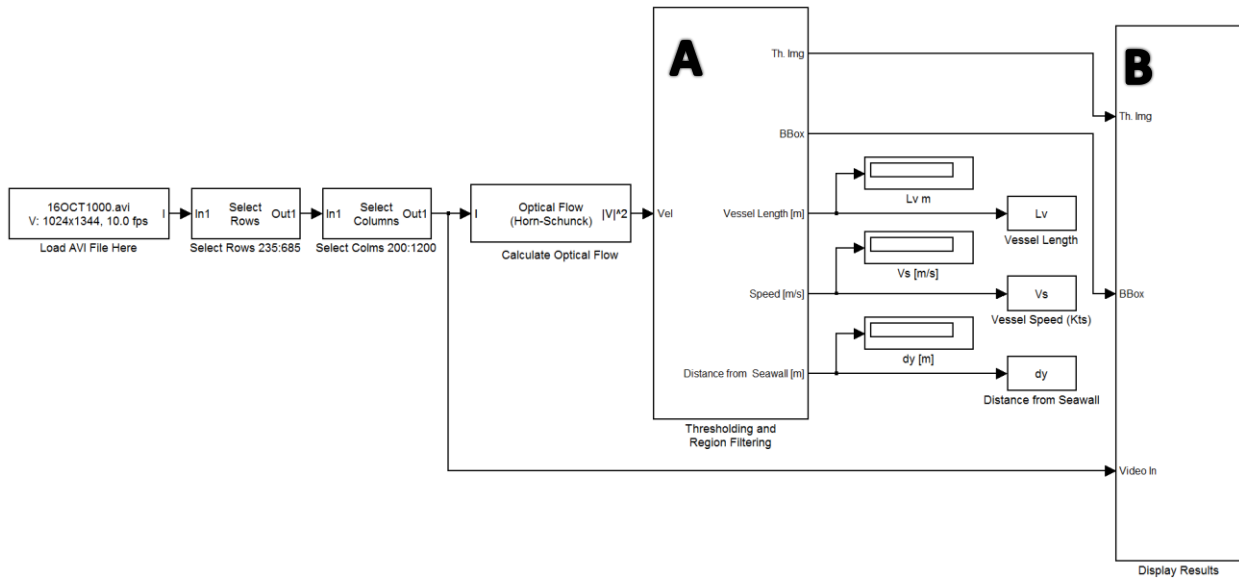
Table 4: Specifications of vessels used in calculating F_L to F_V conversion factor

Vessel Manufacturer	Model	Length [ft]	Beam [ft]	Draft [ft]	Displacement [lb]	∇ [ft ³]	Cb	$\nabla^{1/3}$ [ft]	$\nabla^{1/3}/L$
Robalo	227	21.50	8.50	1.50	3950	61.72	0.23	3.90	0.1813
	180	18.33	8.00	0.92	2600	40.63	0.30	3.40	0.1852
	200	20.58	8.33	1.00	3000	46.88	0.27	3.56	0.1729
	220	21.50	8.50	1.50	3970	62.03	0.23	3.90	0.1816
	240	24.00	8.75	1.67	5040	78.75	0.23	4.22	0.1760
	260	26.42	9.00	1.67	5820	90.94	0.23	4.43	0.1677
	300	29.17	10.50	1.75	8200	128.13	0.24	4.96	0.1701
	225	22.25	8.50	1.50	4050	63.28	0.22	3.93	0.1766
	245	24.00	8.75	1.67	5533	86.45	0.25	4.36	0.1815
	265	26.08	9.00	1.67	6340	99.06	0.25	4.56	0.1747
	305	29.17	10.50	1.75	9600	150.00	0.28	5.23	0.1792
247	24.00	8.75	1.67	5000	78.13	0.22	4.21	0.1756	
SeaRay OpenBow	300	29.50	9.08	1.92	6044	94.44	0.18	4.49	0.1520
	280	28.00	8.83	2.00	5726	89.47	0.18	4.41	0.1574
	260	26.33	8.50	1.75	5168	80.75	0.21	4.26	0.1618
	240	24.11	8.50	1.83	4850	75.78	0.20	4.17	0.1730
	220	22.00	8.33	1.83	4776	74.63	0.22	4.15	0.1886
	200	21.00	8.33	1.67	3500	54.69	0.19	3.75	0.1784
	175	17.50	7.00	1.50	2100	32.81	0.18	3.16	0.1808
	185	19.67	7.25	1.42	2600	40.63	0.20	3.40	0.1726
SeaRay Cruisers	240	24.11	8.50	1.71	5593	87.39	0.25	4.37	0.1813
	260	26.58	8.50	1.92	6950	108.59	0.25	4.70	0.1767
	280	28.67	8.83	2.00	8211	128.30	0.25	4.96	0.1731
	330	33.33	10.50	2.42	14000	218.75	0.26	5.92	0.1776
	350	35.5	11.50	2.75	15400	240.63	0.21	6.11	0.1720
	370	37.5	12.00	2.25	18064	282.25	0.28	6.44	0.1717
	310	31.00	10.00	2.50	11630	181.72	0.23	5.57	0.1796

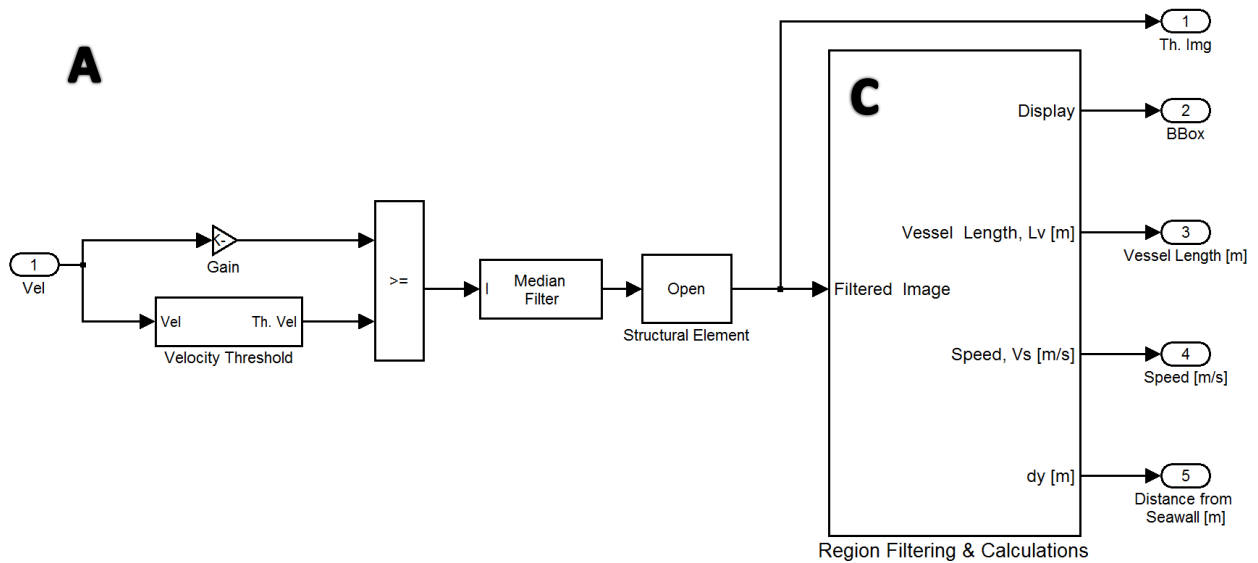
APPENDIX B

Simulink (.mdl) File Information

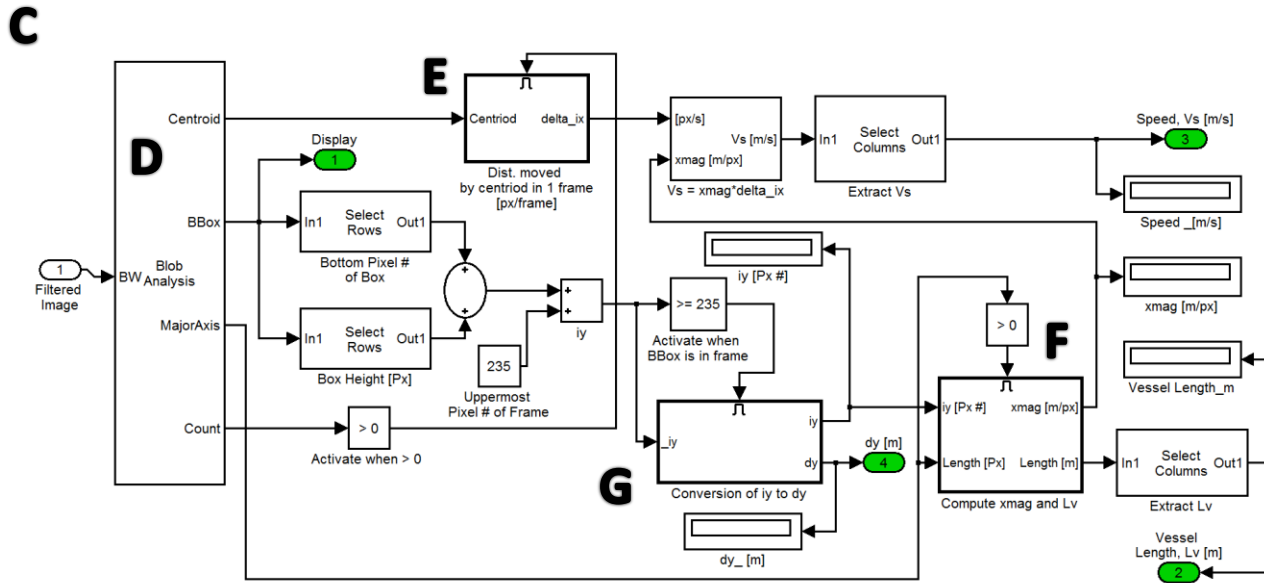
User Interface Level



Thresholding and Region Filtering Level



Region Filtering & Calculations Level



Blob Analysis Parameters

Blob Analysis
Compute statistics for connected regions in the binary image, BW.

Main | **Blob Properties** | Data Types

Parameters

Maximum number of blobs: 1

Warn if maximum number of blobs is exceeded

Output number of blobs found

Specify minimum blob area in pixels: 2000

Specify maximum blob area in pixels: 110000

Exclude blobs touching image border

Output blob statistics as a variable size signal

Fill empty spaces in outputs

Fill values: -1

Blob Analysis
Compute statistics for connected regions in the binary image, BW. **D**

Main | **Blob Properties** | Data Types

Statistics

Area

Centroid

Bounding box

Major axis length

Minor axis length

Orientation

Eccentricity

Equivalent diameter squared

Extent

Perimeter

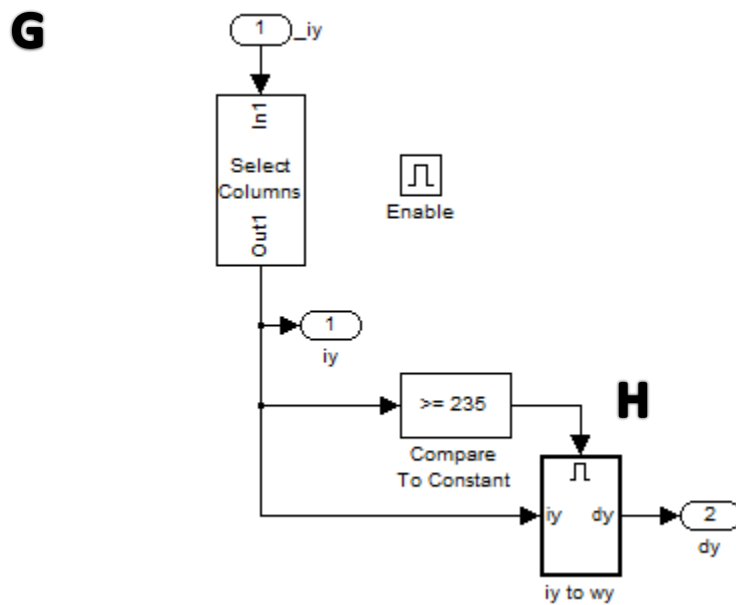
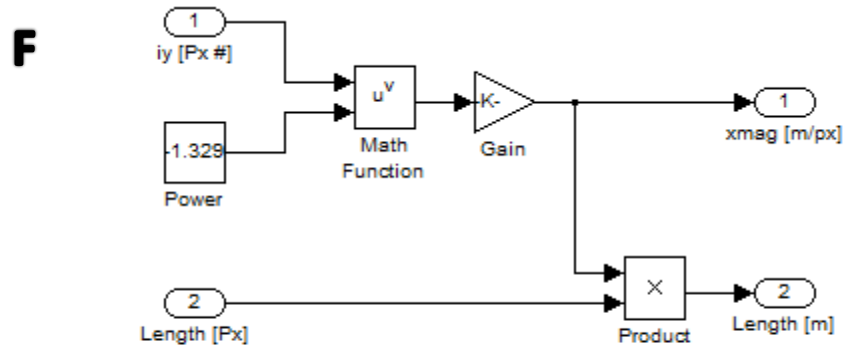
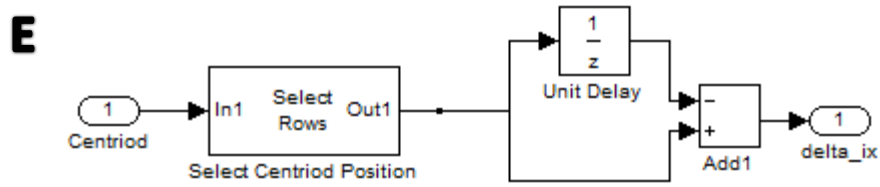
Statistics output data type: single

Note: Area and Bounding box outputs are data type int32.

Label Parameters

Connectivity: 8

Output label matrix



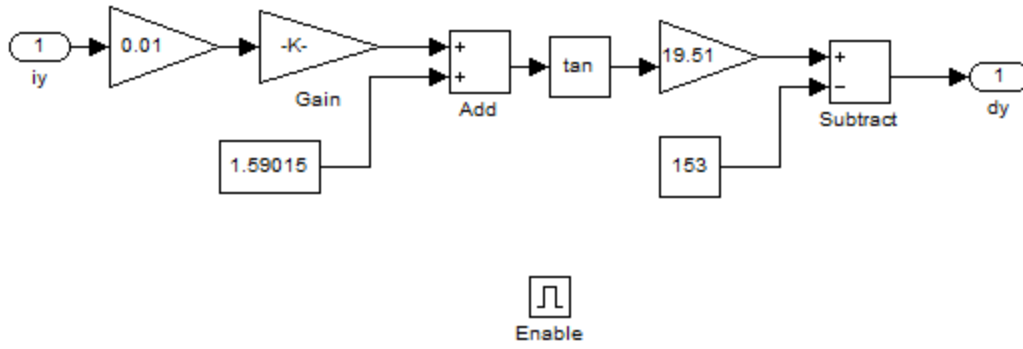
H



iy dy

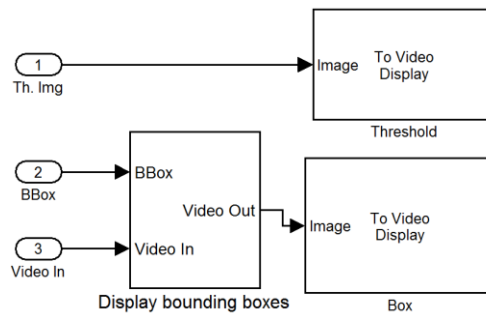
iy to wy

H



Display Results Level

B



APPENDIX C

AWAC Deployment Plan Setup (AST software)

Deployment Planning

Standard | Advanced

Current profile

Profile interval (s): 600

Number of cells: 5

Cell size (m): 1

Instrument

Frequency: 1 MHz

Deployment planning

Assumed duration (days): 7

Estimated depth (m): 5

Battery utilization (% of 540 Wh): 14

Memory required (MB): 23.8

Vertical vel. prec. (cm/s): 0.7

Horizont. vel. prec. (cm/s): 2.2

Compass update rate (s): 600

Power level: HIGH

Waves

Number of samples: 1024

Sampling rate: 2 Hz

Interval (s): 600

SUV mode (for sub-surface buoy)

Use Advanced Settings

Start Update OK Cancel Apply Help

Deployment Planning

Standard | Advanced

Current profile

Average interval (s): 60

Blanking dist. (m): 0.41

Measurement load (%): 37

Compass upd. rate (s): 600

Coord. system: ENU

Power level

High

Low

Deployment planning

Assumed duration (days): 7

Estimated depth (m): 5

Battery utilization (% of 540 Wh): 14

Memory required (MB): 23.8

Vertical vel. prec. (cm/s): 0.7

Horizont. vel. prec. (cm/s): 2.2

Speed of sound

Measured

Salinity (ppt): 4

Fixed (m/s): 1525

File wrapping

Update from Standard

Waves - static mode

Velocity cell size (m): 0.6

AST window start (m): 3.4

AST window size (m): 3.2

Find first peak

AST threshold: 100

Analog inputs

Input 1: NONE

Input 2: NONE

Output power

Start Update OK Cancel Apply Help

APPENDIX D

MATLAB .m Files

Converting AWAC .wad files to .txt

```

% This file simply reads in the processed wave data from the
% QuickWave software. This reads data from both AWAC and Nortek
% PUV instruments (Vector, Aquadopp, Aquadopp Profier)
% GetWad - program to get AWAC unprocessed data from .WAD file
% pname: Pathname ie 'c:\data\'
% fname: Filename ie 'someawacdata.wad'

pname='c:\Users\m126690\Desktop\';
fname='FINALW01.wad';

file2Get = [pname,fname];

WAPdata.file2Get =file2Get;

% Read in Unprocessed AWAC data  rw - # rows cl - # columns
data = dlmread(file2Get);
[rw,cl] = size(data);
if (cl==1 )
    data = dlmread(file2Get, '\t');
    [rw,cl] = size(data);
end

if (cl == 13)
WAPdata.Run = data(:,1)';    % number of data run
WAPdata.Pt  = data(:,2)';    % # of pts. in acquisition (1 to 1024), deltat
1/4 sec.
WAPdata.Press = data(:,3)';
WAPdata.AST1  = data(:,4)';
WAPdata.AST2  = data(:,5)';
WAPdata.ASTQuality = data(:,6)';
WAPdata.Analog = data(:,7)';
WAPdata.V1 = data(:,8)';
WAPdata.V2 = data(:,9)';
WAPdata.V3 = data(:,10)';
WAPdata.Amp1 = data(:,11)';
WAPdata.Amp2 = data(:,12)';
WAPdata.Amp3 = data(:,13)';
end

file2write=[file2Get, '.tab']
[fid,message]=fopen(file2write, 'w');
for i=1:rw;
fprintf(fid, '%6.3f \t %6.3f \r\n', WAPdata.AST1(i), WAPdata.AST2(i)); %print
longitude, latitude ( and \r\n - carriage ret & new line)
end
fclose(fid);

```

Reshape AWAC Wave Data for processing

```

clear all
close all

% read file "date.txt"
load Oct23.txt;
X=Oct23;
clear Oct23;

yr=X(:,3);
mo=X(:,1);
da=X(:,2);
hh=X(:,4);
mm=X(:,5);
ss=X(:,6);
pres=X(:,7);
etaA=X(:,8);
etaB=X(:,9);

N=length(etaA);

% initialize new arrays (eta, mmt, hht)
eta(1:2*N)=0;
sst(1:2*N)=0;
mmt(1:2*N)=0;
hht(1:2*N)=0;

% merge A and B values for eta
for n=1:N
    eta(2*n-1)=etaA(n);
    eta(2*n)=etaB(n);
end

% Create time flow

for n=1:N                                %Seconds
    sst(2*n-1)=ss(n);
    sst(2*n)=ss(n)+0.25;
end

for n=1:N                                %Minutes
    mmt(2*n-1)=mm(n);
    mmt(2*n)=mm(n);
end

for n=1:N                                %Hours
    hht(2*n-1)=hh(n);
    hht(2*n)=hh(n);
end

% Reshape data into single column
[eta, perm, nshifts]=shiftdata(eta,2);
reshape(eta, (N*2),1);

```

```

[sst,perm,nshifts]=shiftdata(sst,2);
reshape(sst, (N*2),1);

[hht,perm,nshifts]=shiftdata(hht,2);
reshape(hht, (N*2),1);

[mmt,perm,nshifts]=shiftdata(mmt,2);
reshape(mmt, (N*2),1);

time=hht+mmt/60+sst/3600;

wavdata(:,1)=time;
wavdata(:,2)=eta;

% Save day wave data

dlmwrite('Wave.txt',wavdata,'delimiter','\t','precision','%.6f')

```

Analyze AWAC Data (Wave.txt)

```

clc
clear all
close all

%Access RawWave File
load Wave.txt
X=Wave;
clear Wave;

time=X(:,1);
eta=X(:,2);

N=1;
constant=12288;
start=constant*N+1;
fin=constant*(N+1);

timeW=time(start:fin);
eta=eta(start:fin);

N=length(eta);

% Remove Tides using High Pass Filtering
[b,a] = butter(5,0.2/2);
tide = filtfilt(b,a,eta);

% Remove Anomalies bursts if > 1.0m
eta=eta-tide;
eta(abs(eta)>2.0)=0;
etaraw=eta;

```

```

% Generate spectrum

dt=0.25;
%duration of wave record

td=N*dt;
%define fourier frequencies

df=1/td;
%use compact notation to define N frequencies

f=0:df:(N-1)*df;
%starting from 0, increasing by df for N variables
%run FFT to obtain a and b coefficients at all frequencies

coef=(2/N)*fft(eta);
%gives complex coefficeints, a and b

Amp=abs(coef);
%find amplitude of the fourier wave component

spectrum=0.5*(Amp.*Amp)/df;
%Find Spectral Density

S=smooth(spectrum);

figure
plot(f,S);

xlim([0.1 2]);
%xmin xmax ymin ymax
Title 'Filtered Spectrum'
xlabel('Frequency, f (Hz)')
ylabel('Spectral Density, S (ft^2/Hz)')

sigmaeta=std(eta);

% Remove Anomalies delta_x > 0.5m in 0.25sec

% Set threshold value
thresh=10*sigmaeta;

% Remove Adjacent Anomalous Values
diffeta=abs(diff(eta));
bigpts = find(diffeta > thresh);
eta(bigpts)=0;
eta(bigpts+1)=0;
eta(bigpts-1)=0;

%Sampling Frequency for Wavelet Analysis
sf=4;
factor = 5/(2*pi);
freq = [0.1:0.005:2];
scale = factor * sf./ freq;

```

```

%Plot Final Figure
figure
subplot (2,1,1)
plot (timeW,eta)
Title 'Wave Displacement'
ylabel('Wave Displacement (m)')
ylim([-0.5,0.5])

subplot (2,1,2)
CWTcoeffs = cwt(eta,scale,'morl');
imagesc(timeW,freq,abs(CWTcoeffs));
axis('xy');
xlabel('Time (Hr)')
ylabel('Frequency (Hz)')
Title 'Spectrogram'

% Save combined plot
saveas (gcf,'WaveData_0700.fig');

```

Extracting Boat Parameters (Post Simulation)

```

close all
Lvseries=squeeze(Lv.signals.values);
Vsseries=squeeze(Vs.signals.values);
dyseries=squeeze(dy.signals.values);

%Number of Frames -----CHANGE FILENAME
aviinfo 'TestTrack.avi';
N=squeeze(ans.NumFrames);

%Establish Time Series
tout=0:0.1:N-1;
tout=tout(1:N);

%Extract Boat Parameters from Simulink sink
L=Lvseries(1:N);
V=Vsseries(1:N);
d=dyseries(1:N);

%Calculate video duration (secs)
filedur=N*0.1;

%Get frame transfer constant (videoduration=1hr*3600s)
convf=3600/filedur;

% One second of video = realdur seconds in real time

%Enter Video Start time ----- CHANGE START TIME
strtime=10;

%Converting Video Time to Real Time
realtout=tout*convf;
acttime=strtime+realtout/3600;

```

```

%Plot Raw Unfiltered Readings
subplot (3,1,1)
plot (acttime,L)
Title 'Boat Length'
xlabel('Time (Hr)')
ylabel('Length (m)')

subplot (3,1,2)
plot (acttime,V)
Title 'Boat Speed'
xlabel('Time (Hr)')
ylabel('Speed (kts)')

subplot (3,1,3)
plot (acttime,d)
Title 'Distance from Gage'
xlabel('Time (Hr)')
ylabel('Distance, dy (m)')

dataraw(:,1)=acttime;
dataraw(:,2)=L;
dataraw(:,3)=V;
dataraw(:,4)=d;

% Save Raw Boat Parameters as txt file -----CHANGE FILENAME

dlmwrite('BoatData_Oct23_1000_raw.txt',dataraw,'delimiter','\t','precision',
%.6f')
saveas (gcf,'BoatData_Oct23_1000_raw.fig');

%-----BOAT FILTER PORTION-----%

clear all
%Access Raw File
load BoatData_Oct23_1000_raw.txt
X=BoatData_Oct23_1000_raw;
clear BoatData_Oct23_1000_raw;

acttime=X(:,1);
L=X(:,2);
V=X(:,3);
d=X(:,4);

% Pinpoint Boat Occurrences
show=find(L>0);
showtime=acttime(show);
%Filter Readings
L(abs(L)<4)=0;
V(abs(L)<4)=0;
d(abs(L)<4)=0;

L(abs(L)>45)=0;
V(abs(L)>45)=0;
d(abs(L)>45)=0;

```

```

L(abs(V)>10)=0;
V(abs(V)>10)=0;
d(abs(V)>10)=0;

L(abs(d)>350)=0;
V(abs(d)>350)=0;
d(abs(d)>350)=0;

data(:,1)=acttime;
data(:,2)=L;
data(:,3)=V;
data(:,4)=d;

show=0;

timeB=X(:,1);
L=X(:,2);
V=X(:,3);
d=X(:,4);

%Smooth Data
L=smooth(L);
V=smooth(V);
d=smooth(d);

%Load Wave Data
load WavehtData_Oct23.txt
Y=WavehtData_Oct23;
clear WavehtData_Oct23;

timeW=Y(:,1);
eta=Y(:,2);

%Establish File Series for Wave Data-----CHANGE FILE NUMBER
file=10;

N=file-6;
constant=12288;
start=constant*N+1;
fin=constant*(N+1);

timeW=timeW(start:fin);
eta=eta(start:fin);
postime=postime(postime>file);
postime=postime(postime<(file+1));
poseta=poseta(postime);

show=find(L>0);
showtime=timeB(show);

show=0;

figure
subplot (4,1,1)

```

```
plot (timeB,L)
Title 'Boat Length'
xlabel('Time (Hr)')
ylabel('Length (m)')

subplot (4,1,2)
plot (timeB,V)
Title 'Boat Speed'
xlabel('Time (Hr)')
ylabel('Speed (kts)')

subplot (4,1,3)
plot (timeB,d, showtime,show,'r*')
Title 'Distance from Gage'
xlabel('Time (Hr)')
ylabel('Distance, dy (m)')

subplot (4,1,4)
plot (timeW,eta, showtime,show,'r*',postime, poseta,'y*')
Title 'Wave Displacement'
xlabel('Time (Hr)')
ylabel('Wave Displacement (m)')

% Save combined plot-----CHANGE FILENAME
saveas (gcf,'CombinedData_Oct23_1000.fig');
```